The Characterization of Thin Film Nickel Titanium Shape Memory Alloys

by

Nicole Latrice Harris Odum

A dissertation submitted to the Graduate Faculty of
Auburn University
in partial fulfillment of the
requirements for the Degree of
Doctor of Philosophy

Auburn, Alabama
December 13, 2010

Keywords: Nickel Titanium, shape memory alloys, thin films, nanomechanics, characterization methods

Copyright 2010 by Nicole Latrice Harris Odum

Approved by

Barton C Prorok, Chair, Associate Professor, Materials Engineering Department
ZhongYang Cheng, Associate Professsor, Materials Engineering Department
Dong-Joo (Daniel) Kim, Associate Professor, Materials Engineering Department
Aleksandr Simonian, Professor, Materials Engineering Department
P.K. Raju, Thomas Walter Professor, Mechanical Engineering Department

Abstract

Shape memory alloys (SMA) are able to recover their original shape through the appropriate heat or stress exposure after enduring mechanical deformation at a low temperature. Numerous alloy systems have been discovered which produce this unique feature like TiNb, AgCd, NiAl, NiTi, and CuZnAl. Since their discovery, bulk scale SMAs have undergone extensive material property investigations and are employed in real world applications. However, its thin film counterparts have been modestly investigated and applied. Researchers have introduced numerous theoretical microelectromechanical system (MEMS) devices; yet, the research community's overall unfamiliarity with the thin film properties has delayed growth in this area. In addition, it has been difficult to outline efficient thin film processing techniques. In this dissertation, NiTi thin film processing and characterization techniques will be outlined and discussed. NiTi thin films—1 μm thick—were produced using sputter deposition techniques. Substrate bound thin films were deposited to analysis the surface using Scanning Electron Microscopy; the film composition was obtained using Energy Dispersive Spectroscopy; the phases were identified using X-ray diffraction; and the transformation temperatures acquired using resistivity testing. Microfabrication processing and sputter deposition were employed to develop tensile membranes for membrane deflection experimentation to gain insight on

the mechanical properties of the thin films. The incorporation of these findings will aid in the movement of SMA microactuation devices from theory to fruition and greatly benefit industries such as medicinal and aeronautical.

Acknowledgements

As this journey has been an intense and long one, the enlightenment and benefits far outweigh the tension. There are a number of people that I would like to acknowledge and thank for their support during my journey. Firstly, I would like to thank my advisor, Dr. Barton C. Prorok, for his unconditional support, guidance, patience, and understanding as I completed this task. Thank you, Dr. Bryan Chin for always being a continual support and source of wisdom. My committee members, Dr. ZhongYang Cheng, Dr. Dong-Joo (Daniel) Kim, Dr. Aleksandr Simonian, and Dr, P.K. Raju for providing their input and advice. Mr. Roy Howard, Dave Lindahl, and L.C. Mathison for always helping me resolve my technical issues. I would also like to thank all of my past and present research group members—especially Ms. Liwei Wang, Mr. Shakib Morshed, Mr. Bo Zhou, and Mr. Dong Liu.

To my family—Johnnie, Sr., Ethel, Andrea, and Johnnie, Jr— and friends you have all been my continual support team throughout my entire academic career. Thank you for always believing in me, keeping me focused, and spiritually grounded.

Finally, I would like to acknowledge my biggest supporter and encourager, my husband, Mr. LeVar Odum. Thank you for pushing me along even when I was defiant.

I would like to dedicate this dissertation and research work to my dear friend, Dr. Dennis Weatherby.

Table of Contents

Abstract ii

Acknowledgements iv

List of Tables ix

List of Figures x

Chapter 1 Introduction and Research Objectives 1

1.1 Shape Memory Alloy Definition 1

1.2 Historical Background of Shape Memory Alloys 2

1.3 NiTi Phase Diagram 5

1.4 NiTi Shape Memory Alloys Crystal Structures 6

1.5 The Role of Martensite 8

1.6 Shape Memory Alloy Behavior 10

1.7 Bulk Scale Shape Memory Alloys 11

1.7.1 Bulk Scale Shape Memory Alloy Characterization Methods. 12

1.7.2 Bulk Scale Shape Memory Alloy Applications 13

1.8 Motivation for Project 18

1.9 Research Objectives 19

1.10 References 20

Chapter 2 Nickel Titanium Thin Film Processing Techniques 22

2.1 NiTi Thin Film Fabrication Techniques 22

2.2 Working Mechanism for Sputter Deposition 23

2.3 Deposition Issues for NiTi Shape Memory Films 25
2.4 References 31
Chapter 3 Current Nickel Titanium Thin Film Applications 33
3.1 Current Nickel Titanium Thin Film Applications 33
3.2 References 42
Chapter 4 Nickel Titanium Thin Film Characterization....................................... 43
4.1 X-Ray Diffraction and NiTi Thin Films 44
4.2 Scanning Electron Microscopy and NiTi Thin Films........................... 48
4.3 Energy Dispersive X-Ray Spectroscopy and NiTi Thin Films 50
4.4 Nanoindentation and NiTi Thin Films 53
4.5 Electrical Resistivity and NiTi Thin Films 58
4.6 References 63
Chapter 5 Experimental Procedure 65
5.1 NiTi Thin Film Production for Deposition Parameter Determination... 65
5.2 NiTi Thin Film Characterization Techniques 70
5.2.1 Phase Identification of Deposited Films 71
5.2.2 NiTi Thin Film Microstructural Observation 71
5.2.3 NiTi Thin Film Composition Determination..................................... 71
5.2.4 NiTi Thin Film Electrical Resistivity Testing 72
Chapter 6 Results and Discussion... 75
6.1 NiTi Thin Film and Crystallography 75
6.2 NiTi Thin Film and Surface Observations 78
6.3 NiTi Thin Film and Composition 83

6.4 NiTi Thin Film Sample Production Elimination 85

6.5 Additional NiTi Thin Film Production 85

6.6 NiTi Thin Film and Transformation Temperature 89

6.7 References 122

Chapter 7 Conclusion and Future Work 123

List of Tables

Table 1-1 Detailed information about the phases seen during shape memory effect 8

Table 1-2 List of NiTi shape memory alloy properties measured on the bulk scale 13

Table 1-3 List of SMA applications and their respective industries 15

Table 2-1 Lattice parameters and information about the precipitates often found in SMA following processing 28

Table 3-1 Relationship table between MEMS actuation type and potential applications 34

Table 4-1 Information about two commonly used nanoindenter tips 54

Table 4-2 Table showing how electrical resistivity and DSC transformation temperature data collection is comparable 59

Table 5-1 List of the parameters used for silicon wafers 66

Table 5-2 Titanium adhesion layer sputter deposition parameters 67

Table 5-3 Design of experiment array developed for NiTi thin film production ... 68

Table 5-4 NiTi thin film co-sputtering parameters 70

Table 6-1 XRD scan results for samples produced in DOE array 77

Table 6-2 Presentation of the NiTi film compositions before and after annealing 84

Table 6-3 Outline of the sputtering parameters for Sample 20-21 87

Table 6-4 Presentation of sputtering parameters for Samples 20-45, 20-64, 20-101, and 25-1 88

Table 6-5 Resistivity data comparison between literature samples and experimental samples 121

List of Figures

Figure 1-1 Microscopic description of the shape memory effect........................... 2

Figure 1-2 Timeline describing the history of the discovery of numerous shape memory alloy systems.. 5

Figure 1-3 Phase Diagram for Titanium-Nickel.. 6

Figure 1-4 Schematic showing the relationship between crystal structure and microstructure 7

Figure 1-5 Stress-strain schematic comparing shape memory effect to superelasticity 11

Figure 1-6 Schematic of the Frangibolt release bolt 16

Figure 1-7 Photograph of a stent in its expanded position................................. 17

Figure 2-1 Schematic showing the magnetron sputter deposition configuration.25

Figure 3-1 Illustration of the actuator micropump developed by Bernard *et al...* 36

Figure 3-2 Illustration of the microwrapper developed by Gill, *et al* 37

Figure 3-3 NiTi–Si cantilever with a slot cut out by a femtosecond laser............ 38

Figure 3-4 SEM micrograph of a NiTi SMA cantilever micro-array 40

Figure 3-5 Schematic and photograph of zigzag shaped spring......................... 41

Figure 4-1 Schematic showing the relationship between XRD and lattice atoms... 45

Figure 4-2 NiTi thin film XRD scan showing scans before and after crystallization 47

Figure 4-3 Examples of XRD scan samples of NiTi thin films presented in literature: (a) JJ Gill *et al.* 2.5 μm thick film (b) CL Shih *et al* 2 μm thick film (c) W Huang *et al* 5 μm thick film (d) A Kumar *et al* 5 μm thick film 48

Figure 4-4 SEM micrographs of NiTi films deposited by Kumar et al. at various temperatures: (a) 350°C, (b) 450°C, (c) 550°C, (d) 650°C 49

Figure 4-5 SEM micrograph showing the surface of the microwrapper produced by JJ Gill *et al.* 50

Figure 4-6 Modern EDS system schematic as outfitted with a SEM 52

Figure 4-7 Plot describing the relationship between NiTi film composition and transformation temperature 53

Figure 4-8 Schematic of typical nanoindentation system 55

Figure 4-9 Common presentation of data obtained from nanoindentation tests 56

Figure 4-10 Schematic showing typical four point probe resistivity testing setup 60

Figure 4-11 Example of graphs showing NiTi thin film resistivity testing results presented in literature 62

Figure 5-1 Photograph of Teflon holder for SMA thin film resistivity testing. (A) Side view. (B) Top view 73

Figure 5-2 Photograph of electrical resistivity testing set-up 74

Figure 6-1 XRD scan exhibiting the transformation from amorphous to crystalline films 76

Figure 6-2 SEM micrographs of films deposited at 25°C and annealed at 600°C for 30 minutes 79

Figure 6-3 SEM micrographs of films deposited at 230°C and annealed at 420°C for 15 minutes 81

Figure 6-4 SEM micrographs of films deposited at 400°C and no anneal 82

Figure 6-5 Photograph of the interior of the environmental chamber and Pomona clip for resistivity testing 90

Figure 6-6 Photograph of the measurement setup of the resistivity testing setup ... 91

Figure 6-7 Resistivity plots for SMA wire and thin film sample 15-09N using the environmental chamber ... 93

Figure 6-8 Resistivity testing results of Sample 15-09N performed using 0.1 A current application ... 95

Figure 6-9 Resistivity testing results of Sample 15-09N performed using 0.5 A current application ... 95

Figure 6-10 Resistivity testing results of Sample 15-09N performed using 1 A current application ... 96

Figure 6-11 Resistivity plot for Flexinol wire ... 98

Figure 6-12 Resistivity plot for repeated Flexinol wire test ... 98

Figure 6-13 Image of the resistivity testing setup for the wire using Kapton tape ... 99

Figure 6-14 Resistivity plots of Flexinol wire using 1 A current application [A] Plot from the initial two temperature cycle run [B] plot from additional testing ... 101

Figure 6-15 Schematic and photograph of 20-channel card used for 4-wire ohm configuration ... 102

Figure 6-16 Resistivity plot of Flexinol wire sample after 4-wire ohm configuration was implemented ... 103

Figure 6-17 Resistivity plot for Flexinol wire after continued testing ... 105

Figure 6-18 Resistivity plots for Sample 15-09M and 15-52N using different testing ranges. [A] Sample 15-52N using 0.1 KΩ testing range. [B] 15-52N using 1 KΩ testing range ... 106

Figure 6-19 Micrographs of Pomona clip leads ... 108

Figure 6-20 Resistivity plot for the Johnson Matthey commercial sample with and without the addition of the silver paste ... 109

Figure 6-21 Resistivity test results for Johnson Matthey film sample featuring silver paste contacts ... 110

Figure 6-22 Photographs of the newly constructed Teflon resistivity holder..... 111

Figure 6-23 Resistivity plot of the Johnson Matthey commercial film with silver contacts 112

Figure 6-24 Resistivity plot for Sample 20-21-C 113

Figure 6-25 Resistivity plots for Samples 20-64-C and 20-64-D........................ 115

Figure 6-26 Resistivity profiles for Samples 20-101-A and 20-101-B 117

Figure 6-27 Resistivity plots for Samples 25-1-A and 25-1-B 119

Chapter 1 Introduction and Research Objectives

1.1 Shape Memory Alloy Definition

Alloys that exhibit the shape memory effect (SME) are those that are previously deformed, usually at a low temperature, and are capable of returning to their original shape or form when exposed to the appropriate thermal or stress procedure [1]. In microscopic terms, the austenite phase is cooled to form a martensitic structure with a twinned lattice. Following the application of stress, the twins self accommodate through deformation and heating returns this lattice back to its austenite phase. The self accommodation of the twins results from the martensite phase possessing a lower symmetry than the austenite phase. Figure 1.1 provides an illustration of this microscopic shape changing process.

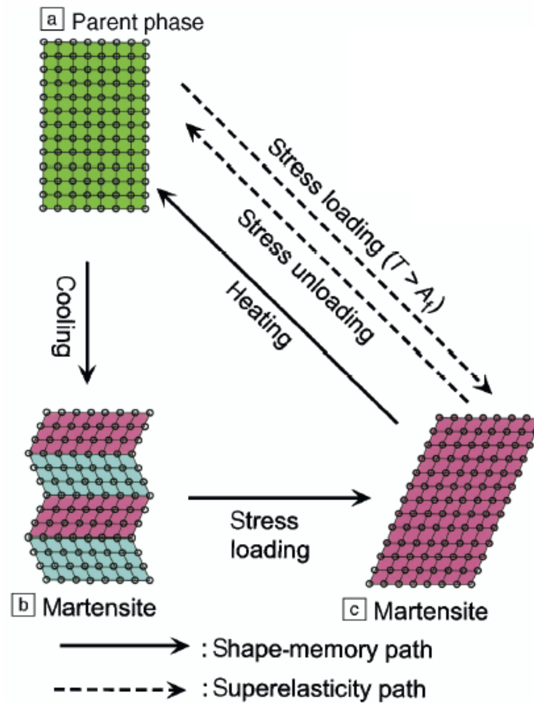

Figure 1-1 Microscopic description of the shape memory effect.

1.2 Historical Background of Shape Memory Alloys

The first documentation of the shape memory alloy (SMA) dates back to 1938 when Alden B. Greninger of Harvard University and V.G. Mooradian of Massachusetts Institute of Technology proved that a copper and zinc alloy was capable of being deformed and reverting back to its original state during a temperature change. Separate investigations by G.V. Kurdyumov, a Russian metallurgist, exploring martensite's crystallography in steel and brass and Thomas A. Read, from the University of Illinois, exploring gold-cadmium provided further proof of the existence of this phenomenon. Although additional research has shown that other systems also show shape memory effect, emphasis on this phenomenon did not grab worldwide publicity until William J. Buehler of the U.S.

Naval Ordinance Laboratory presented his findings in 1962 on nickel-titanium. In his honor, nickel titanium shape memory alloys are also known as Nitinol—Nickel titanium Naval Ordinance Laboratory. [1]

In 1958, Buehler was assigned to identify a material able to "withstand the high temperature rigors of a missile re-entry nose cone." He decided to focus on intermetallics due to their high melting temperature and found 60 systems to fit his criteria. The 60 systems were narrowed down to 12, with NiTi being one of those chosen. Each of the 12 systems was alloyed into ½" thick x 2½" diameter cast buttons using a controlled atmosphere arc-melting. Buehler and team used a simple test of hammer striking to determine the brittleness of the systems and found that equiatomic NiTi was the most impact resistant. To further study its properties, additional samples were developed in wrought form by hot and cold rolling, hot and cold swaging, and wire drawing at room temperature. They observed that when arc cast NiTi bars (⅝" diameter x 4" long) were suspended and struck, an unusual and unique acoustic damping in lieu of temperature was heard. (NOL also investigated 55 weight percent NiTi for shape memory effects and 60 weight percent NiTi for non-magnetic precipitation hardened tool-like material.) This was a Eureka point in the research and lead to extensive metallographic, physical, and mechanical property study. Through these investigations, the team found that the (1) annealing of cold rolled sheets and cold drawn wire resulted in length reduction, (2) hardness indentations done at room temperature were reduced in size with heat application, and (3) acoustic damping changed at temperatures similar to those seen above. These findings were all

indicators of shape memory behavior, but the most exciting find occurred around 1962 when Buehler took a thin strip of NiTi to a management meeting where it was bent into an accordion shape, supposedly to exhibit its fatigue resistance. However, one of the management team members applied heat from his pipe lighter causing the strip to extend with a considerable amount of force, proving the conversion of heat energy into mechanical energy. Within 5 years, the excitement about the new material reached several agencies and was applied. [3]

Numerous alloy systems have been discovered that exhibit the shape memory effect like TiNb, AgCd, NiAl, NiTi, and CuZnAl. Figure 1.2 presents a timeline of the discovery of SMA systems. Yet, only two systems have been provided substantial commercial attention—copper-based systems (such as CuZnAl and CuAl Ni) and Nickel Titanium (Nitinol or NiTi). The NiTi system is often preferred due to its large shape memory strain, thermal stability, excellent corrosion resistance, high ductility, considerable work per unit mass, and attractive transformation temperature [1,4].

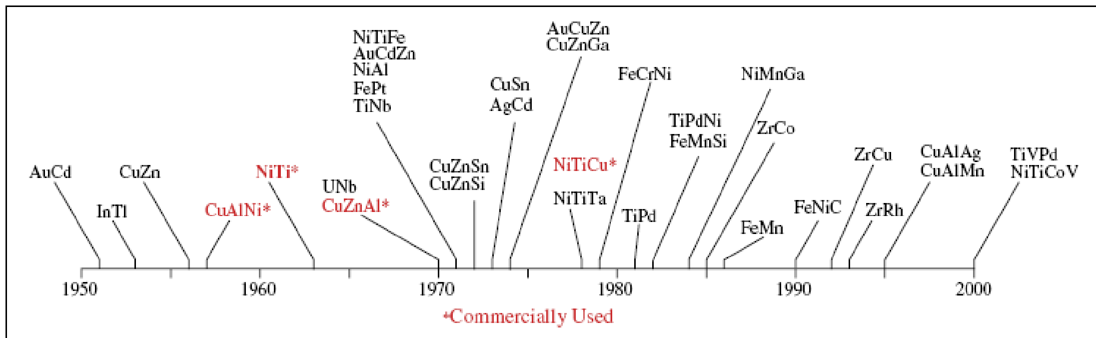

Figure 1-2 Timeline describing the history of the discovery of numerous shape memory alloy systems [5]

1.3 NiTi Phase Diagram

The currently accepted phase diagram is a modified version of the original. Massalski *et al*, prepared this version featuring the deletion of the dotted line at 630°C showing the eutectoid decomposition of TiNi→Ti_2Ni + $TiNi_3$ because no experimental data was able to confirm this decomposition. Instead, a dotted line was added at 1090°C to indicate the transition from BCC→B2. The addition of this line makes it easier to determine the beneficial heat treatments for the improvement of shape memory characteristics. [6]

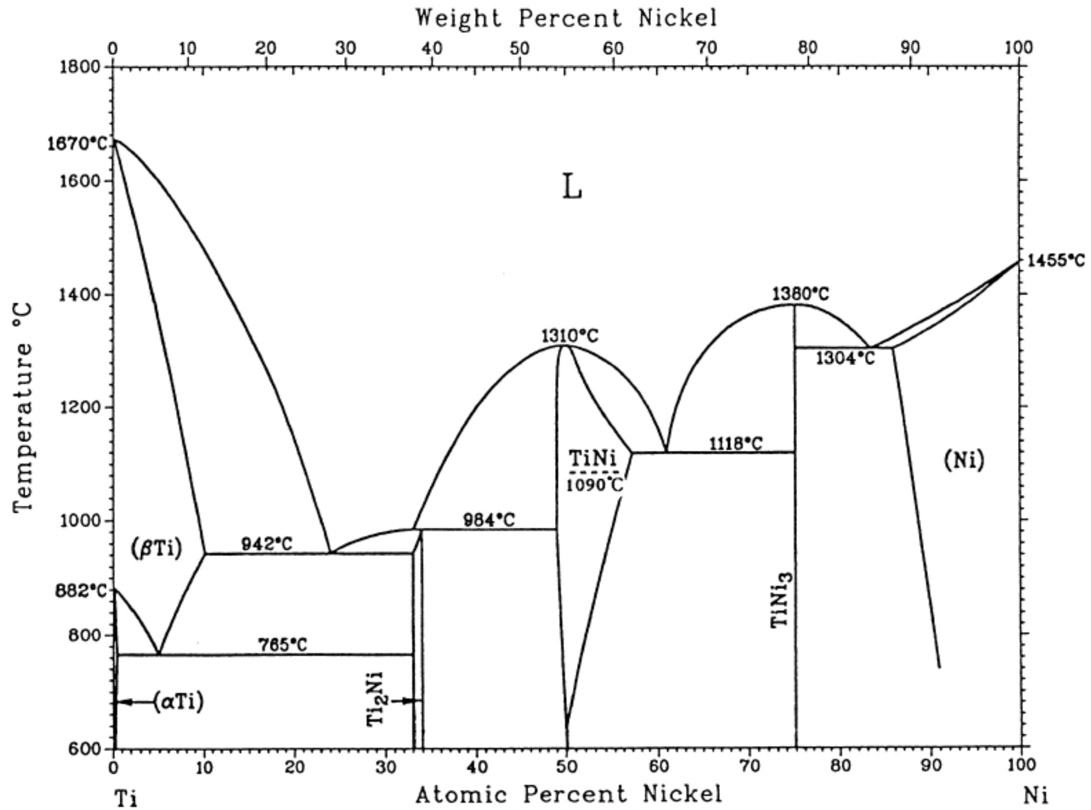

Figure 1-3 Phase Diagram for Titanium-Nickel [6]

1.4 NiTi Shape Memory Alloy Crystal Structures

The shape memory effect is characterized by three phases—austenite, martensite, and rhombohedral. Austenite, also known as B2, has a CsCl type order. Martensite has a monoclinic or orthorhombic type structure, dependent upon the sample's composition. [4] Rhombohedral or R-phase is composition dependent and appears upon cooling and before the martensitic transformation occurs. [7] The R-phase is seen under certain conditions—when rearranged dislocations are introduced, usually through cold working and a 400°C to 500°C anneal; when solution treatment introduces precipitates and an alloy with 50.5%

nickel is aged at temperatures between 400°C to 500°C; and/or when third alloying elements are included to suppress the martensitic transformation. [8,9] More details about these phases are presented in Figure 1.4 and Table 1.1 below.

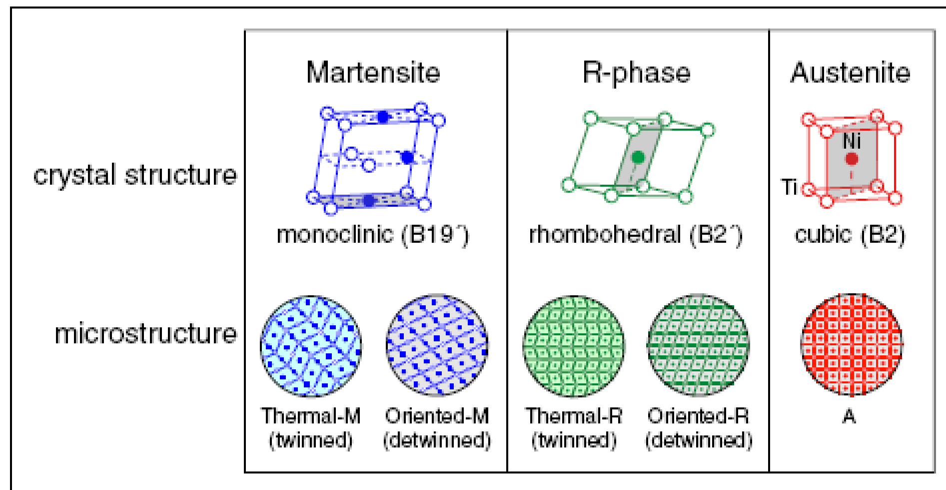

Figure 1-4 Schematic showing the relationship between crystal structure and microstructure. [5]

Phase	Structure	Lattice Parameters	Where seen
B19’ (Martensite)	Monoclinic	a=0.2898 nm b=0.4108 nm c=0.4646 nm β=97.78°	NiTi alloys quenched from B2 parent phase (evident via surface relief)
R	Trigonal	a=0.738 nm c=0.532 nm	In Ti-47Ni-3Fe; Ni-rich NiTi; NiTi if cold worked and annealed
B19 (Martensite)	Orthorhombic	a=0.2881 nm b=0.4279 nm c=0.4514 nm	50Ti-(50-x)Ni-(x)Cu If 5≤x≥7.5
B2 (Austenite)	Cubic	a=0.3015 nm	

Table 1-1 Detailed information about the phases seen during shape memory effect. [7,9]

1.5 The Role of Martensite

In order for an alloy to exhibit shape memory alloy properties, the alloy must have: (1) a parent phase that is ordered, (2) a martensitic phase that is thermoeleastic, and (3) crystallographic reversible martensite. The alloy’s requirement to have an ordered parent is to ensure that slips are avoided and to ensure that a relationship exists to create reversible martensite. An ordered film only has one path to transform to the parent phase. On the other hand, if the

alloy is disordered, three transformation paths would be available and it is possible that the wrong transformation path would be taken. This wrong path would be manifested as the inappropriate parent phase structure change and an increase in the system's energy. [11].

Martensitic transformations occur in two steps—bain strain and lattice invariant shear. Bain strain is a lattice deformation where the atomic shuffle of austenite produces martensite. The lattice invariant shear is an accommodation step to relieve the shape change that has occurred during the Bain strain step. To reduce the strain that may occur during this process, the material must either introduce slip or introduce twinning—neither which alters the martensite's structure. Whether slip or twinning is introduced depends on the alloy system; yet, twinning is more often seen than slip in shape memory alloys. Since slip causes atomic bonds to be broken and is permanent, it is not desired. Twinning is mobile and requires very low energy. This allows it to efficiently accommodate shape changes. [2, 12]

The martensitic transformation results from a homogeneous deformation of the parent phase where the entire material experiences a variety of martensite orientations and size ranges. [1] It forms as thin plates on habit planes which minimizes the strain energy. The habit plane is an interfacial plane between austenite and martensite on a macroscopic scale. [5] The plate's orientation is that of the most energetically stable in the strain field. When unconstrained, the interface plane is flat but when strain energy is being minimized, the plane becomes curved. [7]

For shape memory alloys, when austenite is cooled many variants of martensite are formed and accommodate each other accordingly and thus no shape changes occurs. The application of stress leads to the favored martensite variant growing and shape-changing occurring. The martensite variants have the same structures, but different orientations. This is possible since martensite has a lower symmetry. Strain from one variant offsets the strain from the other variants. It is more energetically favorable to have multiple self-accommodating fields of marteniste growing. Yet, boundaries between them are very mobile and will readily relocate or move when stress is applied. [6] In addition, one or more unrotated, undistorted, invariant lines must be left in order for transformation to occur. Invariant lines are those joining the parent and product phases without rotation or distortion. [7]

1.6 Shape Memory Alloy Behavior

There are two behaviors exploited in shape memory alloys—the shape memory effect and superelasticity. The shape memory effect (SME) happens when tensile testing occurs below the austenite finish temperature and the strains from the testing remain, but they are recoverable when heated above the austenite finish temperature. Deformation applied to the shape memory specimen can be in any form like tension, compression, or bending, as long as it is below a critical value. Superelasticity (SE) occurs when tensile testing is performed above the austenite finish temperature and strains are usually fully recovered by simple unloading. The stress application makes martensite stable,

but once the stress is removed, the martensite is again unstable. Although superelasticity is not the most utilized characteristic of shape memory alloys, it can provide additional memory or force for special purposes. Figure 1.2 shows a comparison between stress-strain plots of SE and SME. [1,2,12]

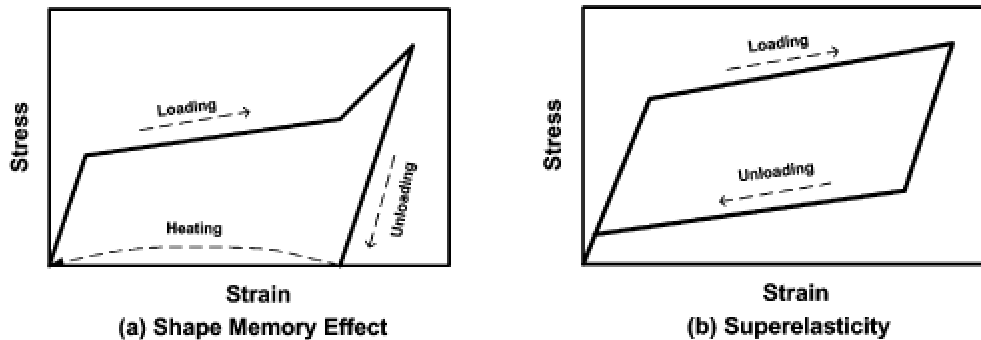

Figure 1-5 Stress-strain schematic comparing shape memory effect to superelasticity. [13]

1.7 Bulk Scale Shape Memory Alloys

Bulk scale shape memory alloys are fabricated using casting, powder metallurgy, forming, and machining. Of these fabrication methods, forming and machining have shown drawbacks—forming leads to high spring-back, die weakening and friction and machining is very difficult and requires very low speeds, large amounts of coolant, rapid tool wear. SMAs are also difficult to mill, drill, and join. For example, joining is difficult because the sister material is not able to withstand the large strains SMA produces. Bulk scale SMAs are available as cold drawn wires, sheets, strips, and tubing.

1.7.1 Bulk Scale Shape Memory Alloy Characterization Methods

In 1965, it was reported that cold work in the martensite phase increased the yield strength of SMA. Without a subsequent annealing step, the SM properties are poor because ‘very low recoverable strains’ are formed. Annealing can “restore the memory effect, but decrease the yield stress” instituting a property trade-off. Therefore, a healthy balance must be reached based upon the required application. (This is the start of the variable processing parameters presented throughout literature.) Another method to control SM properties is through alloying. For example, the inclusion of Fe, Co, or Cr substitute Ni and reduce M_s temperature value. [14]

Shape memory alloy researchers have measured a number of bulk scale properties which are listed in Table 2.1. Of these, the most commonly measured properties on the bulk scale include hardness, yield strength, Young’s modulus, electrical resistance, and deformation abilities. It is very important to note that although these properties have been investigated, SMA characterization and testing has yet to be standardized (ASTM is currently) working on this goal. In addition it is also common practice for each SMA investigative team to test their samples within their own labs with “homemade” testing equipment and produce them with a myriad of processing parameters. [15]

Feel	Acoustic Emission
Ring	Electrical Resistance
Bend	Magnetic Properties
Color	Electromotive Force
Roughness	Thermoelectric Power
Hardness	Hall Coefficient
Expansion	Heat Capacity
Yield Strength	Latent Heat of Transformation
Young's Modulus	Thermal Conductivity
Damping	Lattice Spacing
Internal Friction	Electron Density Waves
Velocity of Sound	

Table 1-2 List of NiTi shape memory alloy properties measured on the bulk scale.

1.7.2 Bulk Scale Shape Memory Alloy Applications

There are four application categories for SMA—free recovery, constrained recovery, actuators, and superelasticity. Free recovery results in motion due to the recovery strain generation (via free recovery during heating). For constrained recovery, large recovery stresses (and not strain) are formed resulting in force. Constrained recovery is the working mechanism behind fasteners and pipe couplings. In the case of actuation, both strains and stresses are recovered during heating resulting in work being done. Superelasticity stores mechanical energy over a rather small temperature range. [16]

Shape memory alloys are desirable for practical applications because they exhibit superelasticity, high corrosion resistance, biocompatibility, and are able to recover large transformation stress and strain upon heating [3]. Since their discovery, SMA have been introduced to several industries—aerospace/aeronautical, medical, industrial/civil engineering, consumer products,

automotive, and electronics. The table below outlines some of the impacted industries and its respective uses. Two of these applications will be discussed in greater detail in the next two paragraphs.

Industry	Use
Aerospace	Flap actuator for aircraft maneuverability Cryofit NiTiFe tube coupling for Us Navy F-14 Frangibolt for space shuttle deployment Rotors to reduce helicopter noise and vibration Helicopter tracking control and wing contour adjustment during flight
Medical	Replace Ti and stainless steel as bone plate material Included in robotic systems used to mimic human functions
Structures	Tendons to limit vibration damage of buildings & bridges Beam-to-column joints for concrete structures
Nuclear Power Plants	Remote temperature sensing Transmission line sag control Ice removal from overhead transmission lines/circuit breakers
Commercial	Eyeglass frame, nose- and earpiece Cell phone antenna Women's brassiere underwire Transmission fluid movement in Daimler-Benz Control of self-cleaning oven door Closing/opening of louvers on automatic fog lights Current interruption mechanism for high density batteries Bumper and body moldings of GM automobiles

Table 1-3 List of SMA applications and their respective industries. [17-19]

The first reported application of the alloy occurred within the aerospace or aeronautical industry that was attracted to their reduced weight, simplicity of design, and reliability. The TiNi Alloy Company developed Frangibolt® Release Bolt to replace the exploding bolt aerospace release mechanism used to remove spacecraft accessories during and after launch. The Frangibolt® Release Bolt would instead be attached to a shape memory cylinder in its martensitic state, activated by an electric heater, expand to a length producing a force larger than 22 kN (5000 lbs), and fracture the bolt. After a successful run with the Clementine in 1994, their incorporation has resulted in the elimination of accidental activation during shipping, potential damage of the spacecraft during explosion, and the off-gassing risks.

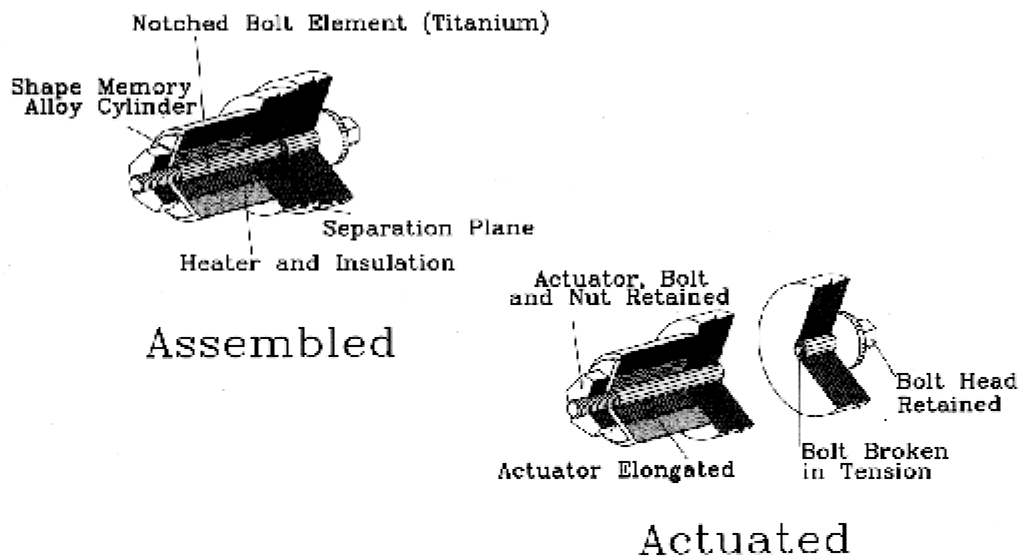

Figure 1-6 Schematic of the Frangibolt release bolt. [17]

In the medical industry, NiTi SMAs are desirable because of its excellent biocompatibility and corrosion resistance. NiTi stents are used to patch lesions and to prop open, to support, and/or to prevent the collapse or blockage of artery walls, ducts, or passageways. SMA stents utilize the functional properties of superelasticity (austenite), thermal shape memory, and low modulus of martensite. In operation, the stent is transformed to the martensite phase by placing it in ice water, compress it, cover it with a protective sheath, and introduce into the body through an opening. Once the stent reaches its proper location, the sheath is removed, and the heat from the body causes it to return to its original shape.

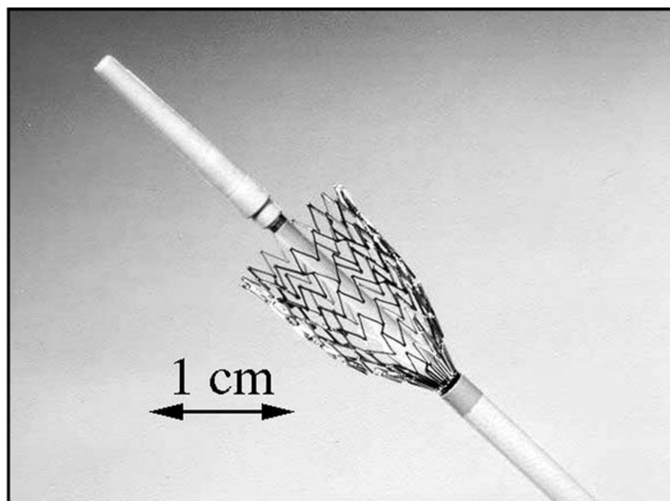

Figure 1-7 Photograph of a stent in its expanded position. [20]

A luxurious application of NiTi shape memory alloy is the Riparian Project, a transformable motor yacht, developed by Adam Voorhees and designed to fuse the relationship between the user, yacht, and current environment. The transformable motor yacht concept is based upon the yacht’s ability to adapt and

physically transform to its current environment using its NiTi structural skeleton featuring active and passive nodes. Advantages include an increase in efficiency by the variable reduction of the yacht's aerodynamic profile, an enhancement of ventilation by its ability to create high and low pressure zones, a temperature variation by the alteration of space volumes. The Riperian boasts of the use of greener technology—hydrogen and solar power—for its power generation. [21]

1.8 Motivation for Project

Although substantial information is available on the mechanical and physical properties of bulk scale shape memory alloys, minimal and inconsistent data is available for thin film shape memory alloys. More specifically, the discrepancy among thermomechanical processing parameters for thin film SMA is a direct result of the variations between research teams and their respectively available equipment. This makes it extremely difficult to rapidly produce SMA films to characterize and apply to microelectromechanical systems (MEMS) devices. Valuable research time is often spent optimizing sputtering parameters when that same time could be focused on other aspects of the thin film shape memory alloy research and applications. In addition, few investigations have characterized films at or below 1 μm thickness. Whenever smaller or thinner films were used, they were often ignored or overlooked due to the researchers' inability to obtain worthwhile or valuable films.

Therefore, an investigation of these films on this scale or lower would be extremely beneficial for the characterization of thin film shape memory alloys and their applications. Possession of the SMA property data on such a small scale will allow researchers to develop MEMS and nanoelectromechanical system (NEMS) devices with better reliability and functionality. Through this research, I will present methods to efficiently fabricate thin film NiTi shape memory alloys and more detailed experimental property data to assist researchers in the application of these unique alloys.

1.9 Research Objectives

Based on the above mentioned issues involving the accurate production and characterization of thin film NiTi shape memory alloys, numerous research objectives have been developed. They include:

a. To develop a systematic approach to producing SMA thin films using design of experiment techniques.
b. To determine the effects of thickness on the property data for films less than or equal to 1 μm.

1.10 References

[1] L.M. Schetky. 'Shape Memory alloys.' *Scientific American.* 241 (1979) 74-82.

[2] C.W. Wayman, T.W. Duerig. "An introduction to Martensite and Shape Memory." *Engineering Aspects of Shape Memory Alloys.* Butterworth-Heinemann. London. 1990.

[3] W. Buehler. "NITINOL Re-examination." WOL Oral History Supplement. *WOLAA Leaf.* 111 (2006) 1-5. <www.wolaa.org>

[4] H. Funakubo. 'Martensitic Transformation.' *Shape Memory Alloys.* Gordon & Breach Science Publishers. New York. 1987.

[5] D. Mantovani. 'Shape Memory Alloys: Properties & Biomedical Applications.' *JOM.* 52 (2000) 36-44.

[6] K. Otsuka, X. Ren. 'Recent developments in the research of shape memory alloys.' *Intermetallics.* 7 (1999) 511-528.

[7] T. Saburi. *Shape Memory Materials.* K. Otsuka & C.M. Wayman (Eds). Cambridge University Press. pp. 49-96.

[8] D.E. Hodgson, M.H. Wu, R.J. Biermann. "Shape Memory Alloys." *Metals Handbook.* Vol. 2. 10th ed. *Properties & Selection: Nonferrous & Special-Purpose Materials.* ASM International. 1990.

[9] K. Otsuka, X. Ren. 'Physical metallurgy of Ti-Ni based shape memory alloys.' *Progress in Materials Science.* 50 (2005) 511-678.

[10] Y. Fu, H. Du, W. Huang, S. Zhang, and M. Hu. 'TiNi-based thin films in MEMS applications: a review.' *Sensors & Actuators A.* 112 (2004) 395-408.

[11] K. Miroslav, P. Mach. *24th International Spring Seminar on Electronics Technology.* May 5-9, 2001. Calimanesti-Caciulata Romania. pp. 42-46.

[12] C.W. Wayman, T.W. Duerig. "An Introduction to Martensite and Shape Memory." *Engineering Aspects of Shape Memory Alloys.* Butterworth-Heinemann. London. 1990. pp.3-20.

[13] W. Huang. "On the selection of shape memory alloys for actuators." *Materials and Design.* 23 (2002) 11-19.

[14] K.N. Melton. ‘NiTi based shape memory alloys.’ *Engineering Aspects of Shape Memory Alloys.* Butterworth-Heinemann. London. (1990) pp.25-35.

[15] J.A. Shaw, C.B. Churchill, M.A. Iadicola. ‘Tips and tricks for characterizing shape memory alloy wire: Part I-Differential scanning calorimetry and basic phenomena.’ *Experimental Techniques.* 32 (2008) 55-62.

[16] J.-L. Seguin, M. Bendahan, A. Isalgue, V. Esteve-Cano, H. Carchano, V. Torra. ‘Low temperature crystallized Ti-rich NiTi shape memory alloy films for microactuators.’ *Sensors and Actuators.* 74 (1999) 65-69.

[17] ‘Aircraft maneuverability.’ Smart Materials & Machines website. <www.cs.ualberta.ca/~database/MEMS/sma_mems?flap.html> Posted 08/17/2001. Accessed 01/26/10.

[18] Wu & Schetky. “Industrial applications for shape memory alloys.” *Proceedings of International Conference on Shape Memory & Superelastic Technology. Pacific Grove, CA. (2000) 1-9.*

[19] A. Lienert. “In GM’s Pipeline: Vehicles that “will drive themselves” says R&D Boss”. Edmunds Inside Line. <http://www.edmunds.com/insideline/do/News/articleId=158189#5>. Posted 09/30/2009. Accessed 09/30/09.

[20] T.W. Duerig. “The Use of Superelasticity in Modern Medicine.” *MRS Bulletin.* February 2002. 101-104.

[21] “Adam Voorhees Unveils the Riparian Project.” Super Yacht Times.com. 08/28/2009. <http://www.superyachttimes.com/editorial/5/print/article/3395 >. Accessed 09/03/2009.

Chapter 2 Nickel Titanium Thin Film Processing Techniques

2.1 NiTi Thin Film Fabrication Techniques

NiTi films produced in the amorphous state were first done by Thomas *et al.* in 1982 using electron irradiation and a high voltage electron microscope. Although these films were amorphous, this was a monumental step in the development of thin film shape memory alloys. Amorphous film production was critical because crystallization of these films will allow the development of films with excellent mechanical properties. In 1983, Sekiguchi *et al.* produced the first crystallized NiTi thin film using vacuum deposition and first confirmed SME in thin films. Four years later, Kim *et al.* used magnetron sputtering to develop films with Ti-56Ni alloy composition. Although the film's composition was not close to the desired equiatomic composition and did not undergo martensitic transformation, their work did verify the possibility of using sputter deposition techniques to produce reliable and sufficient shape memory thin films. [1]

Since this discovery, several methods have been documented that produce thin film shape memory alloys. Popular methods for the production of this film include laser ablation, cathodic arc plasma ion plating, flash evaporation, vacuum evaporation, and sputtering. The above processes have proven unfavorable because they often produce films with non-uniform film thickness

and composition, are incompatible with MEMS processing, and possess low deposition rates. [2] Sputter deposition is often chosen as a production method because of its ability to control film thickness and composition and its ability to produce films with excellent mechanical film properties and extremely fine grain sizes. Sputtering also allows more adherent films to be deposited and allows the production of complex shaped objects. [1, 3]

2.2 Working Mechanism for Sputter Deposition

Evaporation and sputter deposition are physical vapor deposition techniques used to produce thin films. Evaporation involves the thermal absorption of energy to sublime a material in a vacuum environment for film deposition using resistive heating, laser, electron beam, or RF induction methods. Pure metal sources are used to deposit the films because with an alloy the composing materials would evaporate at differing temperatures and be unable to produce equiatomic films. Therefore, sputter deposition is a more suitable deposition method.

Sputter deposition is a method where the target material's surface is bombarded with energetic ions resulting in atom ejection in which they are condensed on the substrate surface. More specifically, the target material or cathode is placed in parallel to the substrate or anode. The cathode is given a highly negative potential by being connected to the negative terminal of the DC power supply and the anode is either grounded, positively or negatively biased,

heated, cooled, or setup in some combination of these. The chamber is then evaporated and a working gas introduced to act as the initiator and sustainer of the electrical discharge or plasma. The plasma results in current flow that allows a momentum transfer where the positive gas atoms strike the cathode and eject neutral atoms from the target that condenses on the substrate's surface. During this process, not only are the target ions ejected, but also secondary electrons, ions, photons, and x-rays. All of these energetic particles can ultimately alter the deposited film properties.

There are four major categories of sputtering process—DC, AC (or RF), reactive, and magnetron. This research work utilizes magnetron sputtering which can be configured in any of these variations. Magnetron sputtering has become the most widely used form of sputtering. Advantages of magnetron sputtering include higher deposition rates, lower voltage operation than traditional DC sputtering, reduced operating pressures, and the avoidance of "gas phase collisions and scattering at high pressure". Planar, cylindrical, and sputter gun are the three configurations that exist. The 3-inch sputter gun setup (which was used in this research) was developed by Peter Clarke in 1968. For this configuration, targets are backside bonded with magnets and placed within the gun source at an angle facing the substrate. This allows the axial B field lines to intersect the ε field lines perpendicularly thereby creating and confining a "toroidial plasma discharge" over the targets surface. The confined electrons help improve the etch rate. [4, 5]

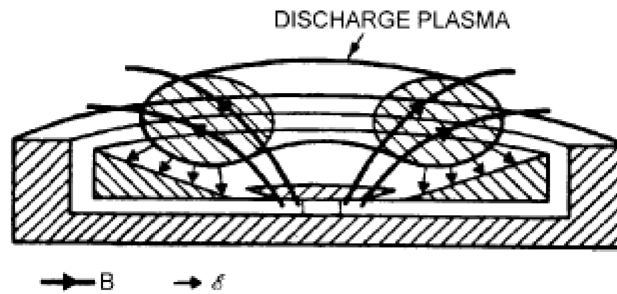

Figure 2-1 Schematic showing the magnetron sputter deposition configuration. [4]

2.3 Deposition Issues for NiTi Shape Memory Films

Although sputtering is the preferred deposition method, there are some intrinsic problems associated with the production of NiTi thin films using this technique. They include sputtering yield differences between nickel and titanium, geometrical composition uniformity over substrates, cross-sectional thickness of coating, and the wear, erosion and roughening of the target during sputtering. Researchers have resolved these problems through co-sputtering and by controlling substrate rotation, precise target position, and sputtering parameters. [2]

Sputtering yield measures how efficient the sputter deposition process is. It is defined as

$$S = (number\ of\ sputtered\ atoms)/\ (incident\ particle). \qquad \text{Equation 2.1}$$

In argon gas atmosphere, Ni has a sputtering yield of approximately 1.45. Ti, on the other hand, has a sputtering yield of approximately 0.51. The differences in

sputtering yields imply that Ni will sputter at a faster rate than Ti. In addition, the differing alloy components require different vapor pressures for evaporation. For these reasons, to obtain the desired equiatomic films, it is imperative that additional Ti be present or utilized. [4]

Processing methods that have been used to address the nickel and titanium sputter yield differences include the: (1) use of co-sputtering techniques, (2) use of a single NiTi target with extra Ti applied as a mesh or chips on the substrate surface, or (3) variation of the chamber's working gas pressure. Altering the chamber's working gas pressure is difficult, in the practical sense, and if raised too high can lead to films with structural defects, brittleness, a low density, and polystructured features. A more practical method involves the use of an additional target or incorporating extra titanium as either a mesh or chips/small plates. If extra titanium is used in the form of mesh, chips, or plates, control of geometry, number, size, position and deposition parameters for the titanium additions are crucial. For that reason, most researchers utilize co-sputtering techniques because it is the more flexible and controllable method to produce equiatomic films. For co-sputtering, researchers have used equiatomic targets alone or some NiTi target in conjunction with Ti plates, Ti pellets, Ti discs, or Ti mesh. The inclusion of addition Ti is required since nickel sputters at a much faster rate than titanium. [6-12]

Thin film sputter deposition of NiTi can result in equiatomic, Ni-rich, or Ti-rich films depending upon the control or lack thereof the sputtering parameters. Equiatomic films exhibit a B2→B19' transformation. The Ni-rich films undergo a

B2→R→B19’ transformation due to the presence of Ti_3Ni_4 precipitates. The precipitate’s density and size are a function of the aging time and temperature. The Ti_3Ni_4 precipitates also cause an increase in the critical slip stress thereby effecting shape memory effect and superelasticity. [13] Ni-rich films resemble bulk materials in their mechanical and transformation behavior and it is impractical to improve upon the SM and SE properties already obtained. On the other hand, Ti-rich films differ on the growth locations of the precipitates. Bulk Ti-rich alloys show precipitation growth at the grain boundaries, but amorphous and crystallized films show precipitation formation intergranularly. At intermediate processing temperatures, Ti_2Ni and Ti-rich plate precipitates are most often seen; at higher temperatures, only Ti_2Ni precipitates are seen. Ti precipitates will most likely precipitate faster since they are 19% larger than Ni atoms. In both Ni-rich and Ti-rich cases, the growth of precipitates allows the manipulation of the SM and SE properties of the produced thin films. [1]

Phase	Structure	Lattice Parameters
Ti_2Ni	Cubic	a=1.132 nm
$TiNi_3$	Hexagonal	a=0.5101 nm c=0.8307 nm
Ti_2Ni_3 (high temperature)	Tetragonal	a=0.3095 nm c= 1.3585 nm
Ti_2Ni_3 (low temperature)	Orthorhombic	a=0.4398 nm b=0.4370 nm c=1.3544 nm
Ti_3Ni_4	Rhombohedral	a=0.670 nm α=113.8°

Table 2-1 Lattice parameters and information about the precipitates often found in SMA following processing. [1]

High quality NiTi films are produced when they do not have any microscale defects (such as cracks or pores), hydrogen, or oxygen present. The presence of these defects within the films will produce brittle films and any stress application will result in fracture. S. Miyazaki reported that for sputter deposited films, the shape memory characteristics depend greatly upon the argon gas pressure, sputtering power, target purity, deposition environment substrate-to-target distance, substrate temperature, alloy composition, annealing temperature and time. [13, 14] Flat and featureless structures are the result of low Argon gas

pressure usage. At low argon gas pressure, there are few collisions between the molecules which results in the electrons arriving at the substrate surface with high energy. In this state, the compressive stresses increases. On the other hand, high Argon gas pressure results in a columnar film structure and restricted mobility of the deposited atoms lead to a decrease in the energy of sputtered atoms. Films deposited at high gas pressures are less dense and have lower compressive stresses than those deposited at low argon gas pressure. [13,15] Shih *et al* showed that with 1 or 2 μm thick films produced using an unheated or 230°C substrate with an Ar pressure greater than 3.5 mTorr, films with surface cracking was produced. In addition, films deposited at pressures greater than 7.0 mTorr also showed cracked surfaces due to the columnar-like microstructure. [15] Gong *et al* presented that the method to obtain crack-free films was through the usage, of substrates with extremely rough surfaces causing strong adhesion properties between the film and substrate. This strong adhesion may also result in the increase of the crystallization temperature. In comparison, the use of too smooth substrate surfaces may result in cracked films. To obtain optimal films, there must be a balance between the smoothness and roughness of the substrate. [16]

To obtain NiTi films that exhibit SME, the film's processing history is very important and the resultant alloy composition plays a critical role in the definition of the transformation temperatures. If NiTi films are sputtered at room temperature, they will have an amorphous structure and are unable to exhibit SME. Amorphous films require the application of some heat treatment schedule

to crystallize these films. The schedule needed to accomplish crystallization has varied significantly between research teams due to equipment availability, desired film composition, and anticipated application. Annealing temperatures have ranged from 300°C to 800°C. In addition, a number of annealing locations have been reported such as inside the sputtering chamber immediately following deposition or a remote vacuum furnace. For example, Gill, Ho and Carman sputtered 2.5 μm thick 50.8 at% Ni-Ti films on an unheated substrate followed by an *in situ* anneal for 500°C for 10 minutes for the production of a three dimensional microactuator. [17] On the other hand, Sanjabi *et al* sputtered 47.2 at% to 51.2 at% Ni-Ti films followed by an *ex situ* 500°C anneal for 60 minutes using a remote vacuum furnace. Despite the annealing location chosen, it is important that the lowest temperature be used to hinder the occurrence of any type of reactions between the NiTi film and the silicon substrate. [6] Without this consideration, the researcher would run the risk of forming unwanted precipitates.

2.4 References

[1] K. Otsuka, X. Ren. 'Physical metallurgy of Ti-Ni based shape memory alloys.' *Progress in Materials Science.* 50 (2005) 511-678.

[2] Y. Fu, H. Du, W. Huang, S. Zhang, and M. Hu. 'TiNi-based thin films in MEMS applications: a review.' *Sensors & Actuators A.* 112 (2004) 395-408.

[3] K. Miroslav, P. Mach. *24th International Spring Seminar on Electronics Technology.* May 5-9, 2001. Calimanesti-Caciulata Romania. pp. 42-46.

[4] M. Ohring. *Materials Science of Thin Films: Deposition & Structure*, 2nd ed. Academic Press. San Diego. 2002.

[5] M.J. Madou. *Fundamentals of Microfabrication: The Science of Miniaturization.* 2nd ed. CRC Press. Boca Raton. 2002.

[6] S. Sanjabi, S.K. Sadrnezhaad, K.A. Yates, and Z.H. Barber. 'Growth and characterization of Ti_xNi_{1-x} shape memory thin films using simultaneous sputter deposition from separate elemental targets.' *Thin Solid Films.* 491 (2005) 190-196.

[7] E. Wibowo, C.Y. Kwok. 'Fabrication and characterization of sputtered NiTi shape memory thin films.' *Journal of Micromechanics & Microengineering.* 16 (2006) 101-108.

[8] Y.H. Li, L.M. Li, F.L. Meng, W.T. Zheng, J. Zhao, Y.M. Wang. 'Effect of substrate temperature on the surface and interface oxidation of NiTi thin films.' *Journal of Electron Spectroscopy & Related Phenomena.* 151 (2006) 144-148.

[9] J.-L. Seguin, M. Bendaham, A. Isalgue, V. Esteve-Cano, H. Carchano, and V. Torra. 'Low temperature crystallized Ti-rich NiTi shape memory alloy films for microactuators.' *Sensors & Actuators.* 74 (1999) 65-69.

[10] J.P. Chu, Y.W. Lai, T.N. Lin, S.F. Wang. 'Deposition and characterization of TiNi-base thin films by sputtering.' *Materials Science and Engineering A.* 277 (2000) 11-17.

[11] A. Ishida, M. Sato, S. Miyazaki. 'Mechanical properties of Ti-Ni shape memory thin films formed by sputtering.' *Materials Science & Engineering A.* 273-275. (1999) 754-757.

[12] P. Surbled, C. Clerc, B. Le Pioufle, M. Ataka, H. Fujita. 'Effect of the composition and thermal annealing on the transformation temperatures of

sputtered TiNi shape memory alloy thin films.' *Thin Solid Films.* 401 (2001) 52-59.

[13] S. Miyazaki, A. Ishida. 'Martensitic transformation and shape memory behavior in sputter-deposited TiNi-based thin films.' *Materials Science & Engineering A.* 273-275 (1999) 106-133.

[14] S. Miyazaki, M. Fremond. *Shape Memory Alloys.* Springer. New York. 1996.

[15] C.-L. Shih, B.-K. Lai, H. Kahn, S.M. Phillips, A.H. Heuer . 'A robust co-sputtering fabrication procedure for TiNi shape memory alloys for MEMS.' *Journal of Microelectromechanical Systems.* 10 (2001) 69-79.

[16] F.F. Gong, H.M. Shen, Y.N. Wang. 'Fabrication and characterization of sputtered Ni-rich NiTi thin films.' *Materials Letters.* 25 (1995) 13-16.

[17] J.J. Gill, K. Ho, G.P. Carman. 'Three-dimensional thin-film shape memory alloy microactuator with two-way effect.' *Journal of Microelectromechanical Systems.* 11 (2002) 68-77.

Chapter 3 Current Nickel Titanium Thin Film Applications

3.1 Current Nickel Titanium Thin Film Applications

In addition to the previously mentioned desirable properties of NiTi thin film SMA, their ability to undergo patterning techniques and batch fabrication have made them a promising candidate for MEMS applications. Yet, the community's inability to fully understand the working mechanism and control of the deposition parameters of thin film SMA, have retarded the widespread application of this film. Fu *et al.* presented a number of basic requirements for the successful use of thin NiTi films as MEMS devices. They reported that effective SMA thin films must possess (1) low residual stress to prevent deformation of MEMS structure; (2) high actuation speed and fast response with precise control of deformation and strain; (3) good adhesion onto the substrate (free of cracking, delamination, and spallation); (4) durable and reliable shape memory effects; (5) wide range choice of working temperatures (from below zero to several hundred degree Celsius); (6) good resistance to surface wear and corrosion; and (7) biocompatibility and good corrosion resistance especially for bio-MEMS. [1]

The most common device or class of devices fabricated in thin film form for MEMS applications are the microactuators. An actuator is defined as a mechanical device used for moving or controlling some object. Commonly used

criteria to evaluate actuators include their work, power density, time constants, accuracy, efficiency, and service life.[2] Researchers have found that the incorporation of NiTi into MEMS devices as an actuator is extremely beneficial because they possess a large work density, produce a large strain output, have a high-frequency response, and utilize Joule heating activation. [3] Microactuation applications for NiTi thin films include micropumps, microvalves, microgrippers, springs, microspacers, micropositioners, and microwrappers. Table 2.3 shows the relationship between several actuation types and real world applications. [1]

Actuation Type	**Real Life Application**
Micropump Microvalves	Implantable drug delivery Chemical analysis Analytical instruments
Microgrippers	Microsystem Assembly Endoscopes (for Microsurgery) Drug Injection micromanipulators
Microswitches Microrelayes	On-chip circuit breakers Probe tips for automatic test equipment Fiber optics switching Automotive fuel injectors Micro-lens positioners

Table 3-1 Relationship table between MEMS actuation type and potential applications.

The first interaction between SMA and microelectronic fabrication techniques occurred when Walker *et al.* in the early 1990s produced thin film NiTi shape memory alloy coil springs on a silicon wafer. Walker's research proved to the community that these films are compatible with the fabrication of Microelectromechanical Systems (MEMS). Another breakthrough in this area occurred when Bernard *et al.* implemented thin film NiTi SMA as an actuator to improve MEMS-based microfluidics devices (refer to Figure 3.1). Of the commonly used actuation methods, this research group believed that the shape memory microactuation would provide high enough strains and forces to produce actuation work densities two orders of magnitude higher than those seen in other actuation mechanisms like piezoelectricity. They also believed that it would produce higher fluid volumes pumped per pump cycle through the microfluidic device. This team microfabricated a 3 μm thick NiTi actuator to include within the reciprocating pumps of the microfluidic device (featuring a deformable chamber and two check valves). Contraction of the pump chamber results in fluid being forced out of the outlet check valve and the inlet check value stops fluid from flowing back into the reservoir. [4]

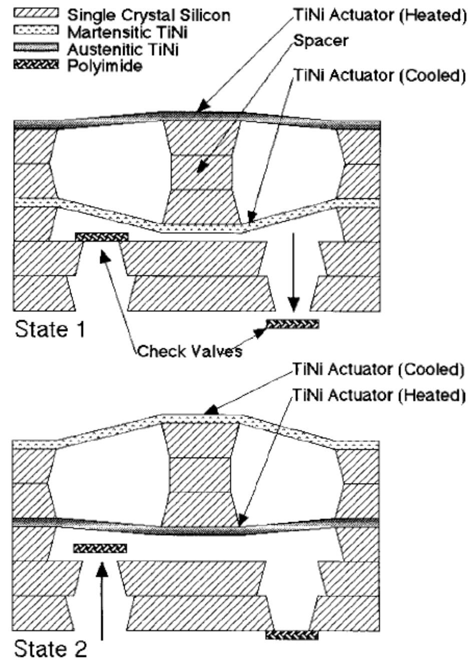

Figure 3-1 Illustration of the actuator micropump developed by Bernard *et al.*[4]

A unique thin film application of NiTi shape memory alloy is a microwrapper developed by Gill *et al.* The microwrapper, seen in Figure 3.2, has potential applications in the biomedical field such as to grab objects like cancerous tumors within living organisms. Prior to the incorporation of the film into the device, the film was characterized using wafer curvature (for transformation temperatures), SEM (to evaluate film integrity before and after processing techniques), and the Timoshenko beam equation (to calculate the degree of curvature of the arms). Following the release of the arms from the substrate, the residual stresses from microprocessing causes the arms to curl up and form a cage-like structure. Upon the application of Joule heating (around 400 mW), the arms return to their original flattened position. The removal of the

current in addition to heat dissipation, forces the arms to return to their original curled up state. [5]

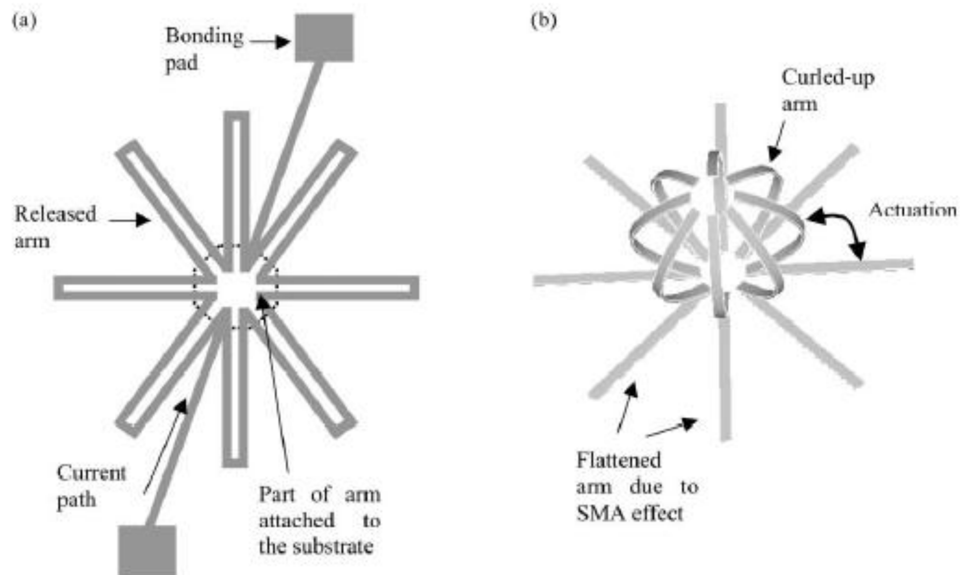

Figure 3-2 Illustration of the microwrapper developed by Gill, *et al.* [5]

In 2004, Huang *et al.* fabricated a three position NiTi-Si cantilever system which was flat at room temperature and curved when electrical current or heat was applied. Two characterization tests were used to investigate the magnitude of the tip's deflection. In the low speed test, heat was applied and the tip moved downward; when it cooled, the tip returned to its original position. In the high speed test, a constant current of 0.6 mA was applied for 10 seconds and removed. The tip moved downward during the first five seconds, upward during the following 5 seconds, and after current removal the tip moved back downward to its original position. In both tests, the maximum deflection upward and downward deflection was approximately 1.1 mm and 1.5 mm, respectively. One

drawback from this investigation was that the electrical current heating produced uneven heating distribution, especially during the high speed testing cycle. [6]

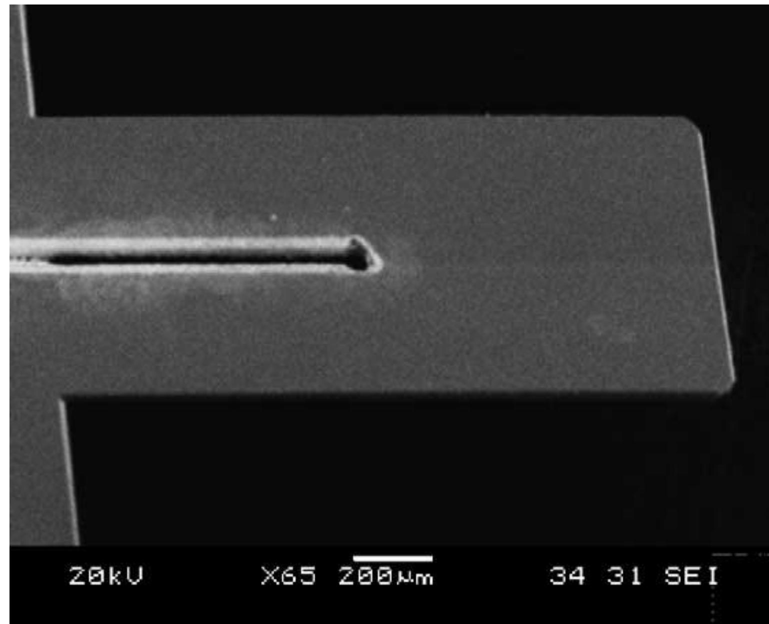

Figure 3-3 NiTi–Si cantilever with a slot cut out by a femtosecond laser. [6]

Zhang, Cheng, and Grummon investigated, in 2007, the use of NiTi films as an interlayer between metal substrates and hard coatings for the enhancement of coating adhesion and the protection of the underlying metal from plastic deformation. Through their exploitation of the SMA indent recovery ability, they anticipate future applications to include information storage, smart tribiological surfaces (friction and wear control), optical communication devices, and microfluidic instruments. The investigated interlayer system consisted of surface polished 6061-T6 aluminum substrate and 15-21 μm thick $Ni_{48.3}Ti_{51.7}$ film with either CrN or diamond like carbon (DLC) coatings. Acoustic emissions,

temperature scanning ball-on-disk wear, and scratch-load testing were used to determine the robustness of the film system. [7]

In 2008, Chan, Chung, and Ng explained their work investigating the application of 5 μm thick NiTi films as the sensing element for the detection of infrared radiation. They microfabricated a micro-array of 50 μm by 100 μm NiTi cantilever's which underwent constraint and heat treatment conditions to induce the two-way shape memory effect at room temperature. During operation, the IR source was focused onto a portion of the micro-array, producing an 8° increase, and resulting in the cantilevers to curl up and reduce the intensity of the focused IR beam. Once the IR beam was removed, the cantilever's returned to their original position and IR beam to its original beam intensity. NiTi was attractive for this application due to its possible cost effectiveness and design simplicity (since other designs require additional material to utilize the coefficient of thermal mismatch for cantilever actuation). [8]

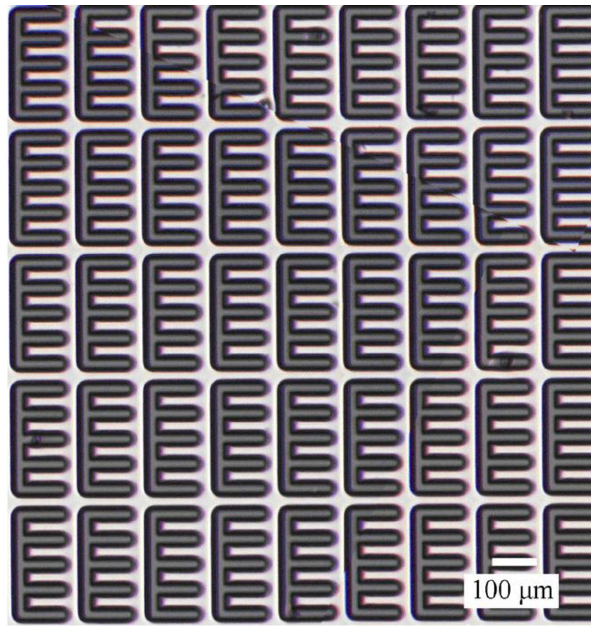

Figure 3-4 SEM micrograph of a NiTi SMA cantilever micro-array. [8]

To respond to the need for a catheter device with a smaller size and larger actuation force, M. Komatsubara, *et al.* developed a three-dimensional deposition system for the fabrication of this micro-catheter. In 2009, they reported on the development of a micro-catheter with four independently and electrically driven zigzag spring-like shaped NiTi actuators fixed onto an elastic shaft. Steps used to produce the catheter include (1) buffing the Cu shaft surface, (2) depositing NiTi via the 3-D sputtering system, (3) patterning of the zigzag , spring-like shapes, (4) etching with HF and HNO3 to remove the Cu shaft and acetone lift-off to remove the remaining PR. The deposited film was characterized as being 5 ± 0.05 μm thick, having a Ni-50 to 50.3 atomic percent Ti composition, and austenite phase presence at the 100°C testing temperature. [9]

Figure 3-5 Schematic and photograph of zigzag shaped spring [9]

3.2 References

[1] Y. Fu, H. Du, W. Huang, S. Zhang, and M. Hu. 'TiNi-based thin films in MEMS applications: a review.' *Sensors & Actuators A.* 112 (2004) 395-408.

[2] M. Kohl. *Shape Memory Microactuators.* Springer. Berlin. 2004.

[3] J. Gill, K. Ho, G.P. Carman. 'Three-dimensional thin-film shape memory alloy microactuator with two-way effect.' *Journal of Microelectromechanical Systems.* 11 (2002) 68-77.

[4] W.L. Benard, H. Kahn, A.H. Heuer, M.A. Huff. 'Thin-film shape-memory alloy actuated micropumps.' *Journal of Microelectromechanical Systems.* 7 (1998) 245-251.

[5] J.J. Gill, D.T. Chang, L.A. Momoda, G.P. Carman. 'Manufacturing issues of thin film NiTi microwrapper.' *Sensors & Actuators A.* 93 (2001) 148-156.

[6] W.M. Huang, Q.Y. Liu, L.M. He, J.H. Yeo. "Micro NiTi-Si cantilever with three stable positions." *Sensors and Actuators A.* 114 (2004) 118-122.

[7] Y. Zhang, Y.-T. Cheng, D.S. Grummon. "Novel tribological systems using shape memory alloys and thin films." *Surface & Coatings Technology.* 202 (2007) 998-1002.

[8] P.M. Chan, C.Y. Chung, K.C. Ng. 'NiTi shape memory alloy thin film sensor micro-array for detection of infrared radiation.' *Journal of Alloys and Compounds.* 449 (2008) 148-151.

[9] M. Komatsubara, T. Namazu, H. Nagasawa, T. Tsurui, S. Inoue. 'Cylindrical film deposition system for three-dimensional titanium-nickel shape memory alloy microstructure.' *Vacuum.* 83 (2009) 703-707

Chapter 4 Nickel Titanium Thin Film Characterization

As previously mentioned, the use of sputter deposition to deposit NiTi thin films without subsequent heat treatments can result in the production of amorphous films. With the possibility of manufacturing amorphous NiTi thin films, additional characterization methods are required to ensure crystallinity. Wibowo and Kwok deposited 3 μm thick Ti-rich NiTi films on silicon substrates and used an electron microprobe analyzer (EPMA) to determine film composition; X-ray diffraction (XRD) to determine the film's crystal structure; nanoindentation to gather information about Young's modulus; and Stoney's equation to calculate the film's residual stress. [1] He et al. used atomic force microscopy (AFM) to characterize the surface roughness of their NiTi films and to determine the transformation temperatures. They also used differential scanning calorimetry (DSC) to gather information on the transformation temperatures. [2] Fu et al. characterized their 5 μm thick films using energy dispersive x-ray spectroscopy (EDS) for film composition; scanning electron microscope (SEM) and AFM to get information about the films' surface morphologies; nanoindentation to explore Young's modulus and hardness; grazing incidence x-ray diffraction (GIXD) for information on the film's crystal structure; and DSC to measure the transformation temperatures. [3]

Other conventional methods used to distinguish amorphous films from crystalline films include atomic composition, crystal structure, transformation temperature, residual film stress, yield strength, Young's modulus, hardness, and surface roughness. The remainder of this chapter will present information to discuss the relationship between SMA and these characterization methods used in this research work.

4.1 X-Ray Diffraction and NiTi Thin Films

A simple method to gain insight about the crystal structure of a material is through the use of x-ray diffraction (XRD). This experimental technique focuses a monochromatic x-ray onto the surface of a material and collects the diffracted beams. These diffracted beams consist of a sizeable number of scattered rays mutually reinforcing each other to display an interaction between the focused or transmitted x-rays. The atoms of the material must satisfy Bragg's Law in order for diffraction to occur. Bragg's Law is defined by Equations 4.1 to 4.3 (Equation 4.3 is the most commonly used variation of Bragg's Law):

$$n\lambda = 2\, d' \sin\theta$$

Equation 4.1

$$\lambda = 2\,(d'/n) \sin\theta$$

Equation 4.2

$$\lambda = 2\, d \sin\theta$$

Equation 4.3

where n=the order of diffraction, d=interplanar distance, λ= wavelength, and θ=diffraction angle or Bragg's angle. It is important to note that the incident beam and diffracted beam are always coplanar. The transmitted beam and diffracted beam always share a 2θ relationship. The atom position within the unit cell determines the diffracted beam's intensity. The shape and size of the unit cell are the only factors used to determine the direction of the diffracted beam. Figure 4.1 presents the schematic showing the working principle of XRD.

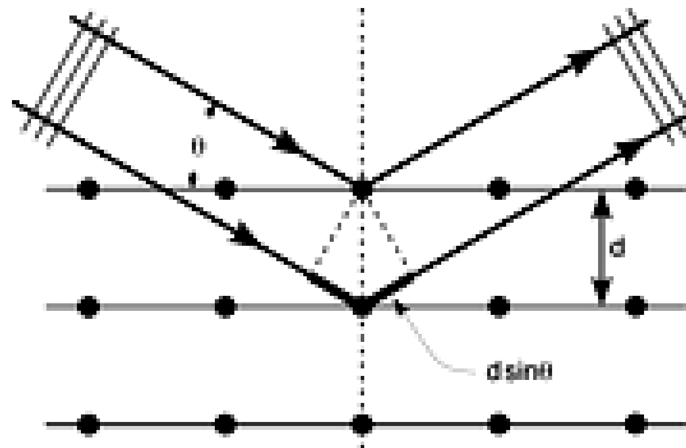

Figure 4-1 Schematic showing the relationship between XRD and lattice atoms. [4]

X-ray diffraction patterns are unique to the substance being investigated and each substance presents the same pattern. Amorphous or liquid samples lack periodicity and order which results in XRD scans featuring curves with one or two maxima. Single crystalline materials produce x-ray scattering in all directions, while polycrystalline samples show scattering in few directions. The periodic array in polycrystalline materials results in destructive interference in all

directions except those satisfying Bragg's Law. The constructive interference of diffracted beams that satisfy Bragg's Law show peaks or what is also known as high sharp maxima. [5]

Since it is possible to produce amorphous films during processing, a rapid way to determine if the film has been crystallized is using XRD. An amorphous NiTi XRD scan is described by a broad peak and can be seen below in Figure 4.2. The figure shows before NiTi thin films have been crystallized, the XRD scan possesses a broad peak; yet, after crystallization, NiTi phase descriptive peaks can be seen. In addition to proving or disproving crystallinity, XRD is also used to determine the dominant phases at various temperatures. The phases present are mostly reflective of the film's composition, substrate temperature during deposition, and annealing temperature and time.

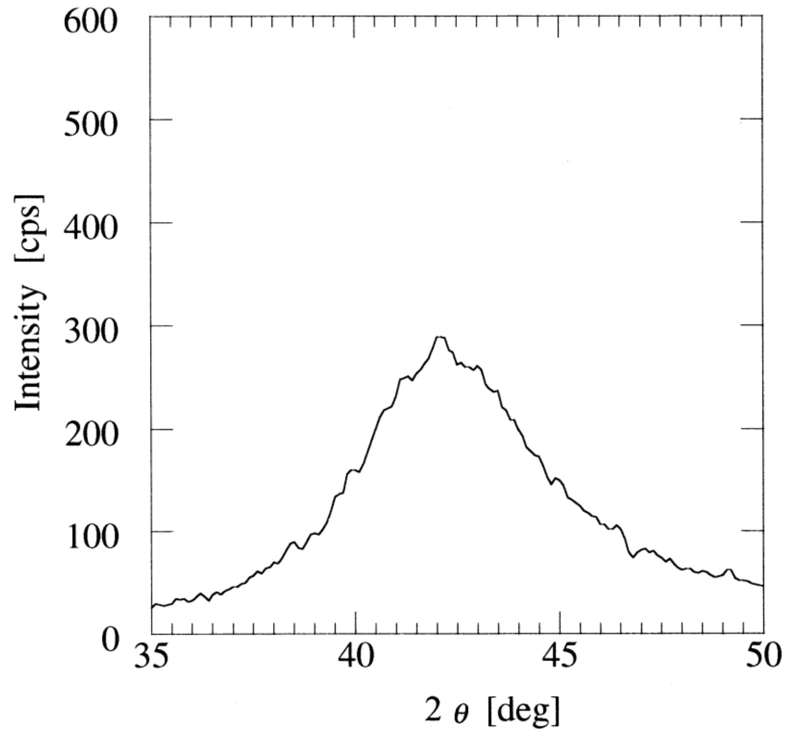

Figure 4-2 Amorphous NiTi thin film XRD scan showing a single broad peak [6]

Thus far for NiTi thin film production, each research team uses their own individual processing parameters that vary depending upon the equipment they have available and the goal of their research. Therefore, researchers have presented the XRD scans in several formats and a few can be seen in figure 4.3. JJ Gill et al. (refer to Figure 4.3a) and CL Shih et al. (refer to Figure 4.3 b) both presented a single XRD scan for a 2.5 μm thick near equiatomic NiTi films exhibiting mixed-phases at room temperature. On the other hand, W Huang et al. (refer to Figure 4.3c) and A Kumar et al. (refer to Figure 4.3d) presented multiple scans to show the phase transformations of NiTi as the temperature changes. [7-10]

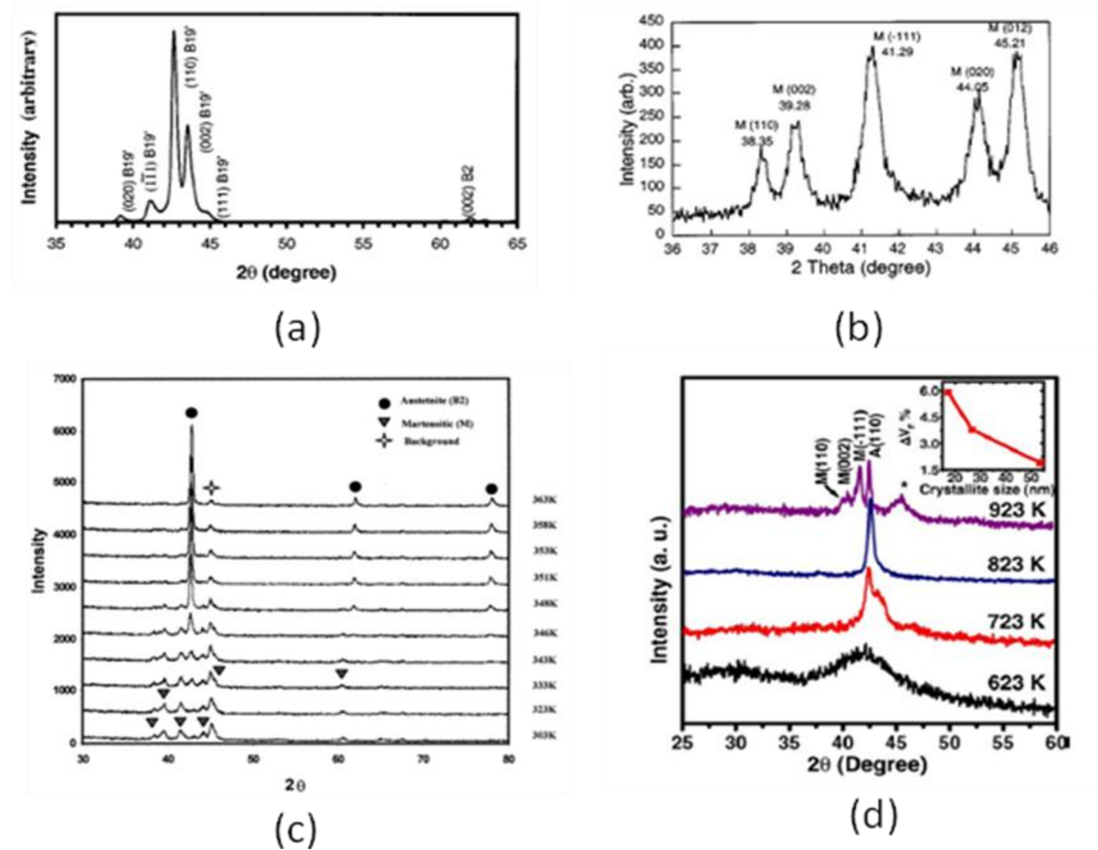

Figure 4-3 Examples of XRD scan samples of NiTi thin films presented in literature: (a) JJ Gill *et al.* 2.5 μm thick film (b) CL Shih *et al* 2 μm thick film (c) W Huang *et al* 5 μm thick film (d) A Kumar *et al* 5 μm thick film [7-10]

4.2 Scanning Electron Microscopy and NiTi Thin Films

Two types of surface observations options have been presented in literature—those that show the surfaces of films following varying processing techniques and those that present the surfaces of MEMS devices. Kumar et al. presented SEM micrographs of 2 μm thick NiTi films deposited using differing substrate temperatures. The surfaces of the four samples can be seen in Figure

4.4. It is believed that the featured surface resulted from a combination of the increased substrate temperature during deposition and the crystallization temperature. [9] JJ Gill et al. imaged the film surface of a 1 μm thick NiTi film patterned by ion milling for the production of their microwrapper. The film was deposited with a substrate temperature of 350°C to reduce residual stress and underwent a 500°C, 6 minute anneal to minimize precipitates. Figure 4.5 illustrates the featureless microwrapper's surface. [11]

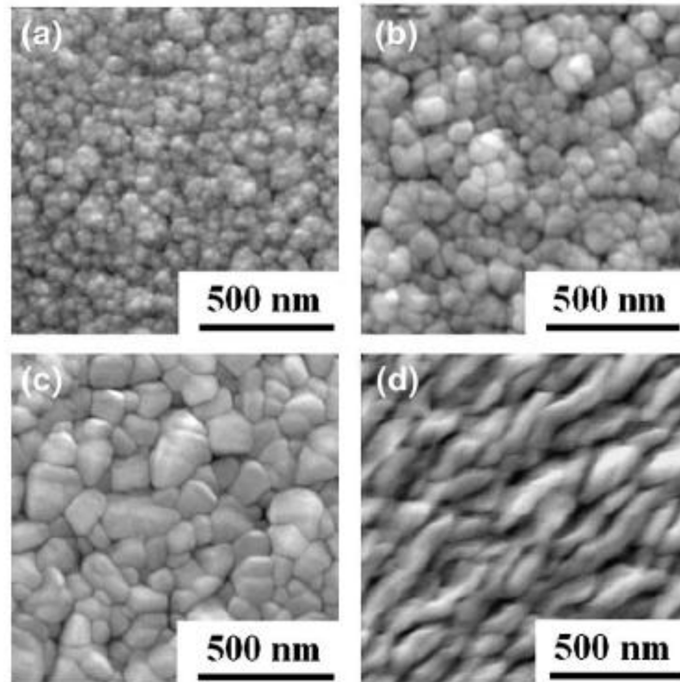

Figure 4-4 SEM micrographs of NiTi films deposited by Kumar et al. at various temperatures: (a) 350°C, (b) 450°C, (c) 550°C, (d) 650°C [9]

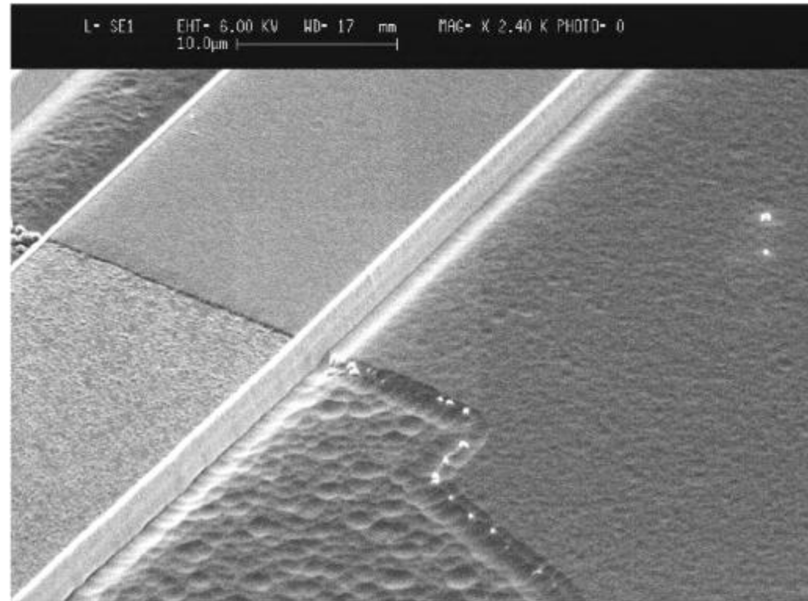

Figure 4-5 SEM micrograph showing the surface of the microwrapper produced by JJ Gill et al. [11]

4.3 Energy Dispersive X-Ray Spectroscopy and NiTi thin films

Energy dispersive x-ray spectroscopy (EDS) is a rapid evaluation method used to gather information on the elemental constituents of a sample. The currently employed EDS system is derived from Fitzgerald's 1968 energy-resolving x-ray spectrometer featuring a silicon, lithium-drifted solid state detector attached to an electron beam microanalyzer. Even though this crude system was unable to resolve neighboring elements, it did exhibit the coupling capabilities of the EDS system with the Electron Beam Microanalyzer or SEM interfaces. Each element has its own unique structure and the unique x-ray generation from the focused beam allows scientists to chemically analyze samples. Elements from beryllium (Be) to uranium (U) can be detected, but it is usually difficult to distinguish elements with atomic numbers lower than carbon (C). Typical EDS

applications include' foreign material analysis, corrosion evaluation, coating composition analysis, rapid material alloy identification, phase identification and distribution, and small component analysis.'

There are four components that make up the EDS system—beam source, x-ray detector, pulse processor, and analyzer. Figure 4.8 shows a modern schematic of the EDS system. A beam of x-rays, created by the SEM's magnetic lenses, are focused onto the sample where the beam excites an inner shell electron. The excited electron is ejected from its shell thereby creating a hole. An outer electron from a higher energy shell fills the hole and the resulting energy level difference (between the higher and lower shell levels) releases an x-ray. The released x-ray passes through the thin Beryllium (Be) window of the x-ray detector. The p-i-n (also known as p-type, intrinsic, n-type) lithium drifted silicon detector has a reversed bias and is cooled (usually by $LN_{2)}$ and sealed under vacuum to prevent contamination, reduce noise, and limit lithium-ion mobility. The detector records the number of x-rays and the energy of these emitted x-rays. Each x-ray photon absorption is followed by a photoelectron ejection forming electron-hole pairs that scatter inelastically. The applied bias sweeps away the electron-hole pairs to form a charge pulse which is converted to a voltage pulse by a charge-sensitive preamplifier. Once additionally amplified, the signal travels to the multichannel analyzer (MCA) which sorts them by voltage and displays them. [12]

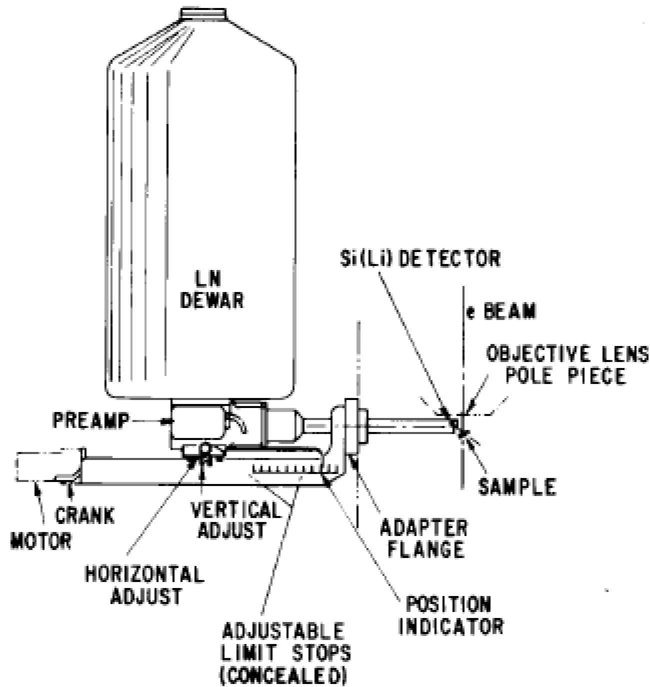

Figure 4-6 Modern EDS system schematic as outfitted with a SEM. [12]

The composition of a sputter deposited NiTi film depends upon the sputtering parameters, as well as the subsequent heat treatment application. However when NiTi thin film composition is investigated, it is never done alone—always in conjunction with some other analysis. For example, P Surbled et al produced NiTi thin films with varying compositions and heat treatments ranging from 420°C to 750°C for 15 minutes to investigate the changes in transformation temperatures. They found that Ti-rich films' transformation temperature mainly depends upon the annealing temperature, but the same is not true for Ni-rich films. A plot exhibiting this can be seen in Figure 4.6 below. [13] As another example, Sanjabi et al used EDS to investigate the change in composition across a substrate based upon the variation of sputtering parameters—substrate

rotation and differing target powers. The results from this study aided the team in the development of initial sputter deposition parameters. [14]

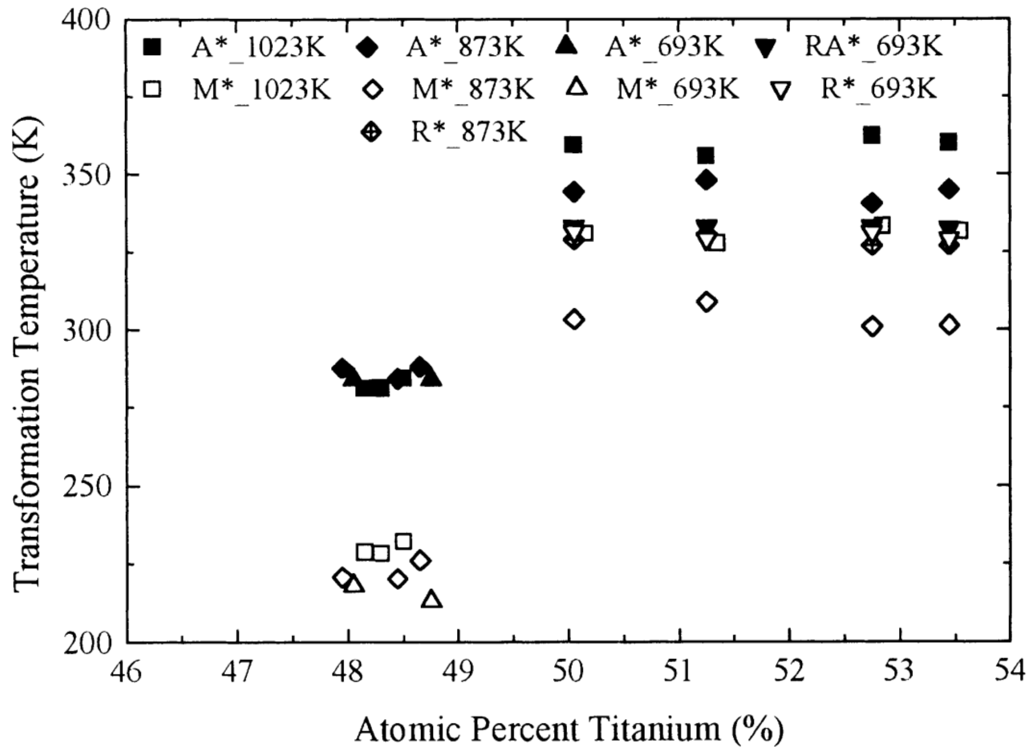

Figure 4-7 Plot describing the relationship between NiTi film composition and transformation temperature. [13]

4.4 Nanoindentation and NiTi Thin Films

Nanoindentation is an ultra-low load variation of the conventional instrumented indentation testing technique. Nanoindentation testing requires minimal sample preparation and is ideal for thin films, coatings, and surface layers. In addition, the use of this technique removes the need for impression imaging and surface layer removal from the substrate.

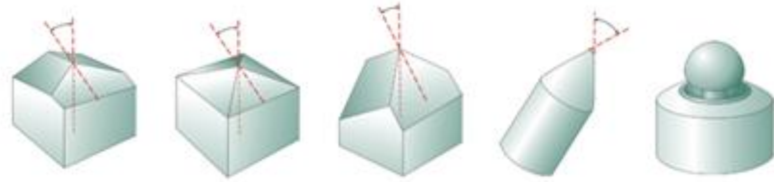

	Berkovich	Vickers	Cube-Corner	Cone (angle ψ)	Sphere (radius R)
Features					
Shape	3-sided pyramid	4-sided pyramid	3-sided pyramid w/ perpendicular faces	Conical	Spherical
Applications	Bulk Materials, Thin Films, Polymers, Scratch Testing, Wear Testing, MEMS, Imaging	Bulk Materials, Films and Foils, Scratch Testing, Wear Testing	Thin Films, Scratch Testing, Fracture Toughness, Wear Testing, MEMS, Imaging	Modeling, Scratch Testing, Wear Testing, Imaging, MEMS	MEMS
Available as Traceable Standard	Yes	Yes	Yes	No	No
Parameter					
Centerline-to-face angle, α A	65.3°	68°	35.2644°	—	—
Area (projected), A(d)	$24.56d^2$	$24.504d^2$	$2.5981d^2$	πa^2	πa^2
Volume-depth relation, V(d)	$8.1873d^3$	$8.1681d^3$	$0.8657d^3$	—	—
Projected area/face area, A/A_f	0.908	0.927	0.5774	—	—
Equivalent cone angle, ψ	70.32°	70.2996°	42.28°	ψ	—
Contact radius, a	—	—	—	d tan ψ	$(2Rd-d^2)^{1/2}$

Table 4-1 Information about commonly used nanoindenter tips. [15]

Nanoindentation systems require three major parts: (a) a means to provide sample translation, (b) a means to apply force, and (c) a means to measure displacement. Figure 4.7 provides a schematic of the indentation system. The indentation process is based upon the application and removal of the indenter. During the indenter's application, elastic and plastic deformation occurs revealing a hardness impression that conforms to the indenter's shape at some contact depth. Once the indenter is removed from the surface, the elastic deformation is recovered, and the indentation depth is measured. Numerous indenter

geometries are available and the applied indenter varies according to the application. Table 4.1 presents the differences between these indenters. [16-18]

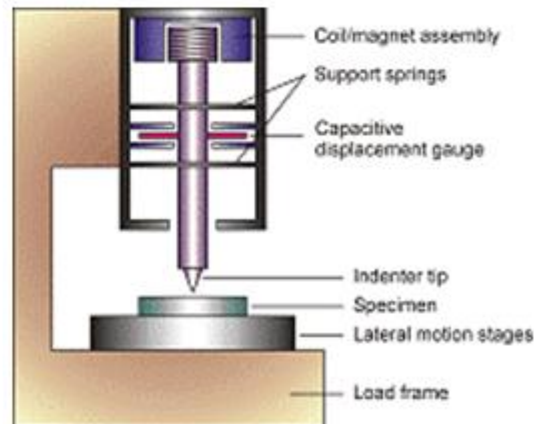

Figure 4-8 Schematic of typical nanoindentation system. [17]

Besides the simple hardness testing method described above, another common measurement technique is the Continuous Stiffness Measurement (CSM). CSM provides a continuous contact stiffness measurement during loading by superimposing a small oscillation on the primary loading signal and using a frequency specific amplifier to analyze the resulting response. In doing so, continuous load-displacement data can be achieved. Use of this continuous indentation mode can be used to determine additional properties, such as the strain hardening exponent, fracture toughness, and the magnitude and sign of pre-existing residual stress. Typical responses seen with this method are shown in Figure 4.8.

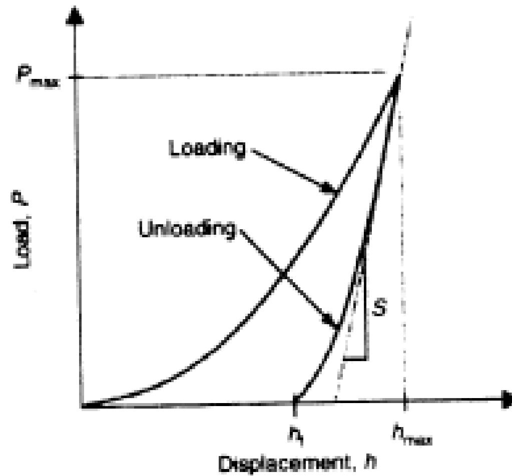

Figure 4-9 Common presentation of data obtained from nanoindentation tests. [17]

The material's hardness, H, is calculated by

$$H = \frac{P}{A}$$

Equation 4. 4

where P is the load applied.

The reduced modulus, E_r, is calculated by

$$Er = \frac{[(\sqrt{\pi})S]}{[2\beta(\sqrt{A})]}$$

Equation 4.5

where β=indenter based constant; =1 for circular, 1.012 for Vickers, & 1.034 for Berkovich and cube-cornered indenters.

And finally the material's young's modulus by

$$\left(\frac{1}{Er}\right) = \left[\frac{1-v2}{E}\right] + \left[\frac{1-vi2}{Ei}\right] \qquad \text{Equation 4.6}$$

where E_i and v_i describe the indenter's values and E and v describe the material's values. [18]

Two types of tests for NiTi SMA thin films have been presented in literature—those that extract material property data and those that utilize the indenter system for its impression abilities. Shaw and constituents used the nanoindenter in conjunction with an AFM, to gather information on the recovery response of 10 or 1.7 μm thick sputter deposited films. First, the indenter was applied to the film surface at pressures of 8, 3, 1, and 0.5 mN. After which, the surface relief of the indent was scanned using the AFM, the sample then heated for 30 seconds to ~200°C using a heat gun, and the surface relief scanned again to gain insight of the NiTi film's recovery. Their research objective was not to report on the material properties, but on the degree of recovery of the indent's depth before and after transformations. They found that indents less than 100 nm deep were easily recoverable by heating. [19] On the other hand, Kumar and team used a Berkovich diamond indenter at room temperature and 250, 500, and 750 μN pressures with 5 seconds holding time. They were able to gather information on the film's hardness and elastic modulus values. Through their investigation they found that the heat treated films presented 150 GPa and 8.42 GPa elastic modulus and hardness values, while the same film in its amorphous state presented 138 GPa and 7.11 GPa values, respectively. They believed that

precipitation hardening during heat treatment may have contributed to the increased values and amorphous films property values resulted from its porosity and film softness. [9]

4.5 Electrical Resistivity and NiTi Thin Films

Methods used to study the phase transformation behavior of shape memory alloys include differential scanning calorimetry (DSC), internal friction measurements, magnetic susceptibility, thermoelectric power, and electrical resistivity. Of these electrical resistivity and DSC are the most common and are often used to complement the other or to confirm the results of the other testing method. Table 4.2 shows how comparable the transformation temperature data collected using resistivity and DSC testing methods. DSC requires the film's removal from the substrate for testing, and therefore, removing it from its natural state. On the other hand, resistivity tests are nondestructive, requires little material to test, and can be performed on samples as they are for MEMS device usage or application. For this work, electrical resistivity will be used to determine the transition temperatures of the NiTi thin films. [20]

Table 1. Comparison of transformation temperatures.

Tool	A'_s (°C)	A'_f (°C)	A_s (°C)	A_f (°C)	R_s (°C)	R_f (°C)	M_s (°C)	M_f (°C)
Four point probe	42	70	70	85	60	50	46	20
DSC	–	–	69	85	66	52	44	18

Table 4-2 Table showing how electrical resisitivity and DSC transformation temperature data collection is comparable. [20]

Resistance is an electrical material property used to describe the flow (or lack thereof) of electrons. It is defined as

$$R = V/I \qquad \text{Equation 4.7}$$

where R=resistance (Ohms), V=Voltage (Volts), I=Current (Amps). Whenever sample geometry is not a factor, resistivity (ρ) tests can be run using the four point probe method. In addition, it is also used to measure the bulk resistivity of starting wafers and the sheet resistance of shallow diffusion layers. General four point probe testing for thin films include a multimeter to measure voltage, a power supply to pass current, 4 probes, and a computer to record the information gathered. A current is applied to the two outer probes and the voltage between the two inner probes is measured. Figure 4.9 shows a schematic of the typical four point probe resistivity testing.

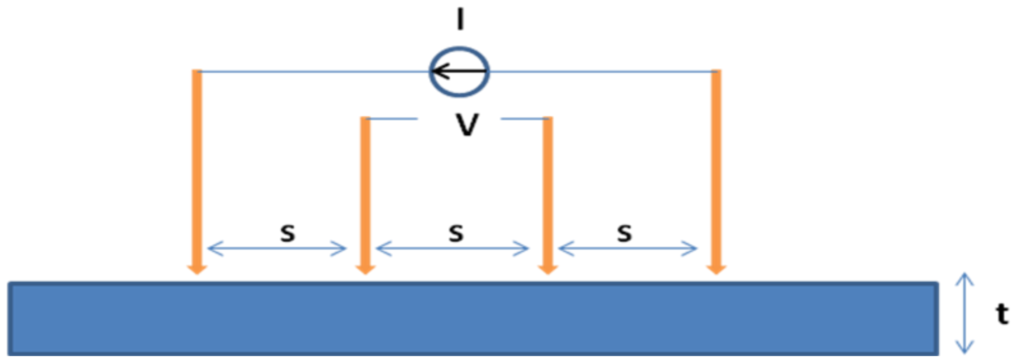

Figure 4-10 Schematic showing typical four point probe resistivity testing setup.

Two equations can be applied to calculate resistivity:

$$\rho= [2\pi sV] / I$$

Equation 4.8

for samples where the thickness (t) is much greater than the distance between the probes (s) or

$$\rho= [\pi\ t\ V] / [\ln 2*I]$$

Equation 4.9

for samples where the thickness is much less than the distance between the probes. [21]

There are a number of material characteristics that contribute to electrical resistivity—crystal structure, deformation defects, twin variant accommodations, and crystal distortions. For NiTi shape memory alloys resistance or resistivity investigations, the start and finish of the different phases is evident through the temperature vs. resistance/resistivity graphs. Generally, as the temperature increases, the resistivity value increases. Once the phase transformation occurs, the resistivity value changes—goes to a small maximum—and the resistivity returns to the linear state after the transformation is complete. The shape of the graph can distinguish between the present phases. It is believed that when the resistivity values do not increase linearly, a mixture of phases is present within the sample. The more thermal cycles the sample experiences, the greater the resistivity peak increases which make it easier to determine the Ms and Mf temperatures. Literature reports that a complete thermal cycle is between -120°C to 60°C because both austenite and martensite transitions are allowed to occur. [20,22]

Although resistance or resistivity measurements are simple testing methods, the results will vary dramatically according to the specimen's composition and thermal history. Mohanchandra et al reported that resistivity tests performed on films that have undergone heat treatment, an increase in annealing temperature results in a decrease in transformation temperatures. Since an increase in annealing temperature leads to a growth of precipitates which is manifested as a decrease in transformation temperature. The shape of the electrical resistivity graph and the occurrence of transition are very

dependent upon the composition and the heat treatment. The plots below, in Figure 4.10, show how much the data can change based upon simple heat treatment variations. [20,22]

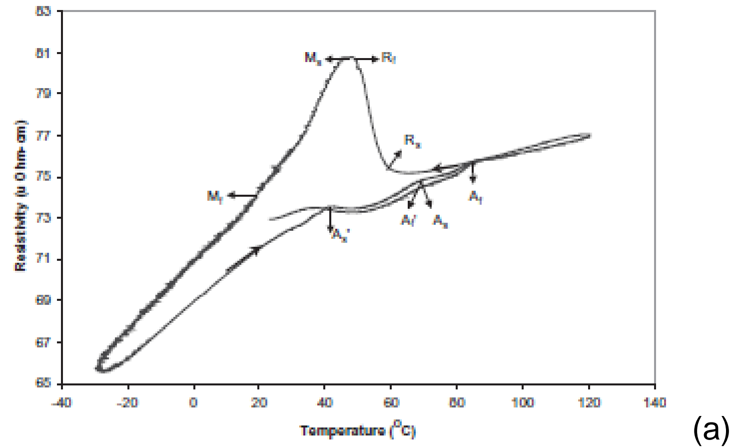

(a)

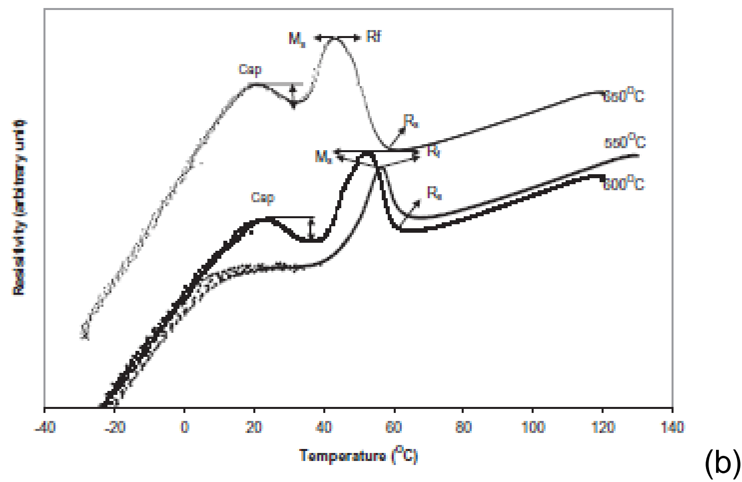

(b)

Figure 4-11 Example of graphs showing NiTi thin film resistivity testing results presented in literature. [20]

4.6 References

[1] E. Wibowo, C.Y. Kwok. 'Fabrication and characterization of sputtered NiTi shape memory thin films.' *Journal of Micromechanics and Microengineering*. 16 (2006) 101-108.

[2] Q. He, W.M. Huang, M.H. Hong, M.J. Wu, Y.Q. Fu, T.C. Chong, F Chellet, H.J. Du. 'Characterization of sputtering deposited NiTi shape memory thin films using a temperature controllable atomic force microscope.' *Smart Materials and Structures.* 13 (2004) 977-982.

[3] Y Fu, W Huang, H Du, X Huang, J Tan, X Gao. 'Characterization of TiNi shape-memory alloy thin films for MEMS applications.' *Surface and Coatings Technology.* 145 (2001) 107-112.

[4] "X-Ray Crystallography." http://en.wikipedia.org/wiki/X-ray_Crystallography. Last modified 01-23-2010. (Last accessed 01-26-2010)

[5] BD Cullity, SR Stock. *Elements of X-ray Diffraction.* 3rd ed. Prentice Hall. Upper Saddle River. 2001. Pp. 91-95, 101-103, and 182.

[6] A. Ohta, S. Bhansali, I. Kishimoto, A. Umeda. 'Novel fabrication technique of TiNi shape memory alloy film using separate Ti and Ni targets.' *Sensors and Actuators.* 86 (2000) 165-170.

[7] JJ Gill, K Ho, GP Carman. 'Three-Dimensional thin film shape memory alloy microactuator with two-way effect,' *Journal of Microelectromechanical Systems.* 11 (2002) 68-77.

[8] CL Shih, B-K Lai, H Kahn, SM Phillips, AH Heuer. 'A robust co-sputtering fabrication process for TiNi shape memory alloys for MEMS.' *IEEE Journal of Microelectromechanical Systems.* 10 (2001) 69-79.

[9] A Kumar, D Singh, D Kaur. 'Grain size effect on structural, electrical, and mechanical properties of NiTi thin films deposited by magnetron co-sputtering.' *Surface and Coatings Technology.* 203 (2009) 1596-1603

[10] D.C. Joy. 'Scanning electron microscopy for materials characterization.' *Current Opinion in Solid State and Materials Science.* 2 (1997) 465-468.

[11] JJ Gill, DT Chang, LA Momoda. GP Carman. 'Manufacturing issues of thin film NiTi microwrapper.' *Sensors and Actuators A.* 93 (2001) 148-156.

[12] J. I. Goldstein, D. E. Newbury, P. Echlin, D.C. Joy, C. Fiori, E. Lifshin. *Scanning Electron Microscopy and X-ray Microanalysis.* Plenum Press. New York. 1981.

[13] P. Surbled, C. Clerc, B. Le Pioufle, M. Ataka, H. Fujita. 'Effect of the composition and thermal annealing on the transformation temperatures of sputtered TiNi shape memory alloy thin films.' *Thin Solid Films.* 401 (2001) 52-59.

[14] S. Sanjabi, S.K. Sadrnezhaad, K.A. Yates, Z.H. Barber. 'Growth and characterization of TixNi1-x shape memory thin films using simultaneous sputter deposition from separate elemental targets.' *Thin Solid Films.*491 (2005) 190-196.

[15] 'How to select the correct indenter tip: Support note.' Agilent Technologies. 10-12-2009. http://cp.literature.agilent.com/litweb/pdf/5990-4907EN.pdf Accessed 02-05-2010.

[16] BC Prorok, Y Zhu, HD Espinosa, Z. Guo, Z.P. Bazant, Y. Zhao, B.I. Yakobson. 'Micro-and Nanomechanics.' *Encyclopedia of Nanoscience and Nanotechnology.* 5 (2004) 555-600.

[17] TestWorks 4 Software for Nanoindentation Systems Manual. MTS. 2002.

http://me.kaist.ac.kr/~fracture/stchoi/Research3.files/image003.gif. Accessed 02-05-2010.

[18] A.E. Giannakopoulos, S.Suresh. 'Determination of elastoplastic properties by instrumented sharp indentation.' *Scripta Materialia.* 40 (1999) 1191-1198.

[19] GA Shaw, DS Stone, AD Johnson, AB Ellis, WC Crone. 'Shape memory effect in nanoindentation of nickel-titanium thin films.' *Applied Physics Letters.* 83 (2003) 257-259.

[20] KP Mohanchandra, KK Ho, GP Carman. 'Electrical characterization of NiTi film on Silicon Substrate.' *Journal of Intelligent Material Systems and Structures.* 15 (2004) 387-392.

[21] R. C. Jaeger. *Introduction to Microelectronic Fabrication,* 2nd ed. Prentice Hall. 2002. Pp. 81-90

[22] H. Funakubo. *Shape Memory Alloys.* Gordon & Breach Science Publishers. New York. 1987.

Chapter 5 Experimental Procedure

5.1 NiTi Thin Film Production for Deposition Parameter Determination

To produce samples for characterization, a 300 nm thick silicon nitride (Si_3N_4) layer was grown onto both sides of a silicon (100) wafer using low pressure chemical vapor deposition (LPCVD) by Virginia Semiconductor, Inc. Table 5.1 presents the parameters for the LPCVD silicon nitride wafers. Following wafer purchase, it is necessary to perform a B clean on the wafers which is used to remove traces of organics and ions from the surface. The B cleaning solution is made with a 5:1:1 ratio of de-ionized (DI) water (H_20), ammonium hydroxide (NaOH), and hydrogen peroxide (H_2O_2). The B cleaning solution was heated to at least 70°C on a hot plate. Once the set temperature was reached, the beaker was removed from the hot plate and the wafers inserted into the B cleaning solution for 10 minutes. After 10 minutes, the wafers were removed, rinsed in DI water, and dried using a N_2 gun. DI water is highly purified and filtered meaning it is free of ions, particulates, and bacterial contamination.

Material	Silicon- CZ
Diameter	100 mm
Dopant	Any
Orientation	<100>
Resistivity	0-100 Ω*cm
Thickness	450-500 μm
Flats	2 SEMI
TTV	SEMI
Bow and Warp	SEMI
Grade	DSP
Polish	Both
Additional parameters	3000 Å Low Stress LPCVD

Table 5-1 List of the parameters used for silicon wafers.

Following the B clean, a titanium (Ti) adhesion layer was deposited on top of the Si_3N_4 layer. A 99.995% Ti target with 3 inch diameter and 0.25 inch thick dimensions, purchased from Kurt J Lesker Company, was used to deposit a 30 nm layer of Ti. Without the adhesion layer, the NiTi layer would be more likely to

delaminate during subsequent processing and characterization. Table 5.2 presents the sputtering parameters used to produce the 30 nm titanium layer.

Target	Titanium (DC)
Deposition Power (Watts)	200
Deposition Time (Minutes)	2
Deposition Temperature (°C)	23
Base Pressure (Torr)	5×10^{-6}
Deposition Pressure (mTorr)	8.0-8.3
Gas Flow Rate (sccm)	40
Holder Rotation	50%
Ignition Pressure (mTorr)	80

Table 5-2 Titanium adhesion layer sputter deposition parameters.

After a review of commonly used processing parameters found in literature, a number of parameters were chosen and placed within a design of experiment array. For the design of experiment, Stat Ease's Design Ease Software (version 7) was used to develop the run order and their subsequent parameters. The Ti power during deposition was set to either 10 W or 25 W; the substrate temperature during deposition was set to 23 ° C, 230°C, or 400°C; and the deposition pressures was set at 2.8, 5.0, or 8.2 mTorr. Table 5.3 presents the 16 sample array and their respective sample numbers.

SAMPLE	Ti POWER (Watts)	ARGON PRESSURE (mTorr)	SUBSTRATE TEMPERATURE (°C)	HEAT TREATMENT (°C/min)
15-09A	25	5.1	25	600/30
15-09B	25	8.2	25	600/30
15-09C	10	5.1	25	600/30
15-09D	10	8.2	25	600/30
15-09E	10	2.8	25	600/30
15-09F	25	2.8	25	600/30
15-09G	25	2.8	230	420/15
15-09H	10	2.8	230	420/15
15-09I	25	5.1	230	420/15
15-09J	25	8.2	230	420/15
15-09K	10	5.1	230	420/15
15-09L	10	8.2	400	none
15-09M	25	8.2	400	none
15-09N	25	2.8	400	none
15-09O	10	5.1	400	none
15-09P	25	5.1	400	none
15-09Q	10	8.2	230	420/15
15-09R	10	2.8	400	none

Table 5-3 Design of experiment array developed for NiTi thin film production.

The 1 μm thick NiTi samples were deposited using a co-sputtering process featuring a 99.995% equiatomic NiTi target produced by Kurt J Lesker and the Ti target previously mentioned. A co-sputtering process is required because nickel sputters at a faster rate than titanium and without the use of this process it would be more difficult to produce equiatomic NiTi thin films. Table 5.4 describes the deposition parameters. After deposition, the film thickness was measured using a mechanical surface profiler where the stylus is mechanically scanned over the wafer's surface. The profiler is able to measure films 0.01-5 μm thick. The heat treatment schedule used was a function of the substrate temperature used during deposition. Samples were annealed inside an alumina holder using the Brew furnace and furnace cooled. After cooling, the films were characterized using the methods presented in the proceeding section.

Target	Nickel Titanium (RF)	Titanium (DC)
Deposition Power (Watts)	400	15
Deposition Time (Minutes)	90	
Deposition Temperature (°C)	23 230 400	
Base Pressure (Torr)	5×10^{-6}	
Deposition Pressure (mTorr)	2.8 5.0 8.2	
Gas Flow Rate	12 25 40	
Holder Rotation	50 %	
Ignition Pressure (mTorr)	50 mTorr	
Thickness (µm)	1	

Table 5-4 NiTi thin film co-sputtering parameters.

5.2 NiTi Thin Film Characterization Techniques

The most common characterization methods for NiTi thin film samples mentioned in literature include x-ray diffraction, atomic force microscopy, electron dispersive x-ray spectroscopy, tensile testing, nanoindentation, differential scanning calorimetry, bulge testing, electrical resistance, scanning electron

microscopy, and transmission electron microscopy. Due to the film thickness and delicacy of the samples produced during this work, many of the techniques mentioned above are not compatible. However, the methods which were compatible for thin films are defined below.

5.2.1 Phase Identification of Deposited Films

Crystallinity was determined using x-ray diffraction (XRD) analysis. XRD scans of the deposited films were obtained using a Rigaku DMAX-III X-ray diffractometer at room temperature. The Cu-Kα tube was used at 40 kV and 40 mA and the scans were performed from 2θ=20° to 80° range, 0.05° scan interval, and a 5° per minute scan speed.

5.2.2 NiTi Thin Film Microstructural Observation

A JEOL JSM-7000F field emission scanning electron microscopy was used to gain insight on the surface characteristics of the deposited thin films. The films were adhered to the holder's surface using a strip of carbon tape and observed at different magnifications especially, 23000X and 65000 X magnifications. SEM film surface observations occurred before and after heat treatment, as well as before and after MDE sample release.

5.2.3 NiTi Thin Film Composition Determination

Energy Dispersive Spectroscopy (EDS) analysis, incorporated into the SEM, was used to determine the composition of the deposited films. Spirit V107 software was used to gather the data collected from the EDS detector. To ensure

sufficient statistics were obtained, the detected x-rays were counted for at least 3000 counts before analyzed. Several areas on the wafer sections were scanned to get an average film composition. EDS was performed before and after heat treatments. Only Ni and Ti elements were analyzed. All other elements present were recorded for reference purposes only.

5.2.4 NiTi Thin Film Electrical Resistivity Testing

A special Teflon holder was designed to hold the thin film during the resistivity testing. Figure 5.3 shows the side and top views of the holder. Each of the probes on the holder was paired with an Agilent Technologies data acquisition/switch unit (DAU) Model 34970A, its subsequent multichannel analyzer, and operated using its four-wire ohm measurement configuration. All experiments took place within an ESPEC Criterion ECT-3 temperature chamber with a Watlow F4 controller cycling thorough temperatures between -30°C to 120°C with cooling/heating rates of 2°C per minute or 5°C per minute. Figure 5.4 shows the experimental setup. During the tests, the DAU monitored the film and chamber temperatures, the resultant resistance, and recorded them every one second using BenchLink Data Logger software. T-type thermocouples were used to monitor the film and chamber's temperatures.

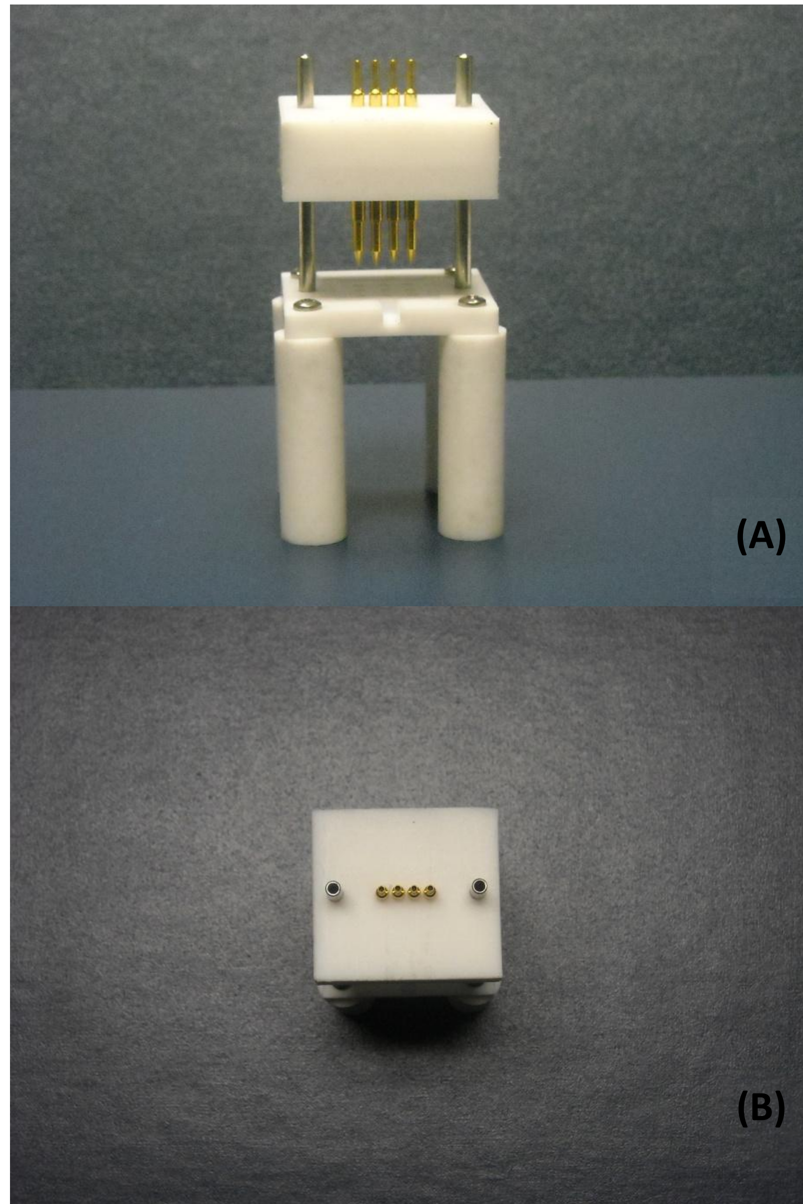

Figure 5-1 Photograph of Teflon holder for SMA thin film resistivity testing. (A) Side view. (B) Top view.

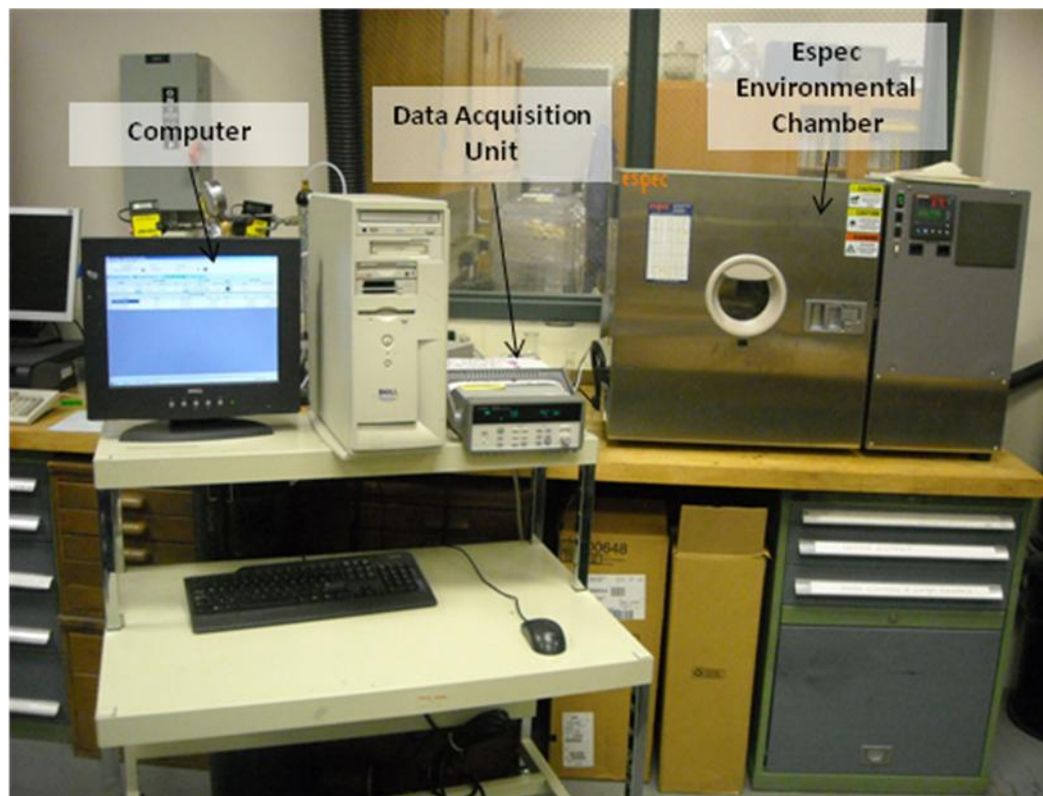

Figure 5-2 Photograph of electrical resistivity testing set-up.

Chapter 6 Results and Discussion

As outlined in Chapter 5, sixteen samples were produced with various sputter deposition and annealing parameters to determine which films met and exhibited shape memory effect requirements. Each of these film samples was characterized through Scanning Electron Microscopy (SEM), X-ray diffraction (XRD), and Energy Dispersive Spectroscopy (EDS) to determine which films exhibited SMA properties. Samples which did not meet the necessary requirements for SME confirmation were omitted. The remaining films were then tested for shape memory confirmation using resistivity and for mechanical property data using nanoindentation and membrane deflection experimentation. The results from this study will be discussed in the remaining portion of this chapter.

6.1 NiTi Thin Films and Crystallography

The sixteen samples outlined in Table 5-3 were exposed to x-ray diffraction to determine if the deposition and annealing parameters produced crystalline films and to disclose the phases present. From the scans, it was found that SMA films deposited at room temperature exhibit amorphous XRD scan qualities where a single broad peak between 2θ=40° to 45° is seen. However,

films deposited at room temperature followed by annealing or deposited at temperature produce crystalline films where numerous peaks are seen in this same area. Figure 6-1 shows an example of how the XRD scans change from amorphous to crystalline following annealing.

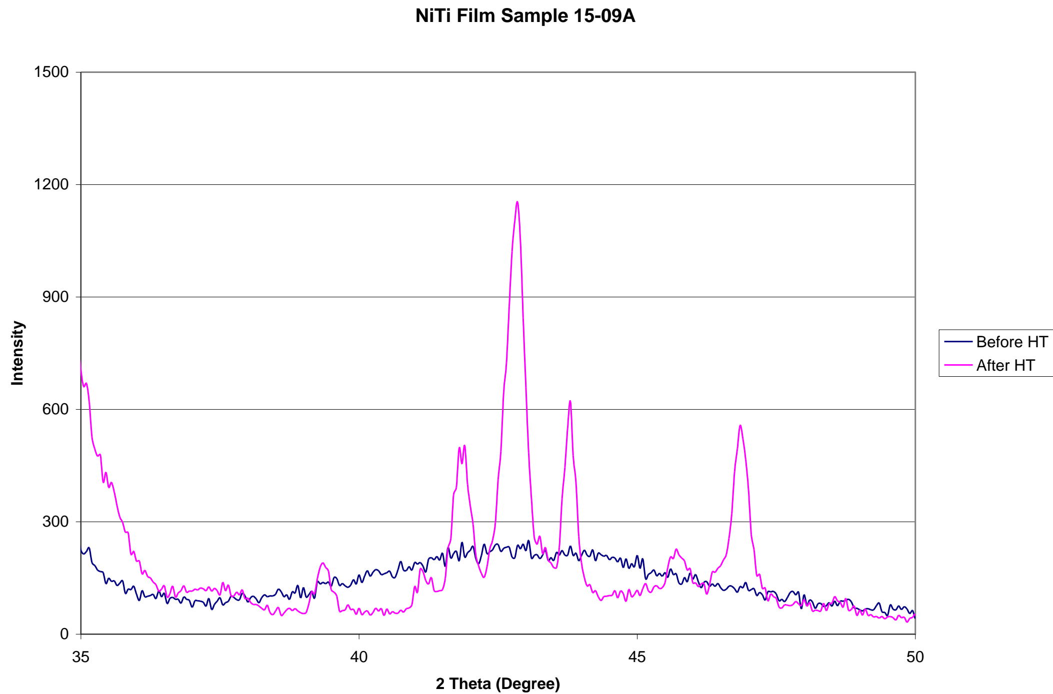

Figure 6-1 Example XRD scan showing the transformation of NiTi film from amorphous to crystalline.

Film samples that underwent annealing were scanned before and after their heat treatment. The results from the XRD scans for each sample can be seen in the Table 6-1.

Sample	Phase(s) Seen
15-09A	M(-111) M(020) A(110)
15-09B	M(020)
15-09C	M(012)
15-09D	Amorphous
15-09E	Amorphous
15-09F	M(002) M(020) M(-112) A(110)
15-09G	Amorphous
15-09H	M(020) A(110)
15-09I	M(020) A(110) A(200)
15-09J	M(020)
15-09K	M(020) A(110)
15-09L	A(110)
15-09M	A(110) A(200)
15-09N	A(110) A(200)
15-09O	A(110) A(200)
15-09P	A(110) A(200)
15-09Q	M(020)
15-09R	A(110)

Table 6-1 XRD scan results for samples produced in DOE array.

From the scans, it can be seen that after annealing samples 15-09D, 15-09E, and 15-09G still show amorphous film structures. Samples 15-09B, 15-09C, 15-09G, and 15-09J show only the martensite phase and 15-09L, 15-09M, 15-09N, 15-09O, 15-09P, and 15-09R show only the austenite phase. Samples 15-09A, 15-09F, 15-09H, 15-09I, and 15-09K show both the martensite and austenite phases. Films deposited at temperature always showed crystallinity. In many cases, austenite and martensite phases are present within the sputter deposited films. The presence or absence of these phases is often a reflection of the film's composition. For example, XRD scans for nickel-rich films only show the austenite phase.

6.2 NiTi Thin Film Surface Observations

The sputter deposited and heat treated film surfaces were observed using a JOEL scanning electron microscopy. Figures 6-2, 6-3, and 6-4 show the surfaces of the films grouped together according to their annealing schedule. It was found that films deposited at room temperature and heat treated showed cracked surfaces and can be seen in Figure 6-2. Cracked film surfaces will be ineffective when paired with microelectronic fabrication techniques and actuation principles and are therefore eliminated.

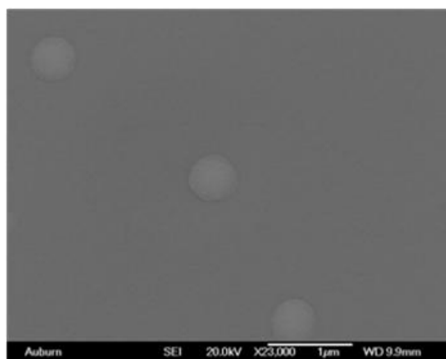

15-09A

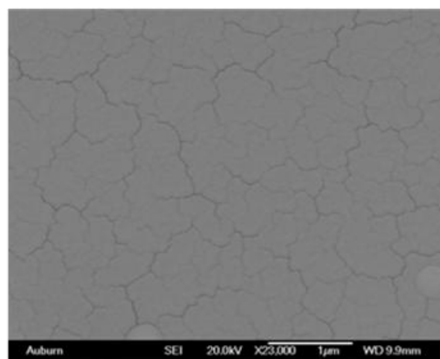

15-09B

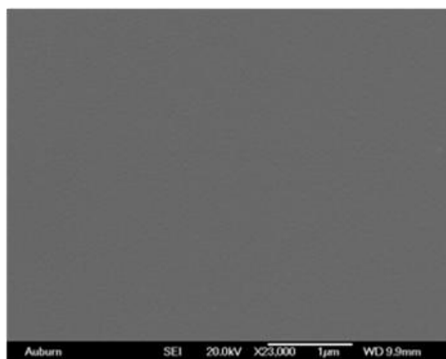

15-09C

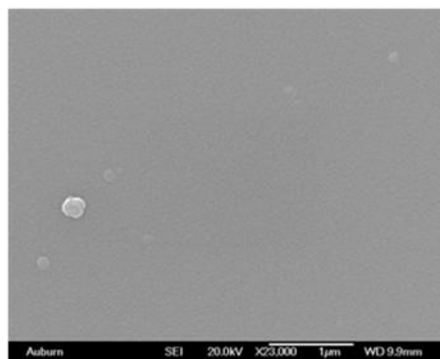

15-09D

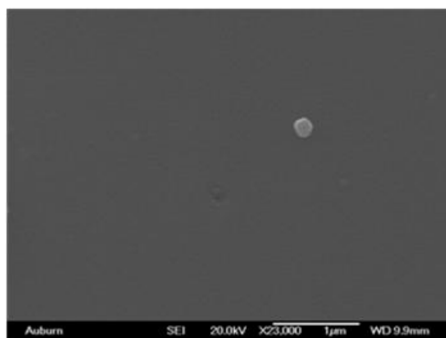

15-09E

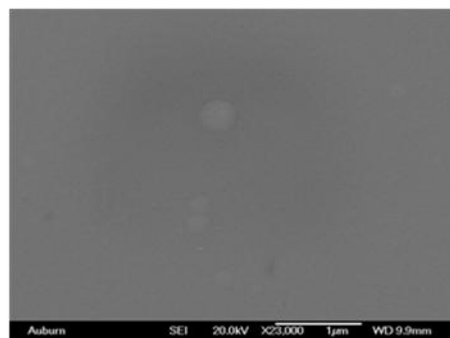

15-09F

Figure 6-2 SEM micrographs of films deposited at 25°C and annealed at 600°C for 30 minutes.

Films deposited at 230°C and exposed to a 420°C and 15 minute anneal produced films that were smooth and featureless. They also showed scattered areas of sputtered film globs which appear as areas of incomplete film crystallization or areas where abnormal growth spurts occurred during sputter deposition. These film micrographs can be seen below in Figure 6-3. It was initially assumed that the globs were a product of precipitates, but their composition mirrors that of the smooth areas of their respective films. The globs are sites of film growth. Thus far, the globs have been only a function of this substrate temperature deposition. Although the films are crystalline, the deposition at temperature makes the process incompatible for microfabrication processing.

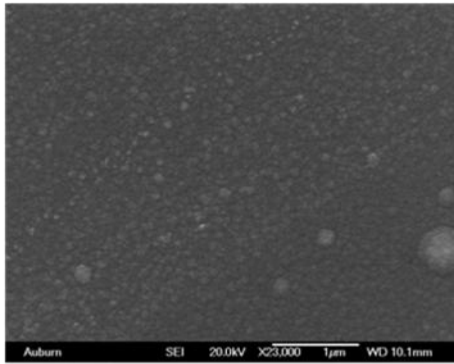

15-09G

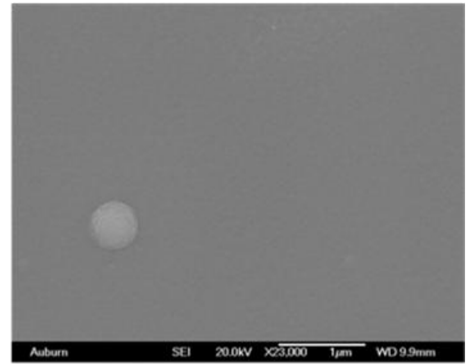

15-09H

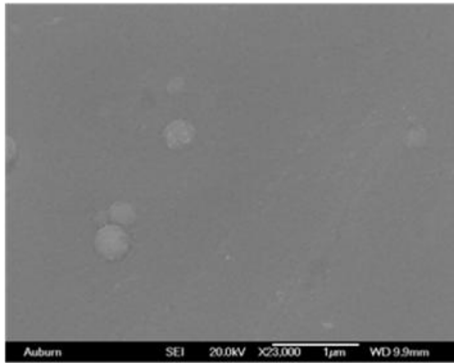

15-09I

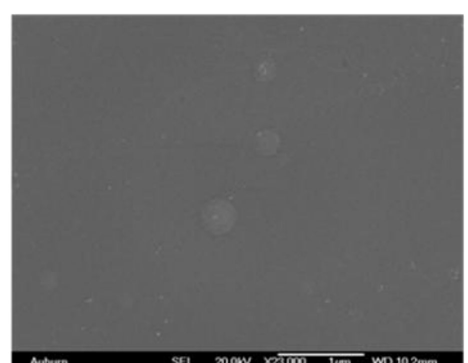

15-09J

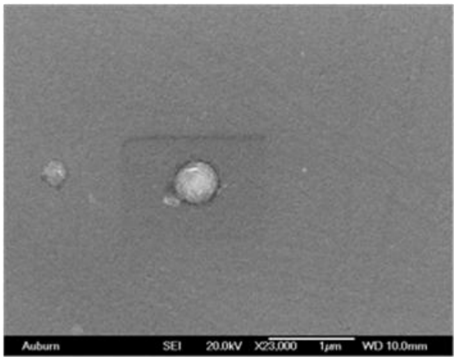

15-09K

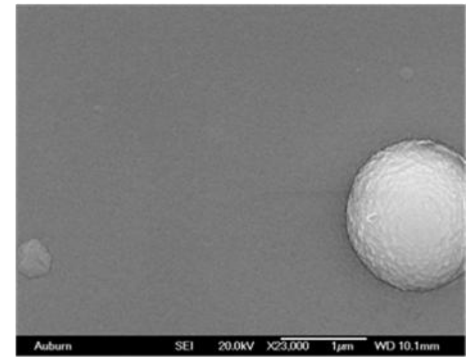

15-09Q

Figure 6-3 SEM micrographs of films deposited at 230°C and annealed at 420°C for 15 minutes.

Films deposited with a substrate temperature of 400°C and no annealing produced films whose features were dependent upon the Titanium power used. For example, samples deposited with 10 W Titanium power exhibited square-like features—15-09L, 15-09O, and 15-09R. On the other hand, films deposited at temperature and 25 W Ti power exhibited chip-like features—15-09M, 15-09N, and 15-09P. Figure 6-4 shows the micrographs of these films.

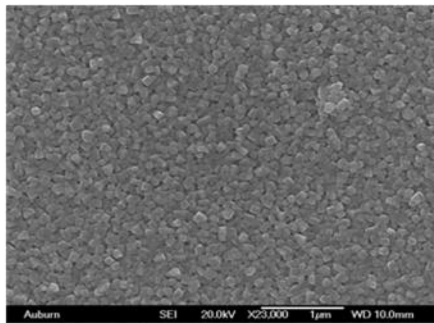

15-09L

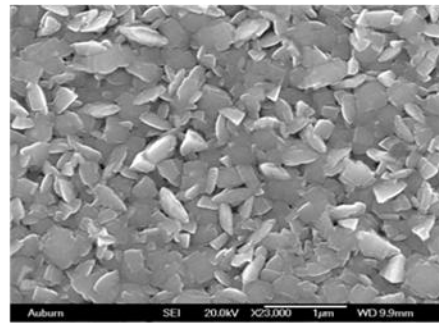

15-09M

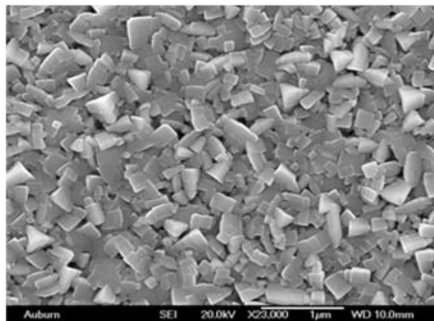

15-09N

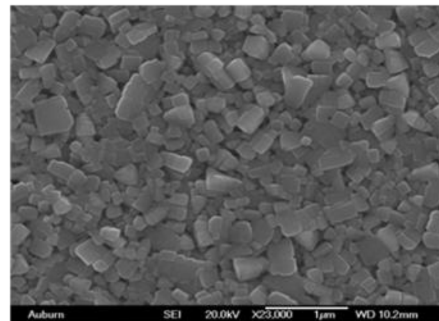

15-09O

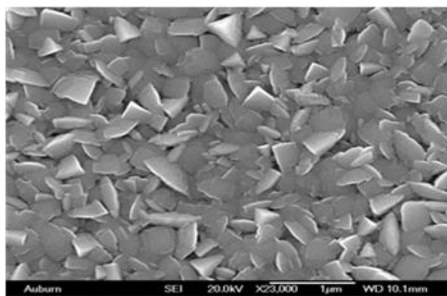

15-09P

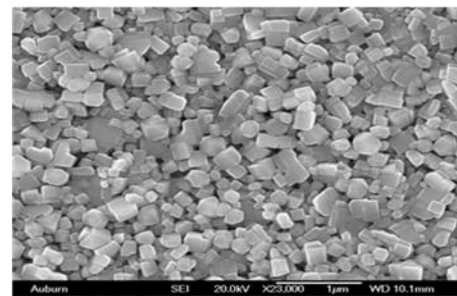

15-09R

Figure 6-4 SEM micrographs of films deposited at 400°C and no anneal.

6.3 NiTi Thin Film and Composition

Film composition is by far one of the most important parameters; since a 1 atomic percent change in NiTi composition can result in a 100°C transformation temperature shift. [19] The varying sputtering parameters used during this study were used to produce films with nickel compositions ranging from 41 atomic percent to 60 atomic percent. The table below provides a listing of the nickel values of the prepared samples before and after heat treatment. All annealed films showed an increase in nickel content following heat treatment. The increase in nickel content could be the result of the nickel atoms diffusing to the surface of the film following heat treatment.

The films that showed composition closest to equiatomic composition (with a ±1.5 atomic percent) were 15-09B, 15-09M, 15-09N, and 15-09R. Each of the equiatomic films were deposited at temperature except 15-09B and at argon gas pressures of either 2.8 or 8.2 mTorr.

SAMPLE	TI POWER (Watts)	AR PRES. (mTorr)	SUBSTRATE TEMP. (deg C)	NICKEL CONTENT (At. %) BEFORE HT	HEAT TREATMENT (deg C/min)	NICKEL CONTENT (At. %) AFTER HT
15-09A	25	5.1	25	47.92	600/30	52.70
15-09B	25	8.2	25	43.78	600/30	49.58
15-09C	10	5.1	25	41.77	600/30	55.13
15-09D	10	8.2	25	41.73	600/30	51.63
15-09E	10	2.8	25	46.33	600/30	60.41
15-09F	25	2.8	25	51.01	600/30	55.08
15-09G	25	2.8	230	47.35	420/15	44.99
15-09H	10	2.8	230	50.52	420/15	61.34
15-09I	25	5.1	230	44.89	420/15	58.91
15-09J2	25	8.2	230	3.94	420/15	53.67
15-09K	10	5.1	230	51.81	420/15	59.66
15-09L	10	8.2	400	56.03	none	56.03
15-09M	25	8.2	400	50.50	none	50.50
15-09N	25	2.8	400	49.98	none	49.98
15-09O	10	5.1	400	53.20	none	53.20
15-09P	25	5.1	400	52.13	none	52.13
15-09Q	10	8.2	230	50.96	420/15	59.75
15-09R	10	2.8	400	51.25	none	51.25

Table 6-2 Presentation of the NiTi film compositions before and after annealing.

6.4 NiTi Film Sample Production Elimination

Scans for near equiatomic and titanium-rich films show the martensite phase. Since films 15-09C, 15-09D, and 15-09E possessed amorphous film structures following annealing, they will be omitted from further consideration of SME confirmation. It was seen that the amorphous films were deposited using 10 W Titanium power and an unheated substrate deposition. No other correlation could be found between the processing parameters and the resultant phases present within the films.

Films deposited at 8.1 mTorr produce films with a cracked surface despite the NiTi/Ti power used. From the results it is evident that the deposition pressures greater than or equal to 8.1 mTorr is too great.

Recall that Sample 15-09B produced a cracked surface and was subsequently eliminated. In addition, the other viable samples were produced at temperature and not suitable for microfabrication processing. However, their composition does help determine the samples parameters suitable for additional testing—15-09M and 15-09N.

6.5 Additional NiTi Thin Film Sample Production

After the most promising sputtering parameters were outlined, it was necessary to use those parameters to produce additional samples for transformation temperature and mechanical data investigations. The first set of samples produced were Sample 20-21 featuring a NiTi target powers of 275 W, 300 W, 350 W, or 400 W and Ti target power of 25 W, and deposition time of

10550 seconds. Table 6-3 shows specific parameters for each sample. Samples 20-21-B, 20-21-E, 20-21-G, and 20-21-H produced films with cracked surfaces. The deposition pressure of 8.1 mTorr was also omitted because its usage continually produced films with cracked surfaces. Cracked surfaces indicate that the pressure within the chamber is so high that the sputtered atoms have too much velocity and force transferred to them during deposition resulting in the introduction of too much stress on the film's surface. After annealing, none of the remaining films' composition values were equiatomic. Therefore, all of Sample 20-21 samples were useless and new deposition parameters were investigated.

Sample	NiTi Power (W)	Substrate Temperature (°C)	Ar Pressure (mTorr)	XRD Phases (After HT)	Ni at. % before HT	Ni at. % after HT
20-21-A	300	25	2.8	A (110)	46.73	46.41
20-21-B	275	25	8.1	A (110) M(-111)	44.68	44.50
20-21-C	400	25	2.8	A (110) M(020) M(012)	47.34	47.59
20-21-D	275	25	2.8	A (110) M(020)	46.15	45.98
20-21-E	300	25	8.1	M(002) M(-111) A(110) M(020) M(012)	45.24	45.31
20-21-G	350	25	8.1	A (110)	45.38	45.49
20-21-H	400	25	8.1	A (110)	46.11	46.02

Table 6-3 Outline of the sputtering parameters for Sample 20-21.

Since the current deposition parameters did not produce the film compositions required, it was mandatory that new parameters be outlined. After several trials and errors, the new and suitable sputtering parameters featured NiTi target power of 400 W and Ti target power of 15 W. Samples 20-45, 20-64, 20-101, and 25-1 were all produced using these new parameters. Table 6-4 outlines their individual sputter deposition parameters. It is important to note,

that samples sputtered at 5.0 mTorr began to delaminate during processing, especially after heat treatment. Therefore, this deposition pressure was also eliminated from future sample production. Optimal sputter deposition parameters consist of NiTi target power of 400 W, Ti target power of 15 W, and deposition pressure of 2.8 mTorr.

Sample	NiTi Power/ Ti Power (W)	Subst. Temp. (°C)	Ar P (mTorr)	Film Thickness (μm)	XRD Phase (After HT)	Ni at. % (Before HT)	Ni at. % (After HT)
20-45-A	400/15	25	2.8	1.000	A(110) M(020)	51.08	49.39
20-45-B	400/15	25	5.2	1.000	A(110)	51.93	47.80
20-64-C	400/15	400	2.8	1.000	A(110) M(012)	49.95	n/a
20-64-D	400/15	400	5.0	1.000	A(110) M(012)	48.30	n/a
20-101-A	400/15	25	2.8	1.666	A(110) M(020)	n/a	51.53
20-101-B	400/15	25	5.0	1.666	A(110)	n/a	49.69
25-1-A	400/15	25	2.8	1.051	A(110) M(020)	n/a	50.15
25-1-B	400/15	25	2.8	2.038	A(110) M(020)	n/a	48.34

Table 6-4 Presentation of sputtering parameters for Samples 20-45, 20-64, 20-101, and 25-1.

6.6 NiTi Thin Film and Transformation Temperature

Research teams often present data on the DSC curves of the NiTi films to gather information on the transformation temperatures of the deposited films, as well as confirm the shape memory effect. Traditionally DSC investigations are performed using powder samples because more surface area is available thereby yielding a greater signal. In addition, powder samples allow even heating and cooling of the sample. For those reasons, when thin film samples are used, the signal is weak, yields inaccurate data, and in the case of device fabrication requires the sample destruction. A Flexinol SMA wire was used to obtain a standard reference. However, during DSC sample preparation, the aluminum crucible and the preparation puncher were drastically deformed because the wire is much harder than the crucible puncher or sealer and the test was not performed.

As an alternative, electrical resistivity test procedures were performed to obtain transformation temperatures for the sputter deposited SMA thin films. The resistivity tests were performed under the premise that it is a nondestructive evaluation technique where the sample temperature is increased and decreased in cycles resulting in a change in crystal structure. To determine the transformation temperature in which the film transforms and to confirm the proper operation of the in-house set-up, an environmental chamber, power supply, multimeter, computer, and Pomona clips were outfitted to a commercial NiTi wire. Figures 6-5 and 6-6 illustrate the testing setup. An Agilent 34401A 6½ digital multimeter was used to measure voltage and an Agilent DC power supply (Model

3612A) was used to apply current and the distance between the Pomona clip pins touching the wire and film was 12.10 nm. Leads from the Pomona clip were attached to the NiTi wire in the following manner:

	Positive Lead	Negative Lead
Voltage	Red	Blue
Current	Green	white

Figure 6-5 Photograph of the interior of the environmental chamber and Pomona clip for resistivity testing.

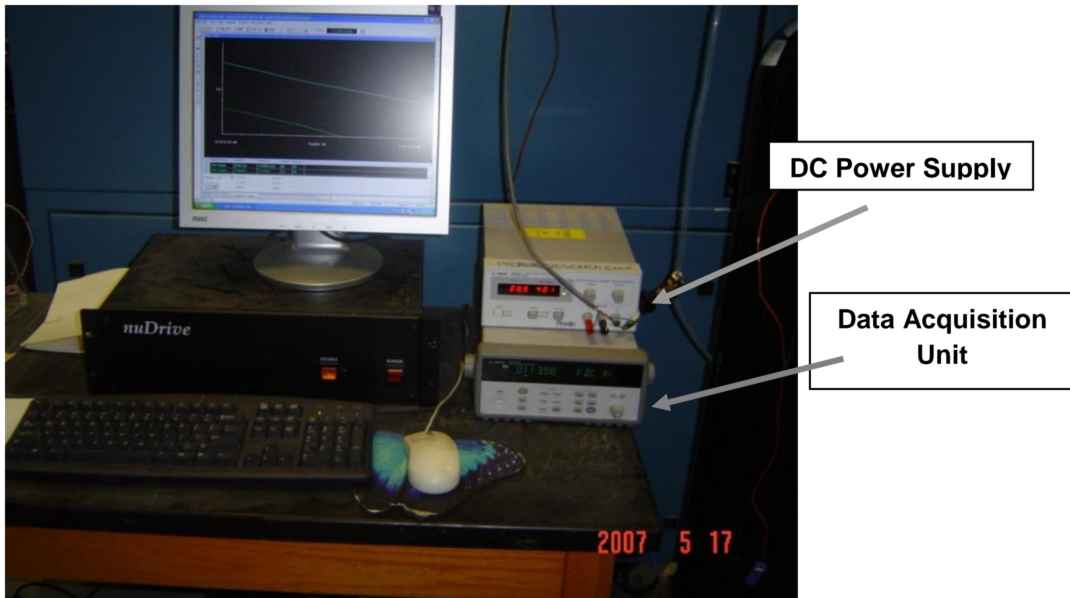

Figure 6-6 Photograph of the measurement setup of the resistivity testing setup.

Temperature cycle programs were developed and input into the environmental chamber unit where the temperature cycling went from -50°C to 150°C with a ramp rate of 10°C per minute. Initial characterization readings showed that the chamber and the current set-up worked fine, but an additional outlet was needed to monitor temperature change. For that reason, an Agilent 34970A Data Acquisition/Switch Unit (DAU) was incorporated into the set-up and the multimeter was eliminated. The DAU featured a 20 channel card, where the following parameters were set—Channel 1 was the positive current lead, Channel 2 was the negative current lead, and Channel 5 was the T-type thermocouple set to monitor temperature output. Using a DC power supply, a voltage of 0.8-0.9 V was applied which corresponded to a 400 mA current application and the temperature program was re-written to cycle between 20°C to

90°C. Due to the size of the chamber, Sample 15-09N, a sputter deposited film, was included in the resistivity analysis with the wire. The results from the simultaneous film and wire resistivity test runs can be seen in Figure 6.7.

Recall that resistivity, ρ, values across the temperature range were calculated using equation 6-1 where R, resistance values, were measured by the DAU, A is the wire's cross-sectional area, and L is its length:

$$\rho = R*(A/L) \qquad \text{Equation 6-1}$$

and $A/L = (d2\pi)/ (4L) = [(500x10^{-6}m)*2* \pi] / [4*(5x10^{-2}m)] = 3.93x10^{-6}$ m.

Resistance, is a relative value, computed using values reported under the four point probe testing configuration found within the DAU. Equation 6-2 outlines the definition of R.

$$V_{measured}/I_{applied} = R \qquad \text{Equation 6-2}$$

Therefore

$$\rho = R*(3.93x10-6) \qquad (\Omega*m) \qquad \text{Equation 6-3}$$

For the 1 µm thick films, the resistivity equation was modified to include the thickness of the films, t, and become

$$\rho = R * [(\pi*t)/ (\ln 2)] \qquad (\Omega*\mu m) \qquad \text{Equation 6-4}$$

For these films the equation becomes

$$\rho = R * (4.532) \qquad (\Omega*\mu m). \qquad \text{Equation 6-4}$$

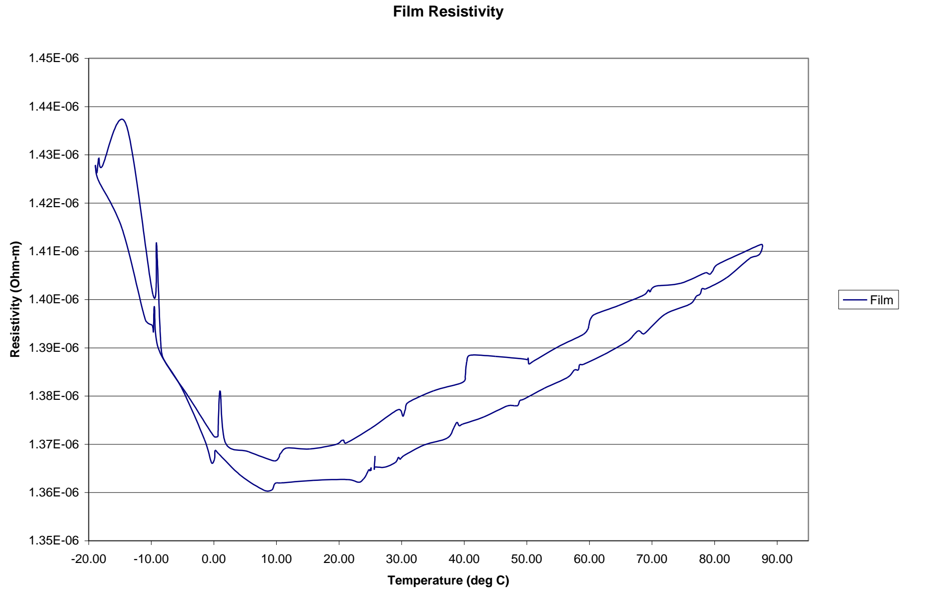

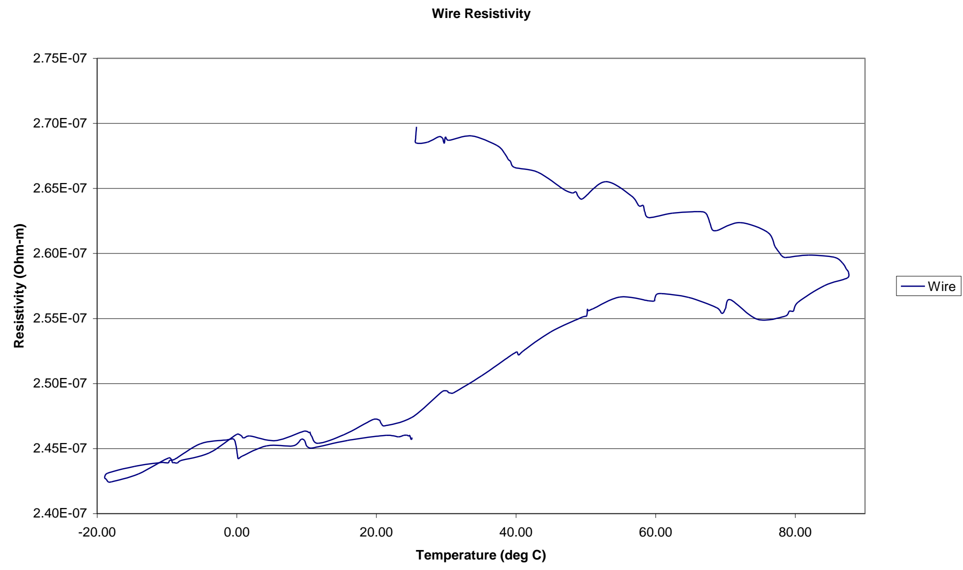

Figure 6-7 Resistivity plots for SMA wire and thin film sample 15-09N using the environmental chamber.

The jagged data set seen in Figure 6-7 is due to the holds inputted into the temperature cycle. The holds were placed into the cycling program to ensure that the samples' temperatures were regulated and steady during cycling. Therefore,

they must be eliminated in future cycles. The results from the 15-09N film resembled a semiconductor and the wire's data did not form a connecting hysteresis, although it was extremely close. In addition, the resistivity values are very small. Therefore, I decided to increase the amount of current applied. To determine a suitable current application, I repeated the tests on the 15-09N film using current values of: I=0.1 A, 0.5 A, and 1 A and a temperature cycle going from -20°C to 80°C with a 10°C per minute ramp rate. The results from this test cycle can be seen in figures 6-8, 6-9, and 6-10. The test performed with a current application of 0.1A, seen in Future 6-8, showed a decrease in resistivity as temperature increased. Once again, the semiconductor-like results were obtained which is the opposite of what should be occurring with SMA. The application of 0.5A test current results looked the most promising of the three, since the resistivity increased as the temperature increased and almost took on a hysteresis shape. The results can be seen in Figure 6-9. The investigation performed using a current application of 1A (see Figure 6-10) resulted in a plot saturated with noise. Although I am unsure of the actual cause of the noise, it could be that at the onset of this test, the film was "burned out" from repeated testing and unable to respond in a suitable manner. This is feasible since I ran the tests one consecutively without any rest time between the tests leading to excessive heat application. Since the resistivity data results from Figure 6-9 most closely illustrate the data we anticipate, current will be applied at 0.5 A during each run.

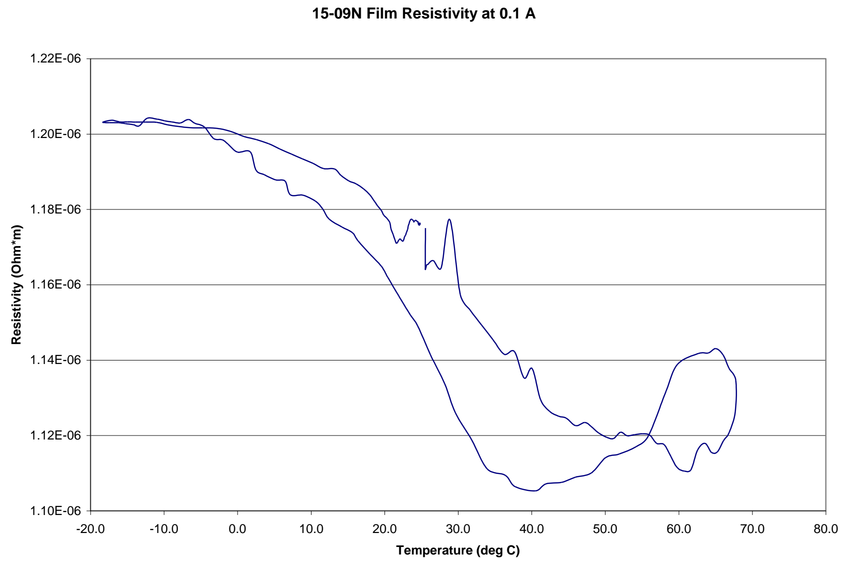

Figure 6-8 Resistivity testing results of Sample 15-09N performed using 0.1 A current application.

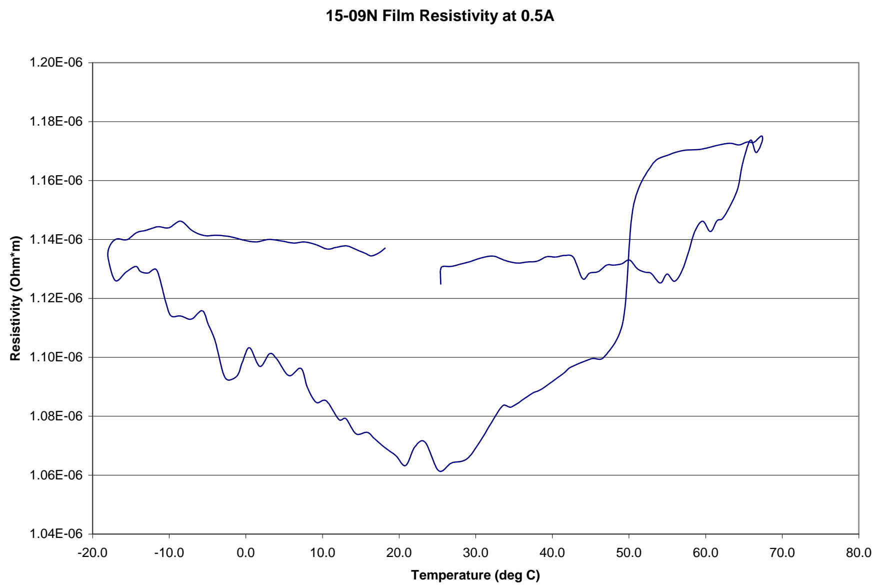

Figure 6-9 Resistivity testing results of Sample 15-09N performed using 0.5 A current application.

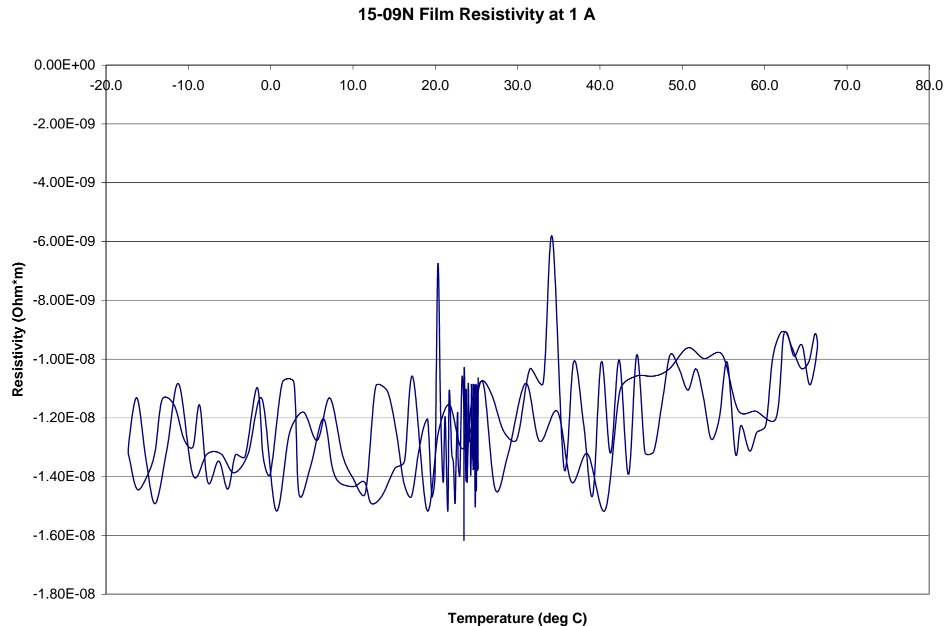

Figure 6-10 Resistivity testing results of Sample 15-09N performed using 1 A current application.

After re-examining this data and the testing arrangements, I determined that the current environmental chamber was too large for the size of samples being investigated and the temperature cycling rate (10°C/minute) made it difficult for the small samples to regulate and reach the desired temperature. For those reasons, I switched to a much smaller environmental chamber—ESPEC Criterion Chamber ECT-3 featuring a Watlow F4 Controller. Since the chamber is smaller, the fan used to change the temperature within the chamber is very intense and it applies a great deal of force during operation. Therefore, it was very important to ensure that the sample is stable and experiences no vibration during the temperature cycling .Otherwise, the unstable, vibrating sample will become a source of noise during testing producing invaluable results. The same data

collection arrangement from the larger environmental chamber was used to test the samples.

The continual exposure of a sample to excessive testing causes it to stop exhibiting its shape memory properties, it is recommended that the samples be periodically replaced. To ensure that valuable results were obtained, I replaced the previously used wire with one produced by Mondotronics called Flexinol. Flexinol wire is mostly used for small device building and was predetermined by its manufactures to have a transformation temperature between 50°C and 75°C. This wire would serve as an excellent reference, since it is already known to exhibit the SME. A one-inch long, 500 μm thick Flexinol wire sample for testing was cut, extended, and adhered across a thin ceramic plate to ensure that the wire did not vibrate during testing. The resistivity plot for the Flexinol wire seen in Figure 6-11 is similar to Sample 15-09N data presented in Figure 6-11. Although the resistivity range is higher than that previously seen, the chart does not produce a hysteresis. In addition, when the test was repeated, the same results were not seen even though the resistivity data were in the same range (see Figure 6-12).

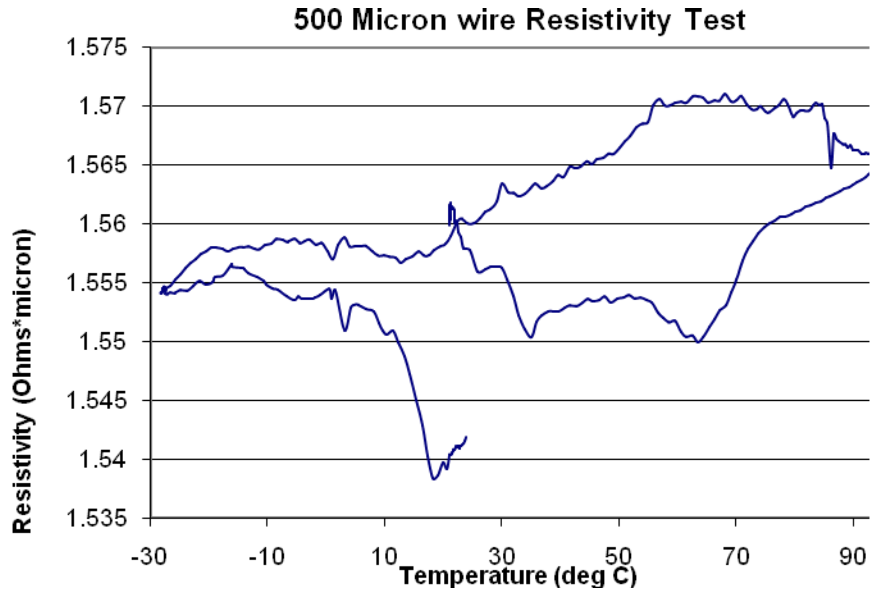

Figure 6-11 Resistivity plot for Flexinol wire.

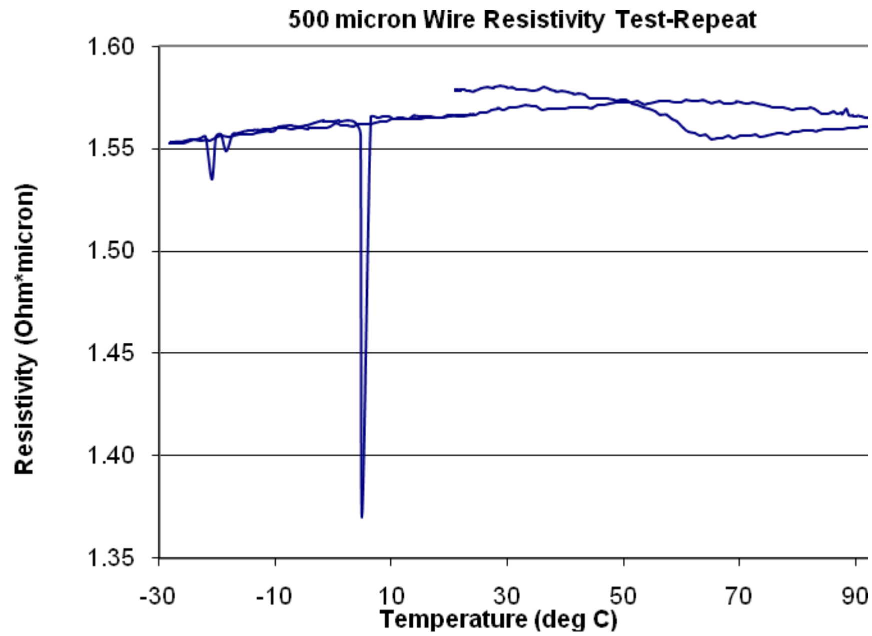

Figure 6-12 Resistivity plot for repeated Flexinol wire test.

I contributed the fairly linear and inconsistent results to vibration and altered the setup to further reduce vibration by using Kapton tape to secure the wire samples. Figure 6-13 provides an illustration of the new setup. I also increased the current application from 0.5 A to 1.0 A and 1.3 A.

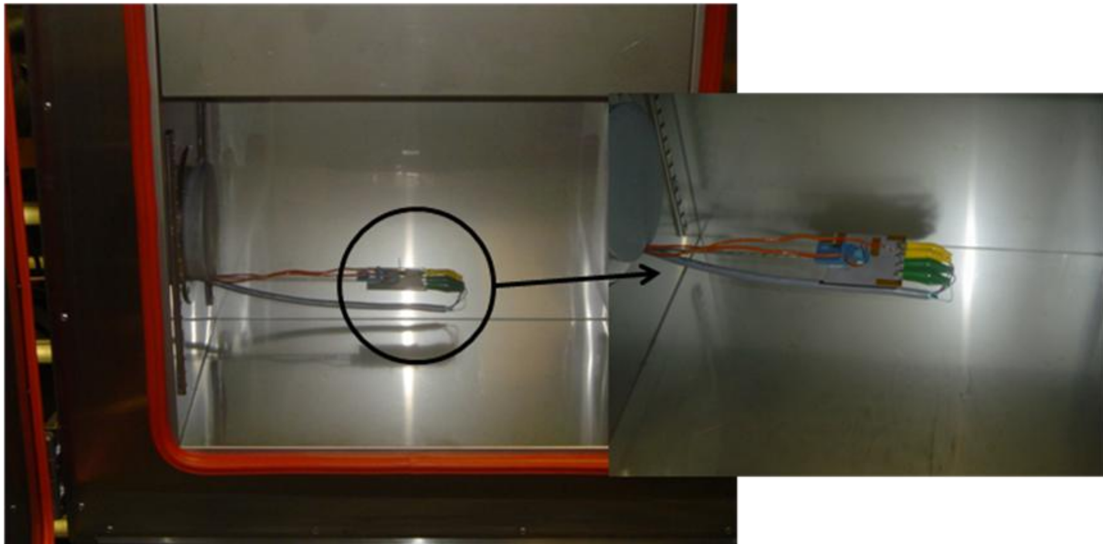

Figure 6-13 Image of the resistivity testing setup for the wire using Kapton tape.

Following the application of the current increase, the data presented an expected resistivity graph, but still showed signs of noisiness. After running additional tests and re-examining the testing setup, it was seen that the confinement of the wire to the ceramic plate was preventing the wire from transforming properly. By fixing the wire to the ceramic plate to prevent vibration and forcing the wire to lie in the flat state, the wire was being trained even as the temperature cycling continues. To counteract and prevent this training, the ceramic plate was removed from the setup and the free wire and the leads for the

DAU were adjoined using alligator clamps, separated by uniform distances. The future tests were repeated with a new wire since the previously used wire underwent training during previous testing. The next tests were performed with only two temperature cycles and a temperature ramp rate of 2°C per minute. The results, shown in Figure 6-14 A and B, from the new wire looks comparable to literature, but the transition periods occur during cool down instead of both cool down and heat up. As additional testing on the new wire continued, it was evident that the more temperature cycles the wire undergoes, the tighter the cycles' data becomes.

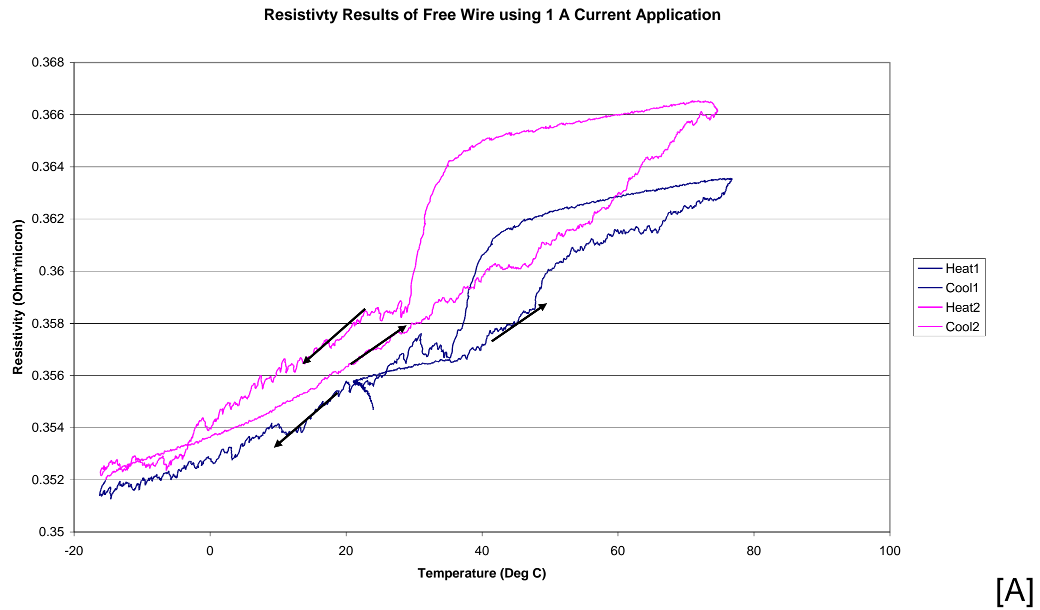

[A]

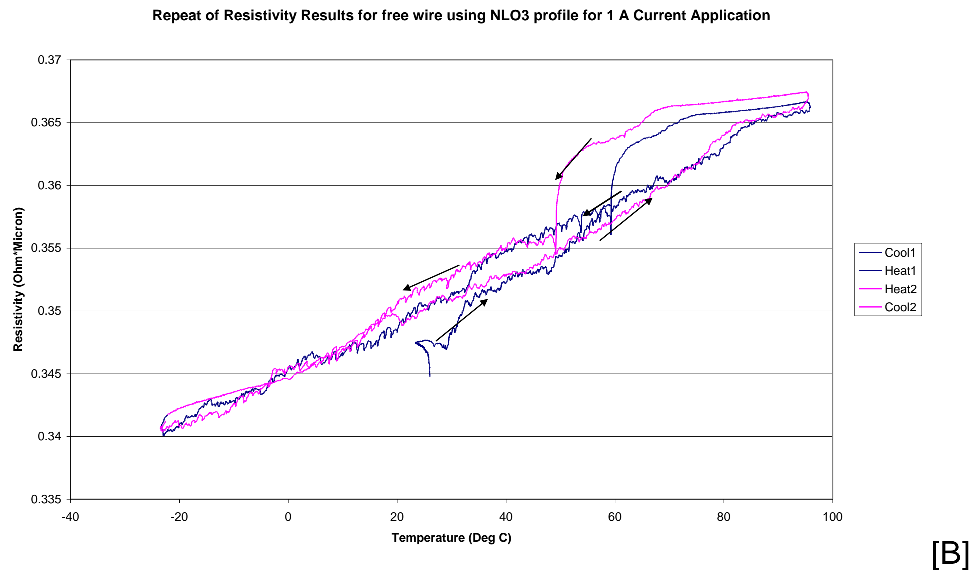

[B]

Figure 6-14 Resistivity plots of Flexinol wire using 1 A current application. [A] Plot from the initial two temperature cycle run. [B] Plot from additional testing.

In addition, the increase in test frequency resulted in greater displays of noise in the data. I consulted with Mr. LeVar Odum and Mr. LC Mathison about my entire

resistivity testing apparatus. it was brought to my attention that the power supply model being used was unable to accurately and constantly supply 1 A of current because it was better equipped to supply constant voltage. To achieve more accurate results, I decided to remove the power supply from the testing set-up and utilize the DAU's internal four-wire ohm configuration setup. The schematics and actual interpretation for this system are shown in Figure 6-15.

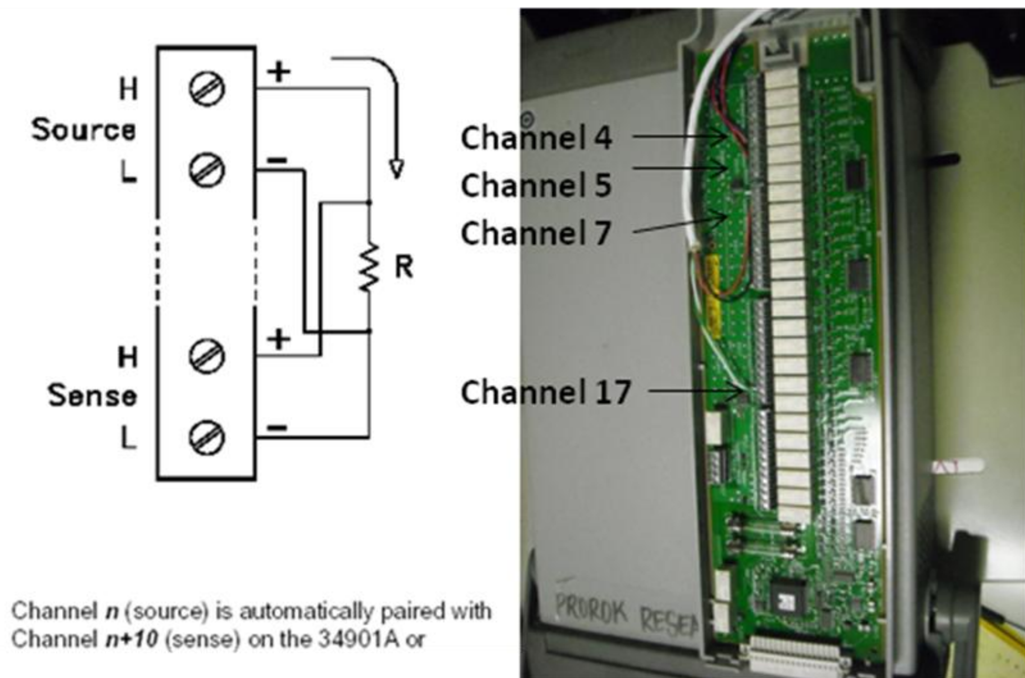

Figure 6-15 Schematic and photograph of 20-channel card used for 4-wire ohm configuration.

The new testing channels using the 20 channel card and 4-wire ohm configuration are channel 4 for wire temperature measurement, channel 5 for chamber temperature measurement, channel 7 (or n) for current (source) application, and channel 17 (or n+10) for voltage (sense) application. This

configuration also allows the alteration of the test current using the range settings programmed into the DAU. The new DAU configuration was tested using the same Flexinol wire from the previous tests and the results can be seen in Figure 6-16.

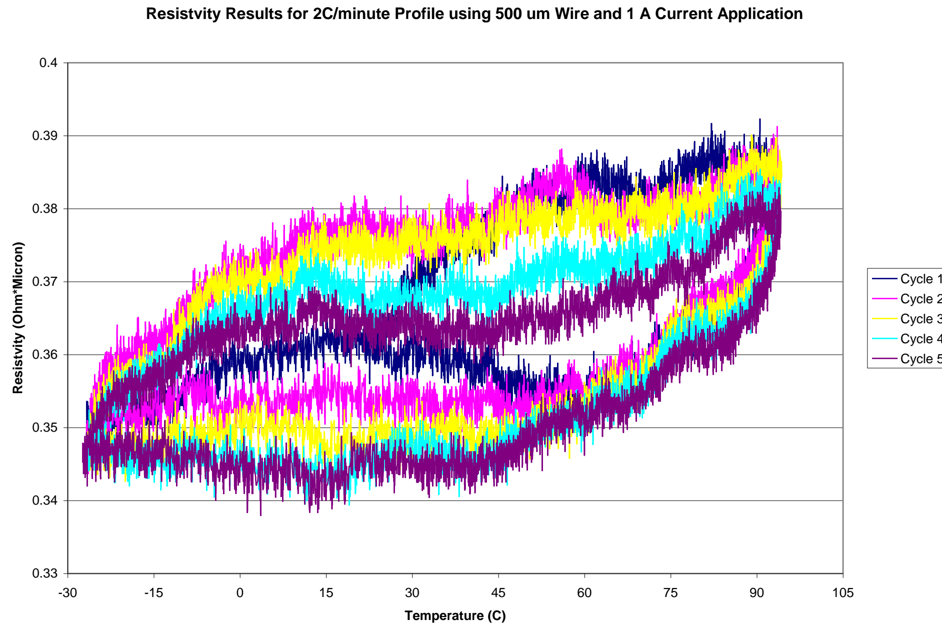

Figure 6-16 Resistivity plot of Flexinol wire sample after 4-wire ohm configuration was implemented.

After incorporating the four-wire ohm test set-up, the resistivity data, presented above, has a range similar to the tests presented in Figure 6-14, shows a hysteresis, and is repeatable. The presence of the hysteresis loop is desired since it proves the SME through repetition and transition temperature change. Although the results were successful, they are still noisy and I am unable to see

any definite periods of transition. Therefore, I changed the temperature profile to feature a shorter profile with multiple repeats. This change in temperature profile parameters, thereby reduced the number of cycle steps and provided a better, easier operation for the environmental chamber's controller.

After continued testing using the free wire clamping system and the new temperature profile parameters, I was able to determine clear areas of transition using the Flexinol wire. Figure 6-17 shows the resistivity profile for the Flexinol wire. An increase and/or decrease in the resistivity values or peaks can be seen between 5°C & 20°C and 45°C & 60°C. Notice that the curves become very tight or show little change in resistivity around or after temperature cycle 28. These peaks could be identifying marks of the transition temperature for the wire, especially since the specifications for the wire state the transformation temperature is between 55°C and 75°C.

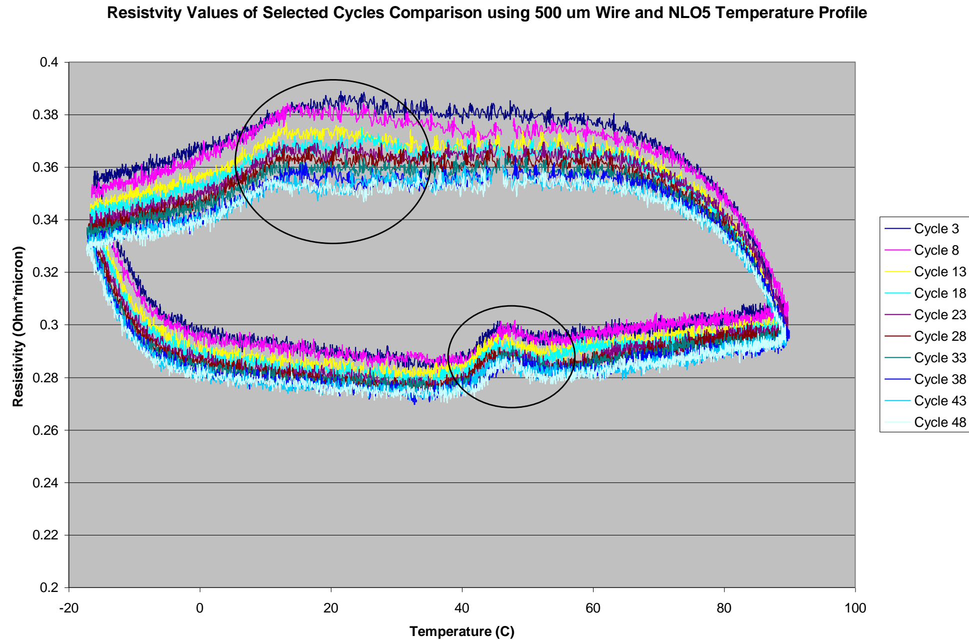

Figure 6-17 Resistivity plot for Flexinol wire after 48 temperature cycles.

Since the resistivity data collection using the commercial wire was successful, I began testing on sputter deposited films. Initial testing revealed very noisy results, so I decided to alter the testing current using two of the test ranges internally set by the DAU—0.1 kΩ and 1 kΩ. In addition, the ramp rates for this testing period were altered between 2°C per minute and 5°C per minute. Although additional samples were evaluated using these testing ranges, the results presented in Figures 6-18 A and B are representative of the samples tested. Of this data, the only data set with reasonable data is that with a 0.1 kΩ testing range and NLO5B temperature profile or 5°C per minute ramp rate. As illustrated in Figure 6-18, the data was linear, very noisy, accented with spikes seen at various temperatures, and inconsistent.

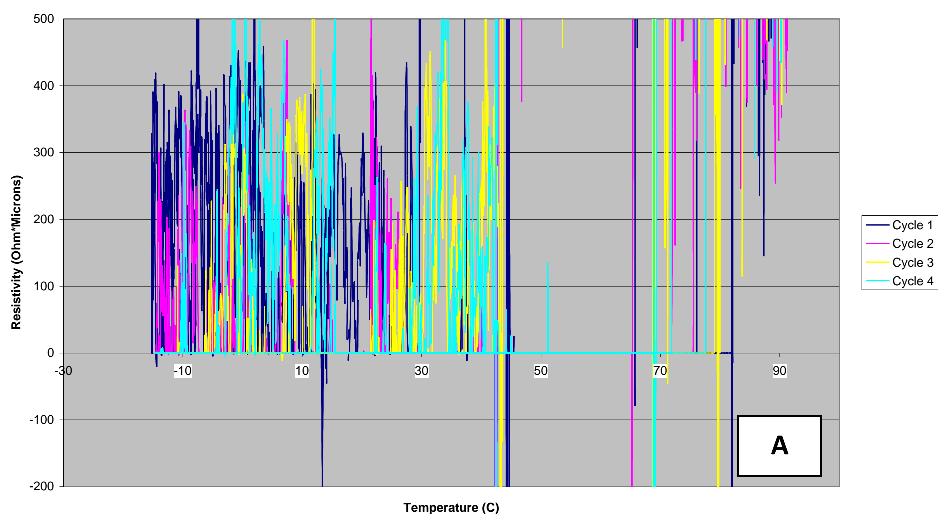

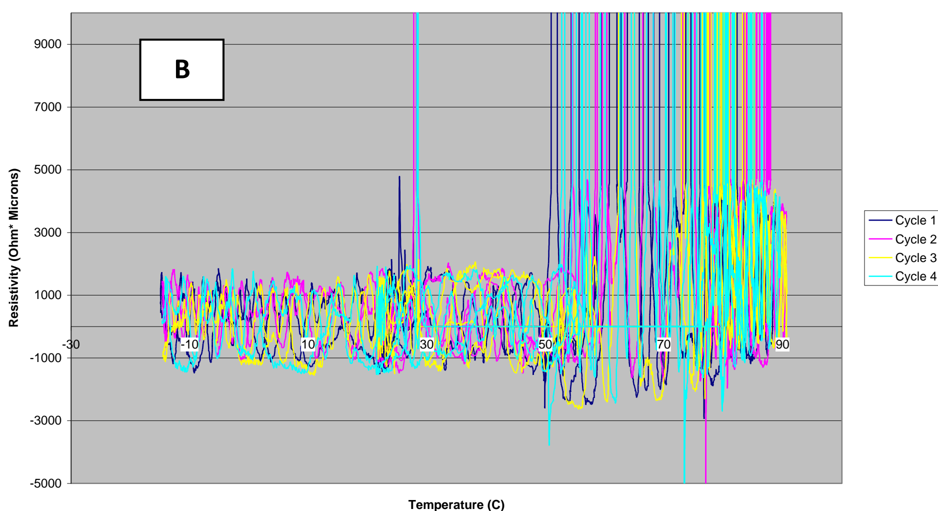

Figure 6-18 Resistivity plots for Sample 15-09M and 15-52N using different testing ranges. [A] Sample 15-52N using 0.1 KΩ testing range. [B] 15-52N using 1 KΩ testing range.

The extremely noisy data can be caused by two things—either sample vibration during temperature change or thermoelectric voltage changes during testing. Sample vibration has long since been taken care of; therefore it should not be an issue. Thermoelectric voltage changes result from the DAU and the sample being at different temperatures during testing, which in this case is very difficult to alter. It is also known that using different connection materials can also lead to flawed resistivity results. Obtaining such noisy data prompted me to investigate the probe's electrodes. After dissecting the Pomona clip, it was seen that the inner portion of the electrodes are not all gold as expected. Figure 6-19 shows micrographs of the Pomona clip leads. In fact, they are gold plated only on the visible ends of the leads. This could definitely affect the electrode connection and influence noise introduction during temperature cycling. Therefore, I needed to design a new testing apparatus to remove the Pomona leads or adjust them be more compatible with our system.

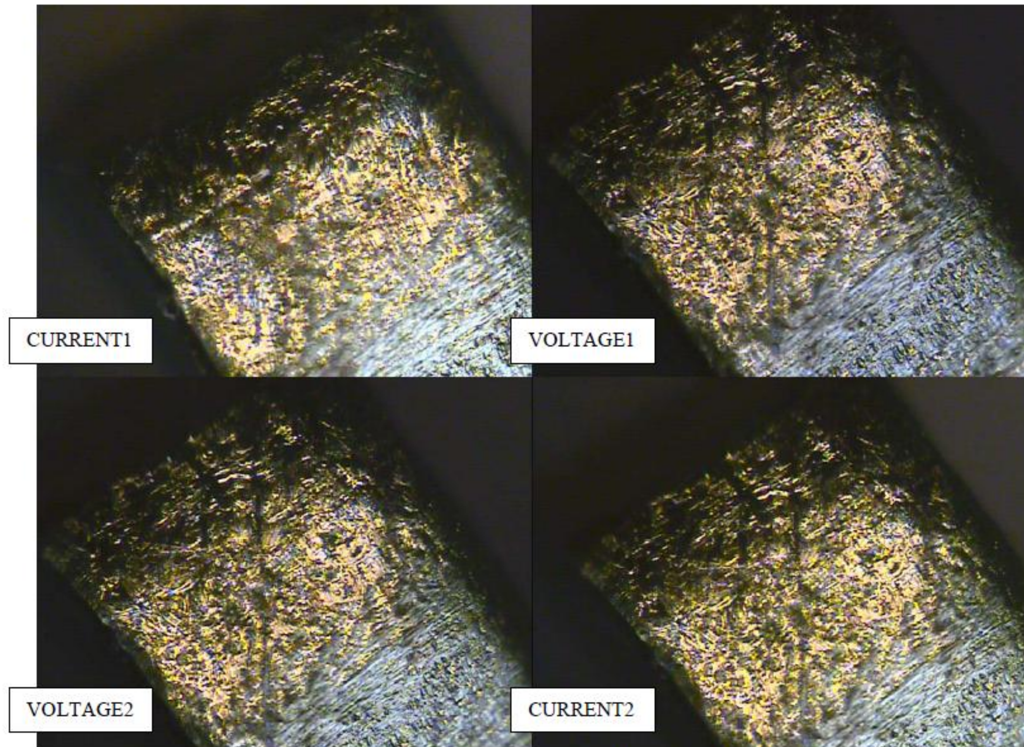

Figure 6-19 Micrographs of Pomona clip leads.

The testing configuration was altered using a gifted Teflon holder previously used to perform resistivity testing on other samples. The holder was cleaned with methanol using swabs, dried overnight inside a desiccator, and outfitted for testing using new electrodes and pins. To test the holder and its compatibility with the setup, Sample 15-127 was tested at 100 μA testing range and 5°C per minute temperature cycle. The resulting resistivity data was linear, noisy, and still did not show any hysteresis. Since this sample did not work as expected, I obtained commercially available NiTi thin film samples from Johnson-Matthey. The Johnson-Matthey film was 50.8 μm thick. Tests were performed on

the Johnson Matthey film using the Teflon holder, but the data was still very noisy. Even after increasing the testing range, the data was still noisy with higher resistivity ranges. A silver paste was applied to the commercial film to enhance the conductivity between the film and the pins. Once the silver contacts were cured, a static temperature test was performed on both samples, with and without the silver paste. The tests were performed in the 100 Ω testing range. The data from the test can be seen in Figure 6.20. The inclusion of the silver caused the data to become cleaner, consistent, and more stable. In addition, the resistivity data range was reduced. The samples with the silver paste were then exposed to the full temperature cycle which produced additional clean data with transformation occurring during the heat up process and not during cool down.

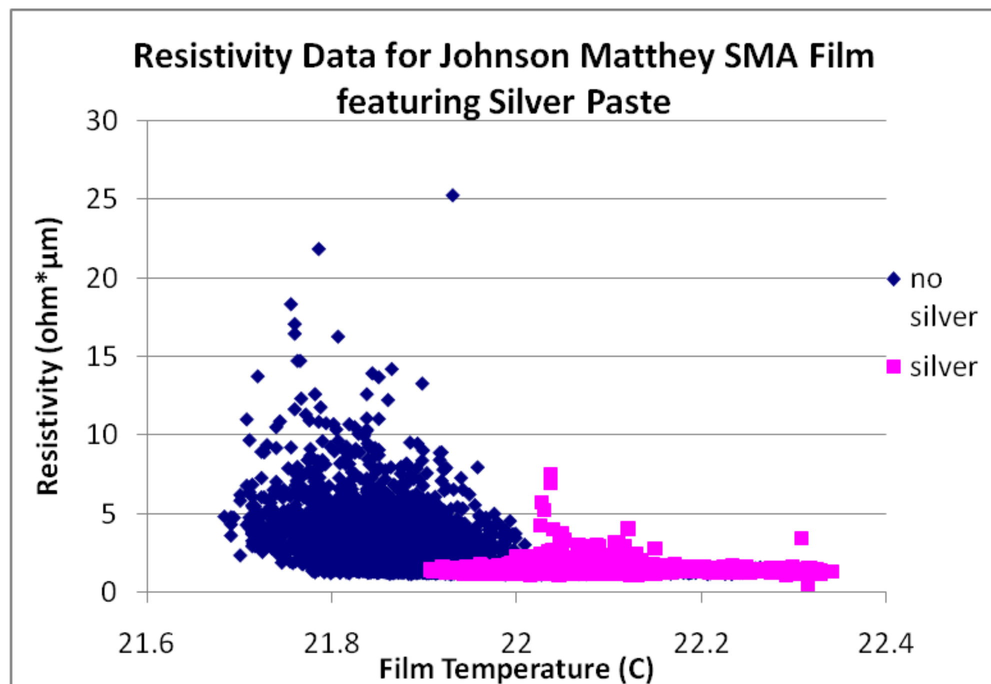

Figure 6-20 Resistivity plot for the Johnson Matthey commercial sample with and without the addition of the silver paste.

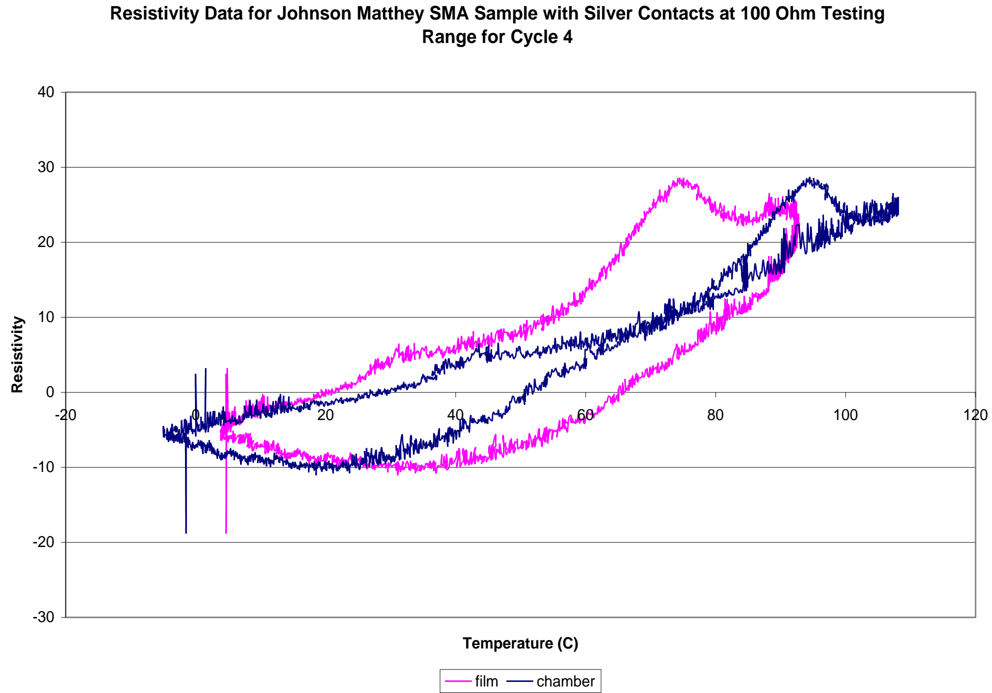

Figure 6-21 Resistivity test results for Johnson Matthey film sample featuring silver paste contacts.

Although this data seen in Figure 6-21 was promising, the results are not very repeatable. After re-examining the testing setup, it was determined that the currently used Teflon holder was too thick for the extremely thin samples being tested, did not provide any ventilation for the sample during testing, and the wires connecting the probes to the DAU were made of differing materials. To resolve these problems, a new Teflon holder was constructed featuring holes in the holder's base to allow ventilation and new probes and wires purchased. After several version changes, the holder seen in Figure 6-22 was used for testing.

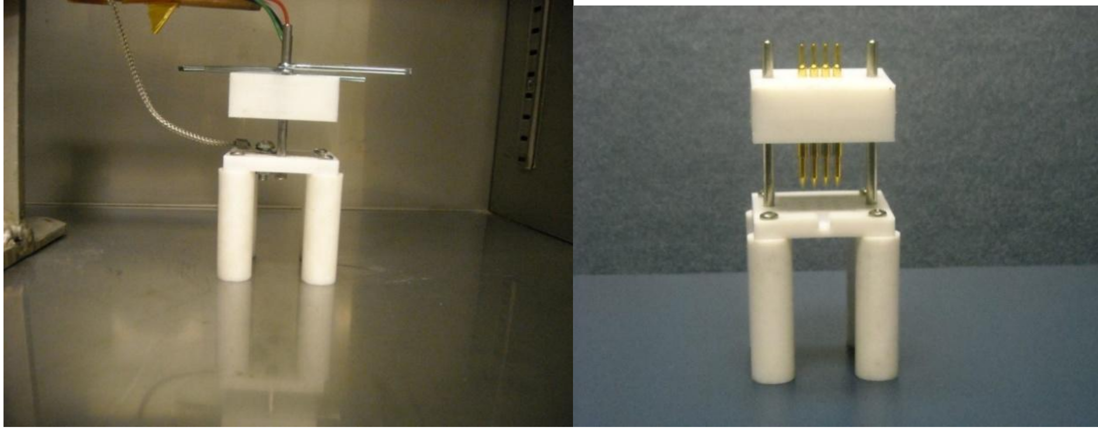

Figure 6-22 Photographs of the newly constructed Teflon resistivity holder.

The first sample tested using this new holder was an untested Johnson Matthey film with silver contacts. During temperature cycling with the new holder, the top of the holder would move up during temperature cycling, creating a non-existent connection and the production of noisy data results. To prevent the top of the holder from moving during temperature changes, the top of the holder was secured in position using cotter pins. In addition, the testing range was set to automatic. An automatic testing range allows the DAU to adjust the current application according to the needs of the sample under testing and eliminates the need for extensive trial and error resistivity testing. These minor changes produced data that was much cleaner and a hysteresis was seen. Figure 6-23 provides the resistivity plot developed after continuous testing of the Johnson Matthey SMA film. Notice that there are three areas of transition—between 30-50°C during heat up, 9-19°C and 42-62°C during cool down. These are

acceptable transformation periods, especially the 30-50°C range since this film has been designed to transform at the body's temperature—approximately 32°C.

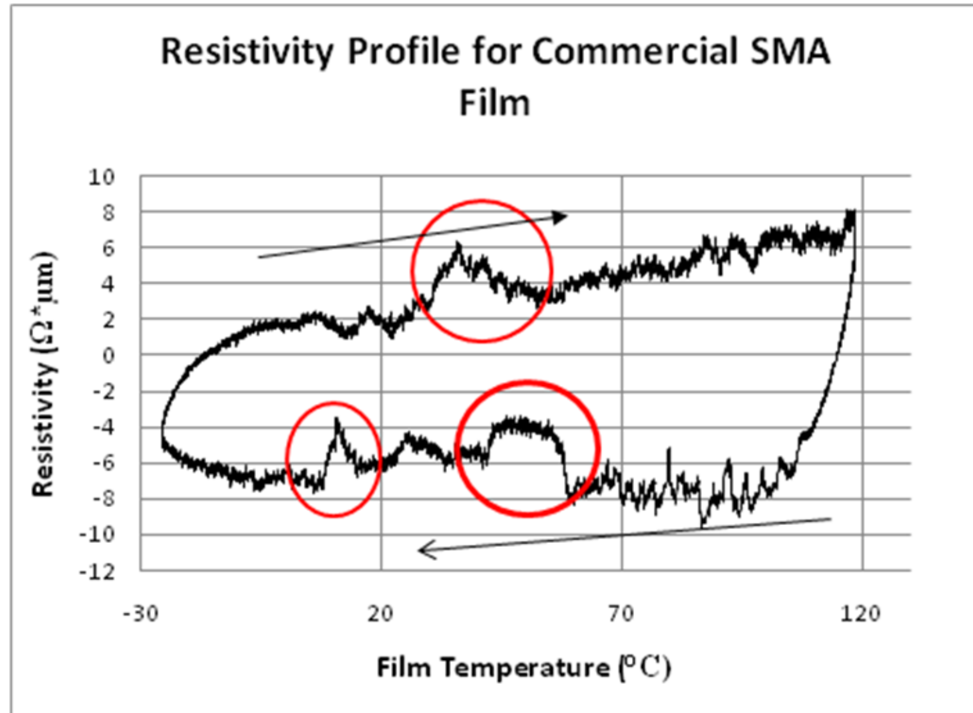

Figure 6-23 Resistivity plot of the Johnson Matthey commercial film with silver contacts.

Since the data collected from the Johnson Matthey commercial SMA film presented valuable results, Sample 20-21-C, a sputter deposited film, was placed into the holder and tested. The results are shown in Figure 6-24. The data collected during this run showed three areas of transition—between 30°C to 35°C and 60°C to 90°C during heat up and 40°C to 50°C during cool down. When the

same sample was exposed to a temperature cycle of 0°C to 120°C, no transitions were seen.

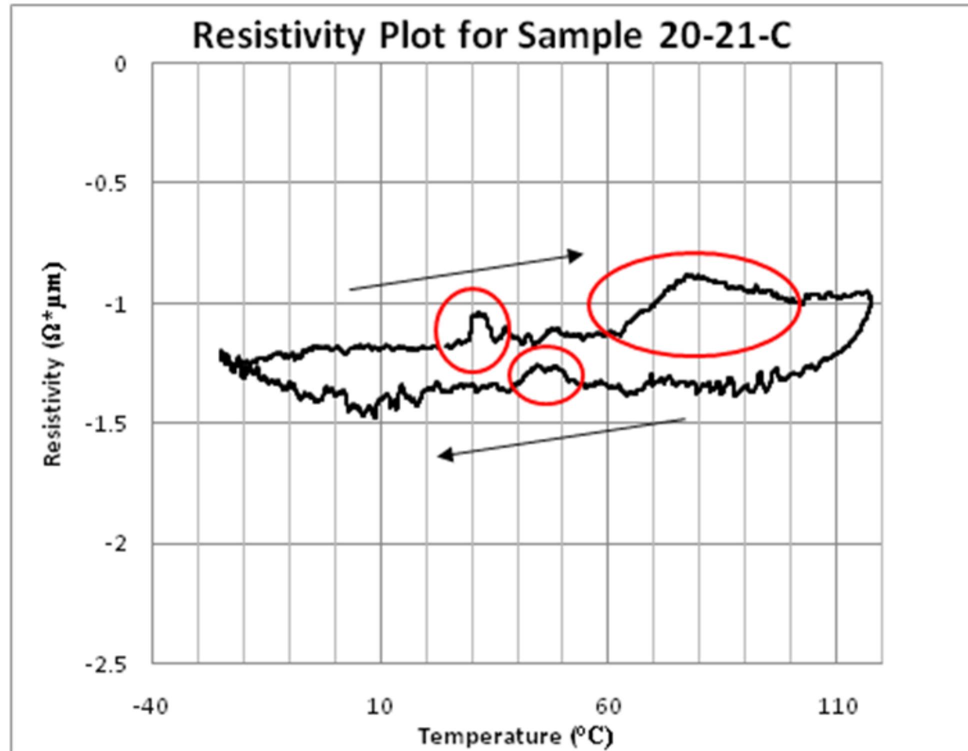

Figure 6-24 Resistivity plot for Sample 20-21-C.

On the other hand, Samples 20-64-C and 20-64-D were exposed to 0°C to 120°C temperature cycle. The resistivity plots for these samples can be seen in Figure 6-25. The data for both samples are pretty similar except 20-64-D has slightly higher resistivity values than Sample 20-64-C and at the colder end of the temperature cycle data collection, the data jumped around in a manner not

previously seen. Sample 20-64-D shows that the data collected during cool down was greater than that data collected during heat up. A distinct peak is seen during cool down between 28°C and 32°C and a number of peaks are seen below 28°C. It is important to note that this data may not look similar to other thin films because they were deposited at temperature and produced a different microstructure.

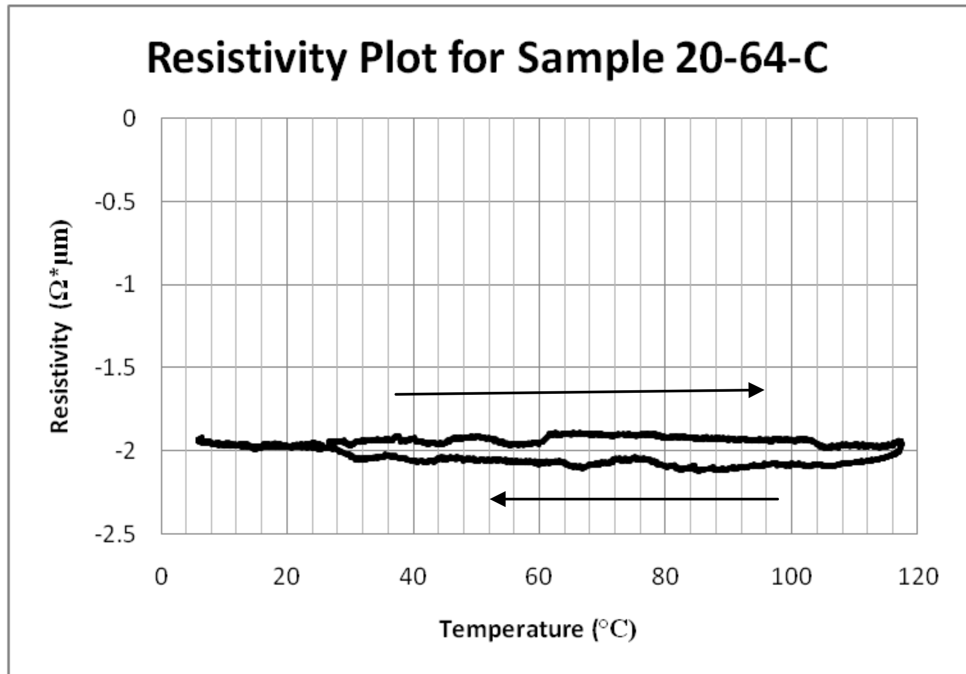

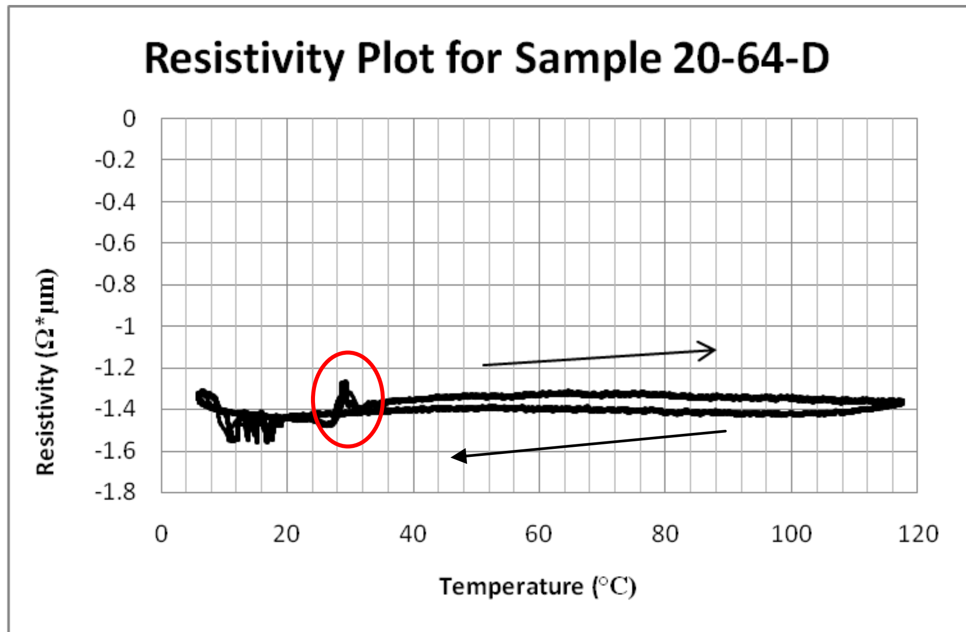

Figure 6-25 Resistivity plots for Samples 20-64-C and 20-64-D.

Sample 20-101-A also shows the unprecedented data collection observed in Sample 20-64-D's test run—the cool down resistivity data is greater than the heat up data. The only difference between the two graphs is that Sample 20-101-A presented three areas of transitions, 79°C to 88°C, 88°C to 99°C, and 4°C to 10°C. On the other hand, when 20-101-A's companion sample, Sample 20-101-B, is tested, the shape of the graph is more normal and shows hysteresis. Refer to figure 6-26 for the resistivity results. The difference between the samples is that Sample 20-101-A was deposited at 2.8 mTorr argon pressure, while Sample 20-101-B was deposited at 5.0 mTorr. In addition, the film compositions also vary—20-101-A is Ni-rich (51.53 atomic percent Nickel) and 20-101-B is equiatomic (49.69 atomic percent Nickel). Most activity seen in Sample 20-101-B is seen between 20°C to 60°C in both heat up and cool down periods, and then the hysteresis becomes tighter in the colder regions.

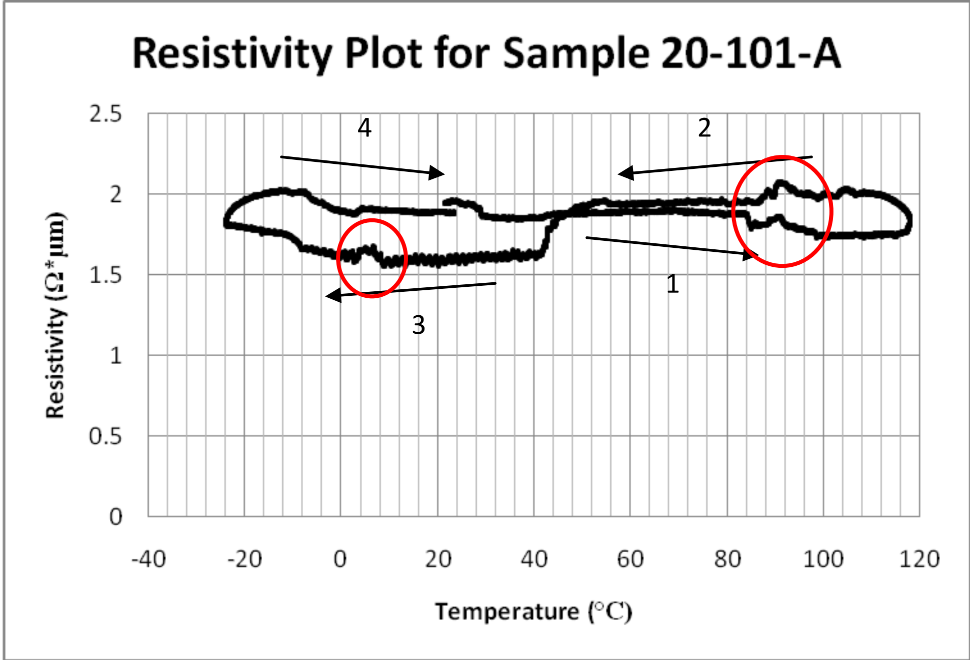

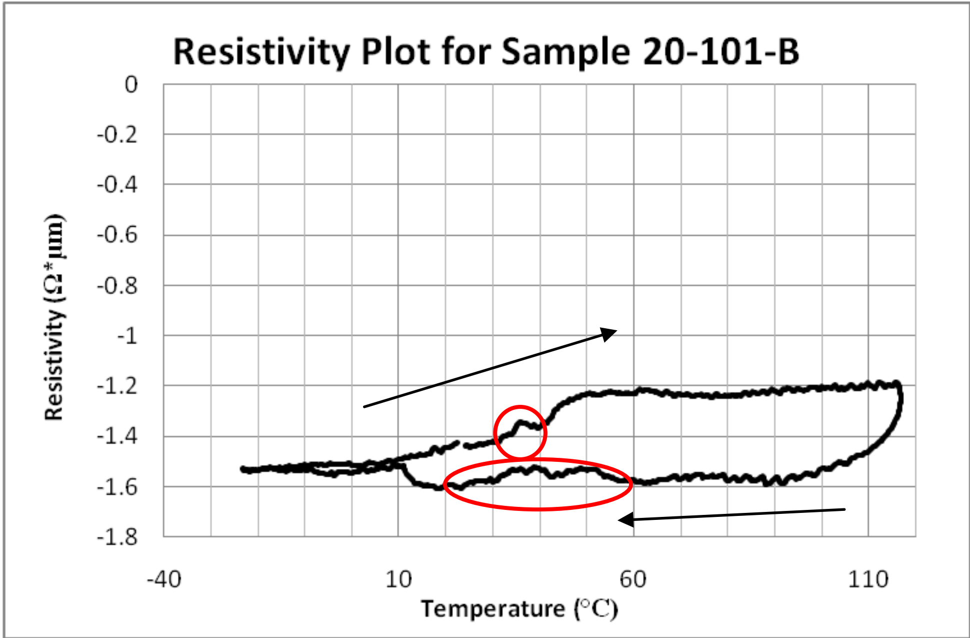

Figure 6-26 Resistivity profiles for Samples 20-101-A and 20-101-B.

Samples 25-1-A and 25-1-B were produced using the same deposition parameters as Sample 20-101-A except with varying sputtering times--Sample 25-1-A is 1 μm thick while Sample 25-1-B is 2 μm thick. Both resistivity data plots are within the same range. The resistivity plot for Sample 25-1-A is uneventful until a transition peak is seen between 0°C and 8°C during the heat up period. On the other hand, Sample 25-1-B has transition peaks between 13°C to 24°C during heat up period and 26°C to 54°C during cool down. The resistivity plots for both Sample 25-1-A and 25-1-B can be seen in Figure 6-27.

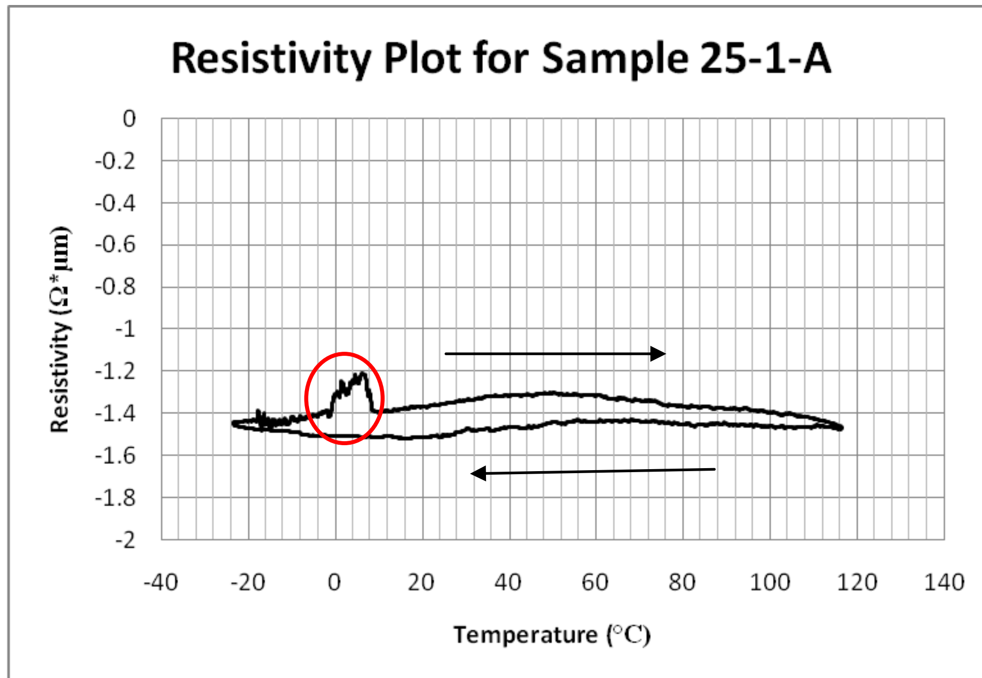

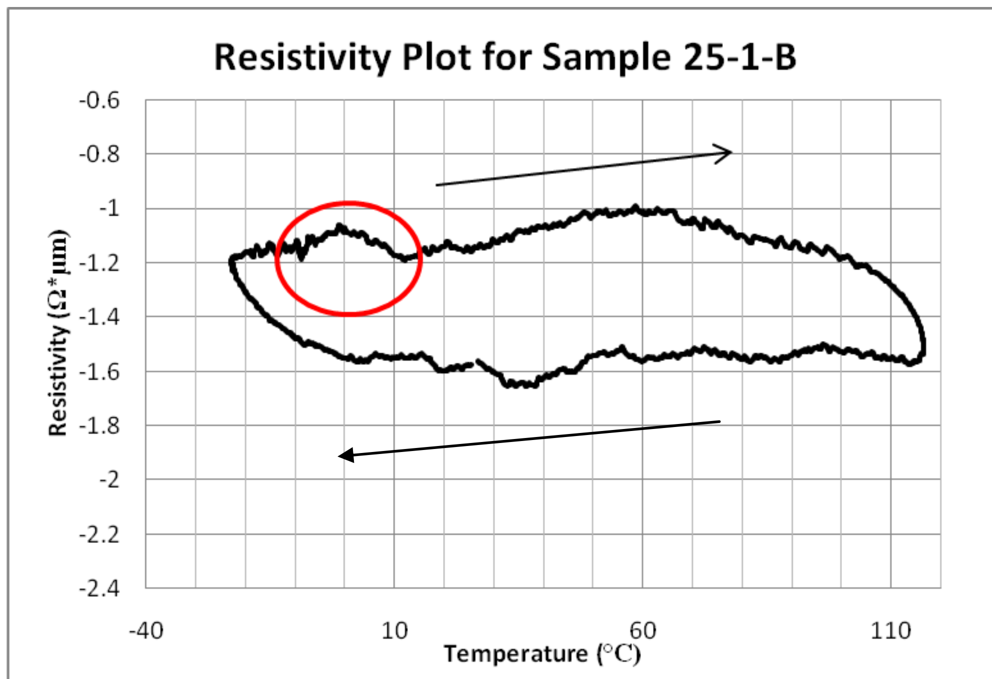

Figure 6-27 Resistivity plots for Samples 25-1-A and 25-1-B.

Using the different sputter deposited films within the resistivity testing apparatus, transformation temperatures were outlined for most of the films. Although some produced unexpected results, the data still showed that the testing set-up was able to calculate transformation temperatures and they are comparable to those presented within literature. Table 6-5 compares the resistivity data from the films tested during this research and those reported in literature. The data for the experimental films presented here are a little higher than those seen within literature. This is due to the decrease in film thickness. The Johnson Matthey sample had the greatest resistivity range between all of the samples, yet its transformation temperatures matched those outlined with several of the produced samples—20-21-C, 20-64-D, and 20-101-B. Sample 20-101-B and the Johnson Matthey film also both showed only the austenite phase, A (110), during x-ray diffraction. Samples 20-101-A, 25-1-A, and 25-1-B all show transitions at the low or colder end of the temperature cycle, between -10°C to 10°C. These samples share the same phases A (110) and M (020).

Sample/Researchers	Sample History	Composition	Resistivity (Ω*μm)
SK Wu, HC Liu, & TY Lin [1]	2 mm x 2 mm x 40 mm; hot rolled; 400°C/24 hour aging; water quench	Equiatomic Ti-51 at% Ni	0.5-1.3
AD Johnson [2]	Bulk sample	n/a	0.75-0.85
NW Botterill & DM Grant [3]	5 μm thick; 600°C/30 min anneal; acetone clean	Ti-47.5 at% Ni Ti-49.6 at% Ni	0.53-0.56
KP Mohanchandra, KK Ho, & GP Carman [4]	500°C/20 min anneal	n/a	0.65-0.83
Johnson Matthey	50.8 μm thick	Ti-50.06 at% N	0-8
20-21-C	3.73 μm thick	Ti-47.59 at% Ni	0.87-1.5
20-64-C	1.00 μm thick	Ti-49.95 at% Ni	1.9-2.1
20-64-D	1.00 μm thick	Ti-48.30 at% Ni	1.3-1.5
20-101-A	1.66 μm thick	Ti-51.53 at% Ni	1.6-2.1
20-101-B	1.66 μm thick	Ti-49.69 at% Ni	1.2-1.6
25-1-A	1.05 μm thick	Ti- 50.15 at% Ni	1.2-1.5
25-1-B	2.04 μm thick	Ti-48.34 at% Ni	1-1.7

Table 6-5 Resistivity data comparison between literature samples and experimental samples

6.7 References

[1] SK Wu, HC Liu, and TY Lin. *Materials Science and Engineering A.* 438-40 (2006) 536-539.

[2] AD Johnson. *Journal of Micromechanics and Microengineering.* 1 (1991) 34-41.

[3] NW Botterill and DM Grant. *Materials Science and Engineering A.* 378 (2004) 424-428.

[4] KP Mohanchandra, KK Ho, and GP Carman. *Journal of Intelligent Material Systems and Structures.* 15 (2004) 387-392.

Chapter 7 Conclusion and Future Work

Shape memory alloys are materials that when deformed at a low temperature they are capable of returning to their original shape or form when exposed to the appropriate thermal or stress procedure. The shape memory effect is characterized by three phases—austenite, martensite, and rhombohedral. Austenite or the B2 phase has a CsCl type order. Martensite has a monoclinic or orthorhombic type structure that depends upon the sample's composition. Rhombohedral or R-phase is composition dependent and appears upon cooling and before the martensitic transformation occurs. Although the first documentation of the shape memory effect was seen in 1938, this phenomenon did not grab worldwide publicity until William J. Buehler of the U.S. Naval Ordinance Laboratory presented his findings in 1962 on nickel-titanium. In his honor, nickel titanium shape memory alloys are also known as Nitinol—Nickel titanium Naval Ordinance Laboratory. Numerous alloy systems have been discovered that exhibit the shape memory effect like TiNb, AgCd, NiAl, NiTi, and CuZnAl. However, only copper-based systems (such as CuZnAl and CuAl Ni) and Nickel Titanium (Nitinol or NiTi) have been given substantial commercial attention. The NiTi system is often preferred due to its large shape memory strain, thermal stability, excellent corrosion resistance, high ductility, considerable

work per unit mass, and attractive transformation temperature. Since their discovery, SMA have been introduced to several industries—aerospace/aeronautical, medical, industrial/civil engineering, consumer products, automotive, and electronics.

The most commonly measured bulk scale properties for SMA include hardness, yield strength, Young's modulus, electrical resistance, and deformation abilities. Although these properties have been investigated, SMA characterization and testing has yet to be standardized. It is also common practice for each SMA investigative team to test their samples within their own labs with "homemade" testing equipment and produce them with a myriad of processing parameters. Although substantial information is available on the mechanical and physical properties of bulk scale shape memory alloys, minimal data is available for thin film shape memory alloys. The discrepancy among the thermomechanical processing parameters for thin film SMA because of the variations between research teams and their respectively available equipment makes it difficult to rapidly produce SMA films for characterization and application. The objective of this research was to resolve these issues and help the community bring more theoretical devices into fruition.

The NiTi thin films investigated within this study were produced using sputter deposition, annealed using a brew furnace, and characterized using x-ray diffraction, scanning electron microscopy, energy dispersive x-ray spectroscopy, and electrical resistivity. Sputter deposition was chosen over other production methods due to its ability to control film thickness and composition and its ability

to produce films with excellent mechanical film properties and extremely fine grain sizes. Sputtering also allows more adherent films to be deposited and allows the production of complex shaped objects. When films are deposited at room temperature, they are amorphous and unable to present the shape memory effect. Therefore, an annealing schedule was required. The outlined characterization methods allowed the investigation of phases present, microstructure observation, composition, and transformation temperature. The optimal sputter deposition parameters to produce crack-free films consisted of NiTi target power of 400 W, Ti target power of 15 W, and an argon deposition pressure of approximately 2.8 mTorr. If the same parameters were used with either 5.0 or 8.1 mTorr deposition pressure, then the resultant films would delaminate or have cracked surfaces, respectively. Majority of the deposited films showed mixed phases present—both austenite and martensite phases were present. A few showed only the austenite phase, but there was no recognizable correlation between the samples and the phases present. After numerous resistivity testing setup variations, the transformation temperatures of several sputter deposited NiTi thin films were established. An internal 4-wire ohm configuration provided within the data acquisition unit, a small environmental chamber set to cycle between -30°C to 120°C, and novel testing apparatus were used to gather this data. The success of this non-destructive data collection allows devices to be tested in their fully microfabricated state and not through a separate, often times destructive, testing step, such as before device fabrication.

In the future, it would be beneficial to produce and characterize microactuation devices using the parameters outlined above. The devices should be produced at varying thicknesses and dimensions. In so doing, the established nondestructive resistivity testing setup can be used to determine transformation temperatures of the microactuation devices in their current form.